FABRICATION, CHARACTERIZATION, AND INDUSTRIAL VIABILITY OF SUSTAINABLE THIN FILMS AND COATINGS DERIVED FROM ALUMINUM BASED NANOCLUSTERS

by

JORDAN D. LEVINE

A DISSERTATION

Presented to the Department of Chemistry and Biochemistry
and the Division of Graduate Studies of the University of Oregon
in partial fulfillment of the requirements
for the degree of
Doctor of Philosophy

June 2021

DISSERTATION APPROVAL PAGE

Student: Jordan D. Levine

Title: Fabrication, Characterization, and Industrial Viability of Sustainable Thin Films and Coatings Derived from Aluminum Based Nanoclusters

This dissertation has been accepted and approved in partial fulfillment of the requirements for the Doctor of Philosophy degree in the Department of Chemistry and Biochemistry by:

Catherine J. Page	Chairperson
Darren W. Johnson	Advisor
Kenneth M. Doxsee	Core Member
Richard P. Taylor	Institutional Representative

and

Andrew Karduna	Interim Vice Provost for Graduate Studies

Original approval signatures are on file with the University of Oregon Division of Graduate Studies.

Degree awarded June 2021

DISSERTATION ABSTRACT

Jordan D. Levine

Doctor of Philosophy

Department of Chemistry and Biochemistry

June 2021

Title: Fabrication, Characterization, and Industrial Viability of Sustainable Thin Films and Coatings Derived from Aluminum Based Nanoclusters

Inorganic metal oxides are extremely versatile materials that make up many components of modern technology. In order to keep up with increasing demand, microelectronics industries have optimized their fabrication techniques to produce pristine high-quality metal oxide films at high through-puts. While the resulting materials have underpinned current technological advances, it has come at a huge energetic and environmental price. The fabrication of these materials from traditional vapor deposition techniques requires high processing temperatures, vacuum conditions, as well as the use of toxic precursors. These processing conditions are detrimental to the environment and as technology continues to define modern day society, and without any remediation, the ecological and environmental impacts of will continue to compound.

Solution processing of metal oxides provides a significantly greener and environmentally friendly approach to the production of metal oxide films and coatings. In this method, films can be fabricated using significantly less processing energy, less toxic precursors, and environmentally benign solvents. Additionally, the ability to solution deposit allows for an extremely scalable and versatile process that industry can easily adapt to suit their desired application, all while using inexpensive starting materials.

This dissertation will detail the exploration of a novel solution deposition precursor, display the development of a scalable coating process tailored for industry, and demonstrate the potential environmental impact of solution processing in the textiles space. Chapter I begins by highlighting the ubiquity of metal oxides, the challenges with their current fabrication methods, and the sustainability benefits that solution processing of metal oxides provides. Chapter II explores the viability of a novel solution deposited precursor used to produce high-quality mixed-metal oxide films. Chapters III and IV highlight the environmental and scalability benefits that solution deposited Al_2O_3 films have to offer. Chapter V will detail the non-destructive characterization technique of innovative nanomaterials. Chapter VI will frame all of this work in the context of sustainability and the production of the next generation of metal oxide films. This thesis contains previously published and unpublished co-authored material.

CURRICULUM VITAE

NAME OF AUTHOR: Jordan D. Levine

GRADUATE AND UNDERGRADUATE SCHOOLS ATTENDED:

University of Oregon, Eugene, Oregon
University of Arizona, Tucson, Arizona

DEGREES AWARDED:

Doctor of Philosophy, Chemistry, 2021, University of Oregon
Master of Science, Chemistry, 2017, University of Oregon
Bachelor of Science, Chemistry, 2016, University of Arizona

AREAS OF SPECIAL INTEREST:

Sustainable materials chemistry
Green chemistry
Metal oxide thin films
Water repellent coatings
Nanomaterial Characterization
Scanning electron microscopy

PROFESSIONAL EXPERIENCE:

Graduate Research Assistant, University of Oregon, 2018 - 2021

Materials Innovation Extern, Minteq International, 2019 – 2020

Lens of the Market developmental workshop, University of Oregon, 2018

Graduate Teaching Fellow, University of Oregon 2016 – 2018

T.W. Lewis Scholar, University of Oregon, 2012-2016

GRANTS, AWARDS, AND HONORS:

Center for Sustainable Materials Chemistry (CSMC) Research Fellow, University of Oregon, 2017- 2021

LGBT in STEM travel award, University of Oregon, 2019

Dean's First Year Merit Award, University of Oregon, 2016

Graduate Student Award for excellence in teaching, University of Oregon, 2018

PUBLICATIONS:

Levine, J. D.; Sharps, M. C.; Cochran, E. A.; Marsh, D. A.; Casey, W. H.; Johnson, D. W. Investigation of the Physical, Optical, and Chemical Properties of Phase Segregated AlCoOx Thin Films from a Novel Hexol-Type Cluster. *Dalton Trans* **2021**, *50* (9), 3247–3252.

Sherbow, T. J.; Kuhl, G. M.; Lindquist, G. A.; Levine, J. D.; Pluth, M. D.; Johnson, D. W.; Fontenot, S. A. Hydrosulfide-Selective ChemFETs for Aqueous H2S/HS− Measurement. *Sensing and Bio-Sensing Research* **2021**, *31*, 100394.

Levine, J.D.; Rosen, A. Q.; Knecht, T. A.; Johnson, D. W. A simple, scalable, eco-friendly and ultralow-temperature approach to forming Al_2O_3 water-repellent cotton coatings via UV photo-annealing. **In prep, 2021**

ACKNOWLEDGMENTS

Throughout my academic journey I have been extremely fortunate to be surrounded by such an incredible, encouraging, and supportive group of people. First and foremost, I would like to show my sincere appreciation for my advisor, Dr. Darren Johnson. I have been continually impressed by Darren's scientific intellect, his integrity, and his ability to openly engage with his students. Darren is committed to fostering an inclusive and supportive environment that truly allows his students to thrive. I sincerely do not believe I could have asked for a better advisor to guide me through graduate school. I want to thank him for believing in me and allowing me to explore scientific and professional endeavors that I was passionate about. While I will sincerely miss having him as my advisor, I am greatly looking forward to our continued friendship and all of the Alesong, sports chats, boat rides, stock discussions, and pictures of our latest kicks that we'll share. I would also like to thank my general chemistry professor, Dr. Pollard, who showed me how contagious passion can be and inspired me to pursue a career in chemistry.

I'd like to thank my thesis committee – Dr. Cathy Page, Dr. Kenneth Doxsee, and Dr. Richard Taylor – for believing in my ability to succeed and for supporting me when I choose industrial experience over publication possibilities. I would also like to thank the chemistry department front office staff, with a special thank you to Janet Macha, who is so vital to departmental operations and ensuring everything runs smoothly.

There have been so many colleagues in the DWJ lab that have guided me over the years, but it is important that I give special thanks to three in particular – Dr. Meredith Sharps, Dr. Susan Cooper, and Dr. Elizabeth Cochran. I was incredibly lucky to have their guidance in the formative years of my PhD. They taught me how to ride out the highs and

lows of grad school, the importance of work-life balance, and most importantly, the impact that a friendly note or sticker can have on someone's day. In addition to them, I would also like to thank other past and current members of the DWJ lab that I have developed genuine friendships with and have made my grad school experience truly enjoyable: Dr. Brandon Crockett, Dr. Brantly Fulton, Dr. Jessica Lohrman, Dr. Tobias Sherbow, Dr. Ngoc-Minh Phan Lau, Dr. Sean Fontenot, Doug Banning, Jeremy Bard, Hazel Fargher, Trevor Shear, Thaís de Faria, Grace Kuhl, Hannah Bates, Jacob Mayhugh, and Henry Trubenstein.

I want to thank my mentor, Dr. Brantly Fulton. I was extremely blessed to have my predecessor in the DWJ lab be someone as entrepreneurial and charismatic as Brantly. His guidance not only helped me thrive in my research, but also helped me secure a position at my dream job. I sincerely look forward to the impacts that Brantly will have on the world.

Finally, I would like to thank my family. My mom, Ellen Levine, has been the most rock solid supportive figure throughout my entire life and I am so incredibly thankful for her love and encouragement. She worked so hard to give me a happy childhood and any success I achieve is a direct reflection of her imprint on me. I also need to thank the rest of my family including Steve Levine, Todd Knudson, Norma & Irwin Silberlicht, as well as Joe & Chahine Levine (ghorboonet beram). Lastly, I would like to give my heartfelt appreciation to my partner and best friend, Ariana Gallegos. She has supported and encouraged me through every step of my PhD, and I truly wouldn't be the man I am today without her. I will always remember our days at Shannon's Place filled with love, basketball, and cuddles with the best pup in the world, Pinot. I have been so incredibly fortunate to have Ari in my life and I cannot wait to discover what our future holds.

TABLE OF CONTENTS

Chapter Page

LIST OF FIGURES

Figure Page

Figure Page

Figure Page

Figure Page

LIST OF TABLES

Table Page

CHAPTER I

INTRODUCTION TO THE FABRICATION AND FORMATION OF METAL OXIDE FILMS

Importance of metal oxides

Metal oxides are an extremely versatile class of materials that underpin much of modern day technology. They're utilized in a variety of applications including photovoltaics[1,2] semiconductors[3,4], gas sensing[5], catalysis[6], protective coatings[7], and smart windows[8]. Metal oxides are so ubiquitous in modern society, that one does not have to search far to find a fully operational metal oxide. In fact, most can find functioning metal oxides in their pocket, in the form of a smart phone. A diagnostic analysis of any generic smart phone would reveal an indium tin oxide touch conductive film over a glass screen comprising aluminum oxide and silicon dioxide.[9,10] A further look would show a rechargeable battery comprised of a lithium cobalt oxide cathode that helps power a thin film transistor containing an indium gallium zinc oxide semiconductor layer.[11,12] With technology continuing to define modern society, metal oxides have truly become the backbone to modern technical advances.

There are a variety of methods for fabricating metal oxides films. Conventional vapor deposition methods such as chemical vapor deposition or sputtering deposition are among the most common used in industry. These methods produce high-quality metal oxide films that are dense, and exhibit excellent properties for semiconducting applications. However, these methods require large amounts of energy due to the need for vacuum conditions and processing temperatures of up to 1200 °C.[13]

Due to the high energy requirements of conventional vapor deposition techniques, there has been a substantial push to determine low temperature processing methods for the next generation of metal oxide films. Low temperature processing techniques can provide industry with a cost saving approach that uses less energy, making it a much more sustainable practice. This is especially important for the field of flexible electronics that contain polymeric substrates that are prone to degrade at higher processing temperatures.[14]

Solution processing of metal oxides perhaps offers the most promising approach for the low temperature processing of films. In this process, a solution containing a metal salt precursor is deposited onto a substrate via spray coating, spin coating, dip coating, or ink jet printing. The subsequent film is then post-processed to remove solvents and counterions and produce a dense metal oxide film. Solution processing of metal oxides offers many advantages over conventional vapor deposition techniques:

- Control over precursor stoichiometry
- Low decomposition temperatures
- Precursors are soluble in environmentally benign solvents
- Scalable deposition techniques
- Cost-effective

Perhaps the most attractive quality of solution processing is the opportunity to achieve substantial sustainability improvements over currently used processes. As climate change takes its toll on the environment, large scale industrial goods manufacturers are constantly evolving their processing to meet industry wide sustainability initiatives and move towards

green chemistry practices. Solution processed metal oxide fabrication is a much more environmentally friendly process, meeting many criteria laid out in the highly esteemed 12 principles of green chemistry.[15] These involve the use of environmentally benign solvents (i.e. water, ethanol, acetone), enhanced atom-economy that prevents excess waste, minimized energy requirements (i.e. low temperature thermal and ultraviolet annealing), and no need for auxiliary substances (i.e. organic solvents, chelating agents, etc.). The importance of creating sustainable processes for the next generation of metal oxide films cannot be overstated and solution processing of these films offers the most promising approach to greatly reduce the environmental cost of producing metal oxides.

There has been significant success in using solution processing to form functioning metal oxide films. For example, Trotochaud et. al fabricated high-quality metal oxide films from metal nitrate ($M(NO_3)_x$, M= Ni, Fe, Co, Mn) precursor solutions. These spun-cast films showed high activity as catalysts in the oxygen evolution reaction (OER) and demonstrated the simplicity of the solution deposition process.[16] Additionally, they showed that by mixing different metal nitrates in predetermined ratios, they could control the final stoichiometry of mixed-metal films. Kast et. al. also demonstrated these benefits by combining a variety of metal nitrates with a precondensed cluster precursor ($Al_{13}(\mu\text{-}OH)_{24}(H_2O)_{24}$) to fabricate dense, uniform metal oxide films with near atomic smoothness, all from an aqueous precursor solution.[17]

Metal oxide formation

The formation of metal oxides is highly tunable and processing parameters can be adjusted to achieve desired film morphologies and properties. When starting the solution deposition process, substrates first need to be adequately prepared. In order to prevent

surface defects and ensure uniform wetting, substrates need to be sufficiently hydrophilic. This is achieved through a variety of activation processes with the most common being plasma treatment, a process that blasts the substrate with reactive oxygen species, removing organic contaminants and generating a polar hydrophilic surface. Once the substrate is prepared, the precursor solution can be deposited onto the surface via the determined deposition technique. After the substrate is adequately wet with precursor solution, external thermal energy is needed to begin evaporating the solvent and initiate the gelation of the film. As the heating process continues, nitrates in the film decompose and are removed as a HNO_3/H_2O azeotrope and NO_x gas, initiating condensation and the formation of M-OH species. At this point, the film is still porous and additional heating is needed to completely remove all solvent and nitrate counterions to form a dense M-O-M network in the film.[18] An overview of this process is presented in Figure 1.1.

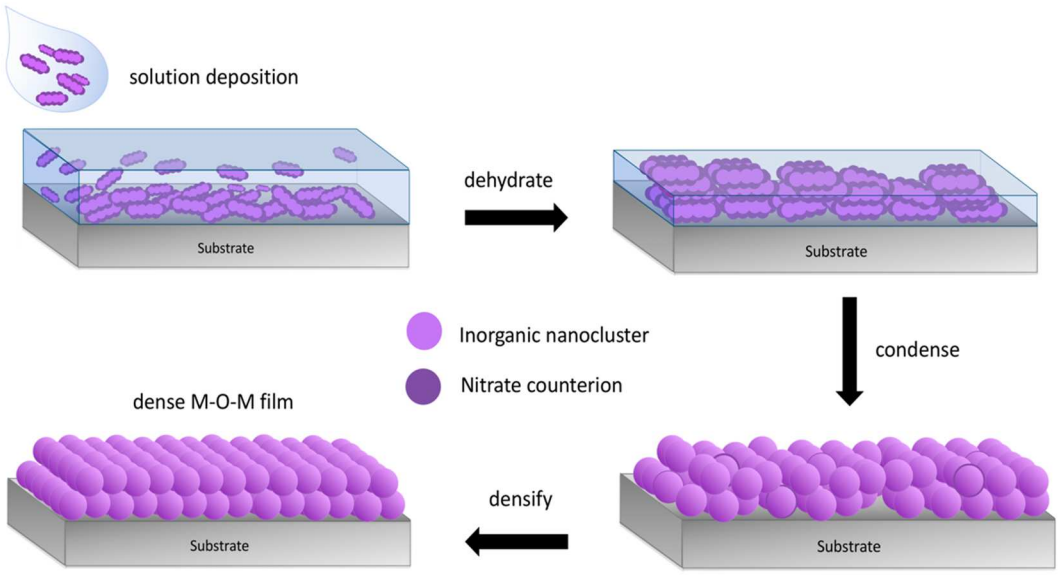

Figure 1.1 Stages of solution deposited metal oxide films. In first step, substrate is wetted with precursor solution. Excess solvent is then evaporated. Nitrate counterions then decompose from film through thermal or photo-annealing. Dense metal oxide film is fully formed after all solvent evaporates and counterions decompose.

Inorganic nanoscale clusters as solution deposition precursors

Inorganic nanoscale clusters have been widely explored as thin film precursors in an effort to alleviate the problems that existed with traditional sol-gel depositions. In sol-gel fabrications, metal precursors are dissolved in organic solvents and are precondensed with organic ligands before annealed to form films that have uniform distribution of metal throughout the film. Due to the high amount of organic additives and solvent in the sol-gel process, the annealing process causes morphological defects and pores in the final films.[19,20] These issues can be mitigated by using inorganic nanoscale clusters as the starting precursor. The precondensed nature of inorganic clusters and lack of organic ligands leads to metal oxide films that densify more readily and have fewer morphological defects.

One common class of inorganic clusters is the metal-hydroxo M_{13} nanoscale cluster with the general formula of $[M_{13}(\mu\text{-}OH)_{24}(H_2O)_{24}](NO_3)_{15}$ where M is Al,Ga,In or a combination thereof. These planar structures, termed "flat", consist of octahedrally-coordinated metal centers in a precondensed M-O-M network with uncoordinated outer sphere nitrate counterions. One of the factors that makes this class of clusters so attractive as a thin film precursor is the increased metal to nitrate ratio. The flat-Ga_{13} (f-Ga_{13}) cluster for instance contains 13 gallium atoms per 15 nitrate counterions allowing for a 13:15 ratio. This ratio is much higher than that of $Ga(NO_3)_3$ which has a 1:3 metal to nitrate ratio. As discussed previously, it is imperative for the proper decomposition of nitrate counterions to form dense metal oxide films. Therefore, theoretically, the f-Ga_{13} cluster with a higher $Ga:NO_3$ ratio would produce denser films than that of its nitrate counterpart. This concept was proven by Jo et. al. in their work where they compared solution processed films

fabricated from the f-Al_{13} cluster and aluminum nitrate and found that the cluster films exhibited higher densities and less porosity.[21]

These clusters are not only viable as thin film precursors, but their resulting metal oxide thin films show film functionality that is comparable to currently used industry fabrication methods. Nadarajah et. al. showed the practicality of indium/gallium heterometallic clusters by tuning the stoichiometry of the precursor solution to produce high quality IGZO films that contained homogeneous distribution of metal ions due to the precondensed nature of the heterometallic indium/gallium cluster. Interestingly, the solution processed IGZO films demonstrated higher channel mobilities than analogous sputtered films.[22] Additional work by Smith et. al. compared solution processed Al_2O_3 films from the f-Al_{13} to films fabricated from atomic layer deposition (ALD), and although films from the cluster were not as dense as the ALD films, they did exhibit lower leakage currents.[23]

With the advancements that solution deposition has made, it is increasingly important as well to investigate and modify the precursors that are being utilized in these processes. One of the most investigated nanoscale clusters to date is the flat-Al_{13} cluster $[Al_{13}(\mu\text{-}OH)_{24}(H_2O)_{24}]^{15+}$ (Figure 1.2) due to its proven record of producing high quality Al_2O_3 coatings and thin films. First isolated by Seichter et. al. in 1998, the f-Al_{13} cluster consists of a planar structure containing 13 aluminum atoms coordinated by bridging hydroxides. This discovery by Seichter et. al. established the groundwork for these inorganic clusters, leading to many innovative synthetic approaches. For example, Gatlin et. al. demonstrated the use of a reductant, N-nitrosodibutylamine (DBNA), to control the pH of the aluminum nitrate solution and slowly precipitate out the f-Al_{13} cluster in

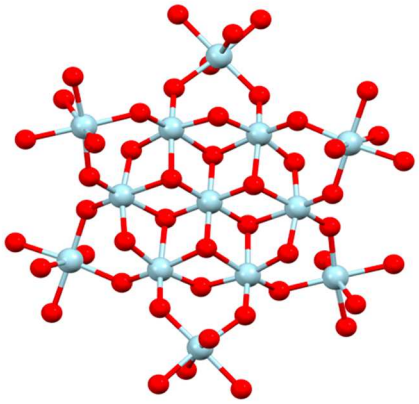

Figure 1.2 Crystal structure of "flat" metal-hydroxo Al_{13} nanoscale cluster. Hydrogen atoms removed to show precondensed M-O-M network.[25]

appreciable yields (60 %).[26] This work was expanded upon as Wang et. al. replaced the carcinogenic DBNA reductant with less toxic zinc metal (Zn^0) to controllably reduce the acidic nitrate solution and form the cluster ref.[27] Most recently, Fulton et. al. provided a scalable, one-pot, alternative method for synthesizing the Al_{13} cluster. In this "top-down" dissolution approach, solid $Al(OH)_3$ was dissolved in stoichiometric amounts of HNO_3 to form an aqueous solution with the f-Al_{13} cluster as the dominant product that could be easily scaled up for industrial use.[28]

The work by Fulton et. al was particularly impactful in the field because it provided an extremely scalable method to develop the f-Al_{13} precursor for Al_2O_3 coatings. In order for industry to adapt solution processing into their fabrication methods, it not only has to produce high quality metal oxide films, but it also has to be economically viable. This dissolution method utilizes the inexpensive and relatively abundant $Al(OH)_3$ mineral that is significantly cheaper than the more commonly used $Al(NO_3)_3 \cdot 9H_2O$ precursor ($0.04 mol^{-1} compared to $0.3 mol^{-1}, respectively).

With all of the advances in solution processing, it is now becoming extremely viable for applications scientists to incorporate solution deposition into their manufacturing process. This thesis will describe the synthesis and characterization of a novel solution deposition precursor in Chapter II, show the industrial viability and scale up of the f-Al_{13} cluster in Chapter III, and demonstrate the use of the cluster in the next generation of low temperature solution processed water repellents for textiles in Chapter IV. The chapters presented will not only demonstrate the ability for inorganic clusters to make high quality films, but also demonstrate that solution deposition is an innovative and sustainable solution that can be easily adapted to suit industrial requirements.

Bridge to Chapter II

The presented introduction demonstrates the viability of inorganic clusters and the opportunities that solution deposition techniques have on producing sustainable metal oxides. In order to continue innovating in the solution deposition space, it is important to continually investigate new inorganic clusters that can be used as precursors. In Chapter II, we present a novel mixed-metal heterometallic precursor that was investigated for its viability as a thin film precursor. This chapter will also introduce a significant amount of characterization techniques that will be seen throughout this thesis such as atomic force microscopy (AFM), scanning electron microscopy (SEM), X-ray diffraction (XRD), X-ray photoelectron spectroscopy (XPS) and transmission electron microscopy (TEM).

CHAPTER II

INVESTIGATION OF THE PHYSICAL, OPTICAL, AND CHEMICAL PROPERTIES OF PHASE SEGREGATED ALCOOX THIN FILMS FROM A NOVEL HEXOL-TYPE CLUSTER

Authorship Statement

This chapter contains material previously published in *Dalton Transactions* **2021**, 50, 9, 3247-3252. This work was coauthored by Jordan D. Levine, Meredith C. Sharps, Elizabeth A. Cochran, David A. Marsh, William H. Casey, and Darren W. Johnson. The manuscript was written by J.D.L with contributions and editorial assistance from all authors.

Introduction

Mixed-metal oxides are extremely versatile materials due to their attractive thermal, electronic, and optical properties, which has led to their extensive use in a variety of fields ranging from photovoltaics to thin film transistors.[1-3] The recent push towards more cost effective and less energy-intensive processing of these materials has led to the utilization of solution-based deposition methods that allow for scalable and inexpensive fabrication of high quality metal oxide thin films.[4,5] While sol-gel techniques offer the benefits of solution-based fabrication, they often have the potential to leave behind organic contaminants which can be detrimental to film formation and properties.[6] Nanoscale inorganic clusters are a promising alternative precursor for solution processing of thin films because their precondensed metal-hydroxyl network and nitrate counterions can more

readily condense to form films with fewer morphological defects. Upon annealing of these films, nitrate counterions decompose and solvent evaporates, initiating the formation of a metal-hydroxyl species $M(OH)_x$. From here, further annealing can remove any remaining solvent and counterions, condensing the metal-hydroxyl network into the final metal oxide. Nadarajah et. al. has shown the benefits of inorganic clusters, utilizing heterometallic gallium and zinc nanoscale clusters to form high-quality IGZO thin film transistors that exhibit higher channel mobility than analogous metal nitrate and sol-gel films.[7] Additional work by Jo et. al utilized the flat-Al_{13} cluster to produce aluminum oxide dielectrics with ultralow processing temperatures via a UV-light activation process. This work highlighted the advantages of the cluster, demonstrating how it leads to more dense films than analogous metal nitrate films due to the cluster's high aluminum to nitrate ratio.[8] These advancements in the field have ultimately raised the profile of inorganic clusters as thin film precursors for a variety of applications in electronics and roll-to-roll processing.[9,10] While processing conditions are continually being optimized to realize more energy-efficient thin film fabrication techniques, it is also vitally important to continue to investigate potential precursor compositions for solution deposition. Inspired by the successful incorporation of clusters into films and devices, our lab previously reported a novel nanoscale cluster modelled after Werner's famous hexol (Fig 2.1, M=Al, Ga, In), which is notable as the first compound to exhibit molecular chirality without the presence of any carbon.[11,12] Due to their outer sphere nitrate counterions, preorganized structure, and low decomposition temperature, this class of clusters are a viable candidate to be investigated as precursors for solution deposited thin films.

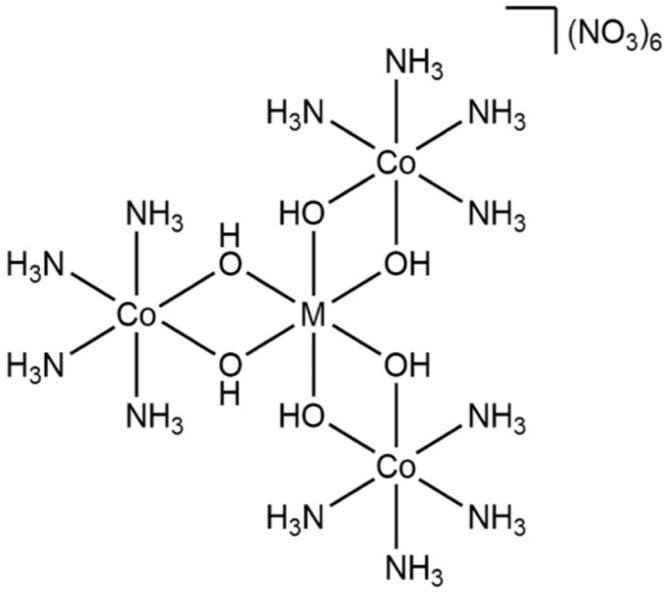

Figure 2.1. Werner's famous hexol (M=Co). For this work, M=Al was used as the thin film precursor.

We previously reported the synthesis and characterization of a series of heterometallic hexol-type clusters ($M[(\mu\text{-}OH)_2Co(NH_3)_4]_3(NO_3)_6$ M= Al, Ga, In).[11] As a proof of concept for the use of these hexol-type clusters as thin film precursors, the aluminum cobalt cluster ($Al[(u\text{-}OH)_2Co(NH_3)_4]_3(NO_3)_6$, **CoAl**) was investigated. This specific aluminum cluster was chosen because of its low decomposition temperature (Figure 2.2), as well as its heterometallic chemical composition which would allow for a direct comparison to similar films fabricated from Kast et. al.[4] In their work, the flat-Al_{13} cluster is combined with $Co(NO_3)_2{\cdot}6H_2O$ at varying ratios in solution to produce a mixed metal oxide film that readily phase segregates into the corresponding oxides at 450 °C. This highlighted the importance of studying heterometallic systems, and produced substantial precedence detailing the formation of mixed-metal oxide films.

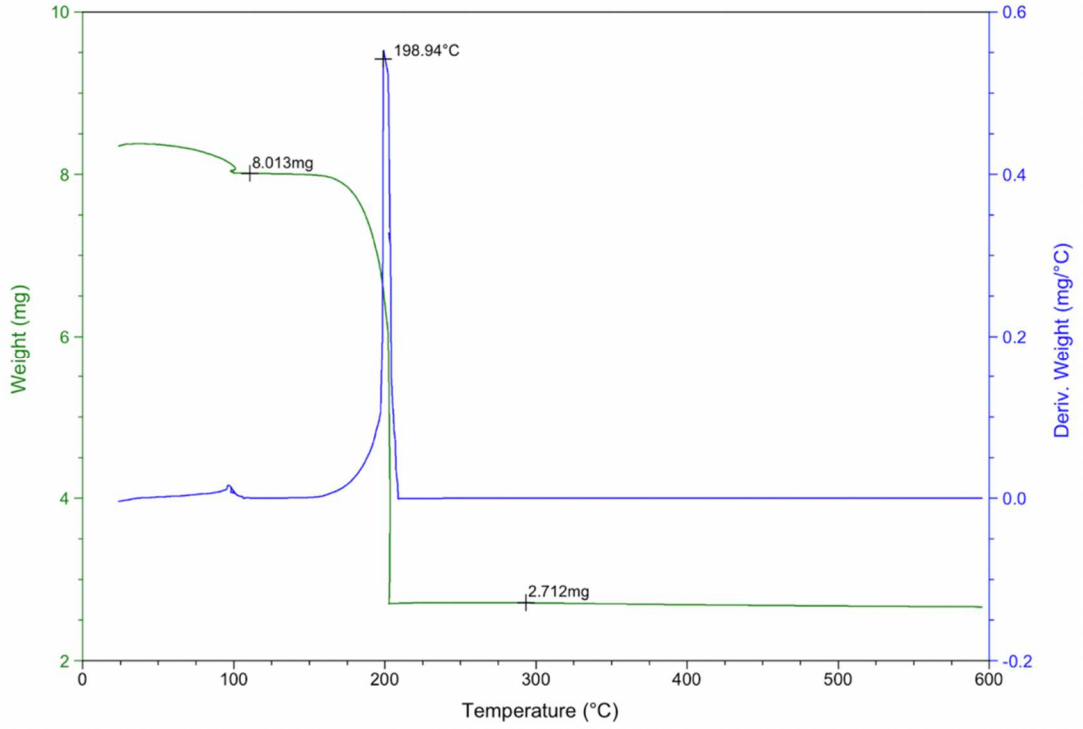

Figure 2.2 Thermogravimetric analysis (TGA) of CoAl precursor. Mass loss event at 198.94 °C correlates to the decomposition of the outersphere nitrate groups and ammine ligands.

In this study, we sought to investigate if the proposed **CoAl** cluster would produce similar results yielding the binary phase segregated oxides or if the precondensed nature of the cluster would produce an alloy with a homogenous distribution of cations throughout the film. Additionally, we sought to assess how temperature affects the morphological and microstructural properties of films made from a single-source cobalt and aluminum precursor.

We were able to demonstrate through microstructural, optical, and elemental characterization that the novel **CoAl** cluster is a suitable precursor for solution deposited thin films. In addition, we confirmed that despite the precondensed nature of the cluster, a phase segregated binary oxide is produced. To our knowledge, fabrication and

characterization of these types of films have not been attempted, and these studies suggest that future work could lead to other derivatives of Werner's hexol being used for thin film fabrication.

2.2 Experimental

Preparation of precursor solution

Cobalt aluminum hexol-type clusters (**CoAl**) were fabricated using a previously reported procedure.[11] To synthesize the cluster, a 1.0 M aqueous solution of $Al(NO_3)_3 \cdot 9H_2O$ was added dropwise to a 0.5 M aqueous solution of $[Co(NH_3)_4(CO_3)](NO_3)$. The reaction was stirred at room temperature for 1 hour and was filtered and purified to yield the final **CoAl** cluster product. For the final precursor solution, a 0.4 M solution of the **CoAl** cluster dimethyl sulfoxide (DMSO) was filtered through a 0.45 micron filter before deposition.

Film deposition and annealing

Single-side polished Si (100) was used for XRD, AFM, and XPS studies. Fused-quartz substrates were used for UV-Vis and XRR studies. All substrates were scored with a diamond scribe on the unpolished side and cleaved into 2 × 2 cm squares. Substrates were loaded into a Teflon boat that held the samples in a vertical orientation. Substrates were washed in a sonicator for 10 min in a solution of 6.25% Contrad 70, rinsed with nanopure (18.2 MΩ) water for 30 s, loaded onto a spin-coater, spin rinsed for 10 s, spin dried for 20 s at 2500 rpm, and placed on a hot plate at 100 °C for 2 min to finish drying. The substrates were then plasma cleaned in an O_2/N_2 mixture for 10 min, spin rinsed with nanopure water

for 5 s, and spin dried for 25 s to remove any dust before the precursor solution was deposited.

Once substrates were prepared, the 0.4 M precursor solution was deposited dropwise from a syringe onto the substrate and spun for 150 s at 2500 rpm. The samples were immediately moved to a hot plate and annealed for 10 min at 250 °C. To fabricate multilayered films, as-spun samples were subjected to subsequent solution depositions and annealed at 250 °C on a hot plate until the desired number of layers was obtained. Samples were then post-annealed in a box furnace up to the desired temperature at a ramp rate of 12.5 °C/min and were annealed for 30 min at the allotted temperature.

Film characterization

CoAl cluster bulk powder was analyzed using thermogravimetric analysis (TGA) on a TA instruments thermogravimetric analyzer, TGA Q500, by ramping from room temperature to 600 °C at a rate of 10 °C per minute under N_2 atmosphere. X-ray diffraction data was collected in a grazing incidence XRD (GI-XRD) geometry on a Rigaku SmartLab with Cu Kα radiation (λ = 0.15418 nm). The incident angle of the X-ray beam was 0.5° relative to the sample plane, and the scintillation point detector was swept from 10° to 70° relative to the sample plane in 0.2° steps with an integration at each step of 30 s. Elemental composition was performed using a Thermo Scientific ESCALAB 250 X-XPS with an Al Kα monochromated source at 20 kV. Film thickness was determined through low-angle X-ray reflectivity (XRR) using a Bruker D8 Discover diffractometer, equipped with Cu Kα radiation and a Göbel mirror. Film thicknesses were determined by indexing the Kiessig fringes and using a modified version of Braggs law corrected for refraction. Atomic force

microscopy **(**AFM) images were collected using a Bruker Dimension Icon atomic force microscope equipped with FastScan. Al-coated Si tapping mode probes were used, and images were collected over 1 μm^2 areas. Elemental composition and surface morphology images were determined by scanning electron microscopy energy dispersive X-ray spectroscopy (SEM-EDS) using a ThermoFisher Helios Hydra Plasma FIB. Transmission electron microscopy (TEM) images were collected on an FEI Titan 80-300 equipped with a C_s image corrector with an accelerating voltage of 300 KV. Samples were placed on a TEM grid using the focused ion beam on ThermoFisher Helios Hydra Plasma FIB. Transmittance measurements were collected on a PerkinElmer Lambda-1050 UV/vis/NIR spectrophotometer utilizing a 150 mm integrating sphere. Background samples were collected in air and with a blank quartz substrate. Transmittance data was collected from 300 nm to 800 nm at 1 nm intervals.

Results and discussion

The films' physical properties, morphology, and composition were studied by varying the number of deposited layers and annealing temperature. The spun-cast films were initially deposited from aqueous solutions, but even with significant varying of deposition parameters, films appeared to have undesirable surface defects and thus DMSO was utilized (Figure 2.3).

In order to investigate the crystal structure of the fabricated films, a GI-XRD annealing study was performed. Figure 2.4 shows the GI-XRD diffraction pattern of a **CoAl**-produced thin film annealed at 250 °C compared to films that were post-annealed at

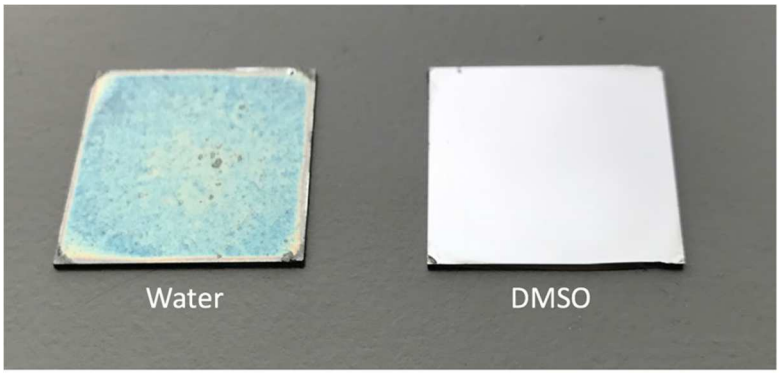

Figure 2.3 CoAl films fabricated from water (left) and DMSO (right). After spin coating and soft bake at 250 °C films from water had significant surface defects compared to ones from DMSO.

temperatures of 400 °C, 600 °C, and 800 °C. These diffraction patterns are referenced to the Co_3O_4 diffraction pattern. The diffraction peaks at 2θ = 19.0°, 31.3°, 37.0°, 44.9°, 55.6°, 59.5°, and 65.4° can be indexed to (111), (220), (131), (040), (224), and (440) reflections in Co_3O_4 spinel, respectively. The initial hot plate anneal of films at 250 °C and films annealed at 400 °C exhibit the emergence of a crystalline phase in a mostly

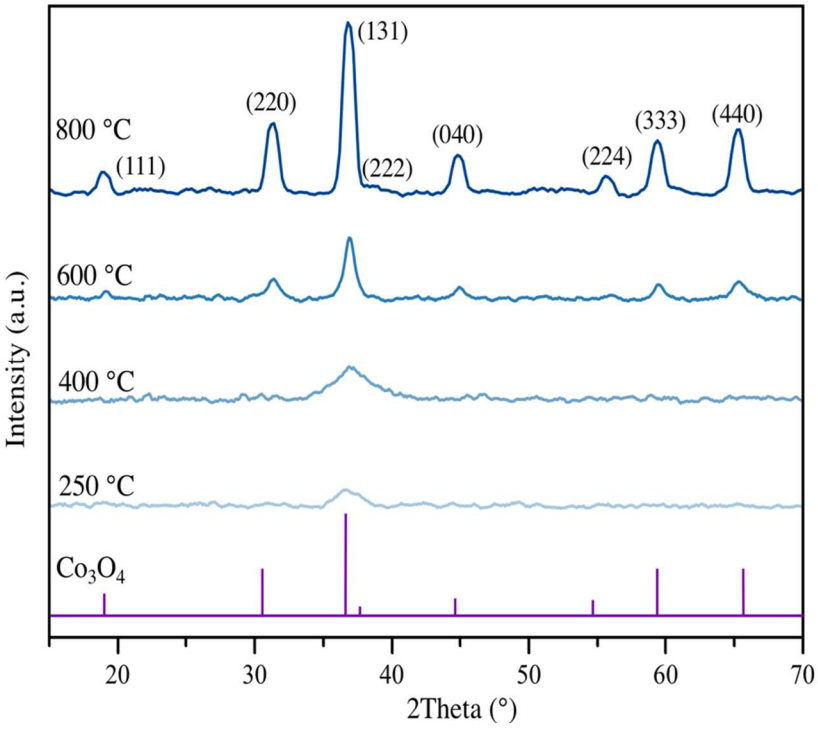

Figure 2.4. GI-XRD diffraction patterns of **CoAl** films annealed at 250 °C, 400 °C, 600 °C, and 800 °C, referenced to Co_3O_4.

amorphous film. By 800 °C, the crystallinity greatly increases, and the diffraction pattern can be indexed to the Co_3O_4 spinel.[13] No other diffraction peaks were detected, suggesting that the cobalt present from the cluster crystallizes into the Co_3O_4 spinel crystal structure. However, due to the similarity in ionic radii of Co^{3+} and Al^{3+}, it can be difficult to exclude the possibility of Al^{3+} ions migrating into the Co_3O_4 spinel to form $CoAl_2O_4$ or $AlCo_2O_4$ spinel. While the cobalt oxide spinel and cobalt aluminate spinels have extremely similar diffraction patterns, there is a distinctive characteristic cobalt aluminate spinel peak at $2\theta = 49.0°$ that is not present in our reported diffraction pattern.[14] After indexing the diffraction peaks present in the sample annealed at 800°C, Bragg's law was utilized to determine interplanar spacing and calculate lattice parameters.[15] The lattice parameter calculated from the diffraction pattern was determined to be a = 8.073(8) Å, closely matching that of Co_3O_4 (a = 8.072(3) Å) and somewhat lower than that of $CoAl_2O_4$ (a = 8.106(6) Å) or $AlCo_2O_4$ (a = 8.087(2) Å). These initial results suggest that the cobalt present in the films crystallizes and phase segregates into a binary oxide, containing crystalline Co_3O_4 present in an amorphous Al_2O_3 network. To further understand the chemical composition of these films, XPS studies were performed. Figure 2.5 shows the cobalt 2p, aluminum 2p, and sulfur 2p XPS spectra of **CoAl** films that were annealed at

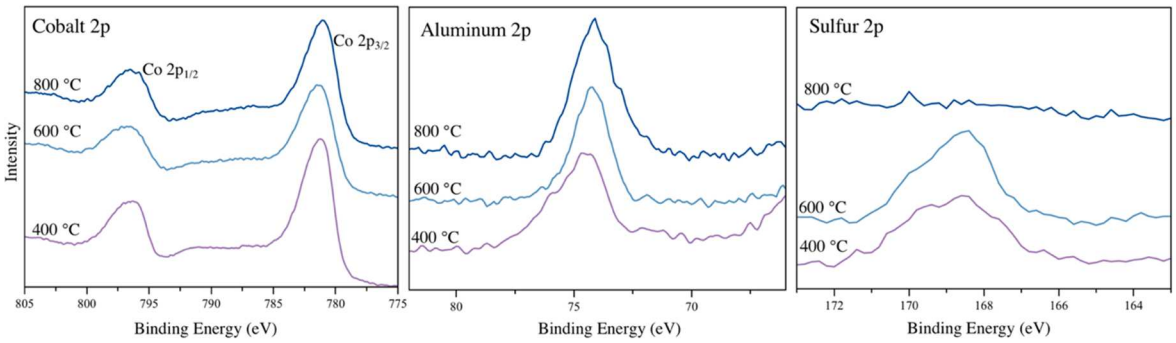

Figure 2.5. Cobalt 2p (left), aluminum 2p (middle), and sulfur 2p (right) XPS spectra of 1-layer **CoAl** films annealed at 400 °C, 600 °C, and 800 °C.

400 °C, 600 °C, and 800 °C. For cobalt, the peaks at 779.8 eV and 795.8 eV correlate to Co $2p_{3/2}$ and $Co_{1/2}$ respectively.[16] The satellite peaks indicate the presence of Co^{2+} and Co^{3+} oxidation states which can be attributed to the presence of the Co_3O_4 spinel. Lastly, the modified Auger parameter (1553.1 eV), is consistent with previously reported Co_3O_4 films further suggesting the cobalt in these films is comprised of Co_3O_4.[17] Additional analysis of the aluminum spectra supports the presence of Al_2O_3. The peak at 74.1 eV correlates to the aluminum 2p line and is in agreement with previously reported Al_2O_3 thin films.[18] Lastly, we investigated the sulfur content of these films. The films annealed at 400 °C and 600 °C show small amounts of sulfur (~1.0 at. %) from residual DMSO present as sulfate in the films. However, further annealing to 800 °C appears to remove all residual sulfur from the film.

With a clearer understanding of the composition of these films, we sought to further investigate their physical and morphological properties. XRR analysis determined single layer films to be roughly 22.0 nm thick with each additional layer increasing the thickness by approximately 20.5 nm (Figure 2.6).

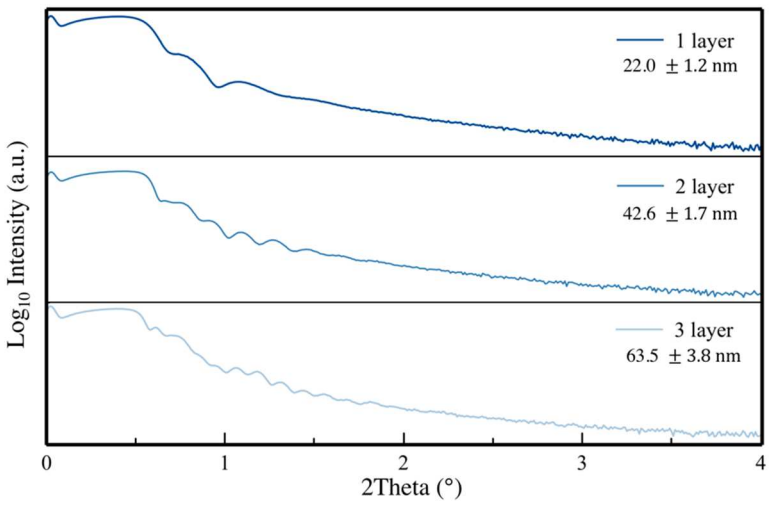

Figure 2.6. XRR diffraction pattern of 1-layer, 2-layer, and 3-layer **CoAl** films annealed in box furnace at 700 °C with corresponding film thicknesses.

Figure 2.7 shows the AFM scan of 5-layer **CoAl** films annealed at 400 °C and 800 °C. At 400 °C, the films approach near-atomic roughness with an R_{rms} of 0.517 nm. By increasing the annealing temperature to 800 °C, the roughness of the films is increased roughly 7-fold to an R_{rms} = 3.760 nm due to the emergence of crystallites on the surface.

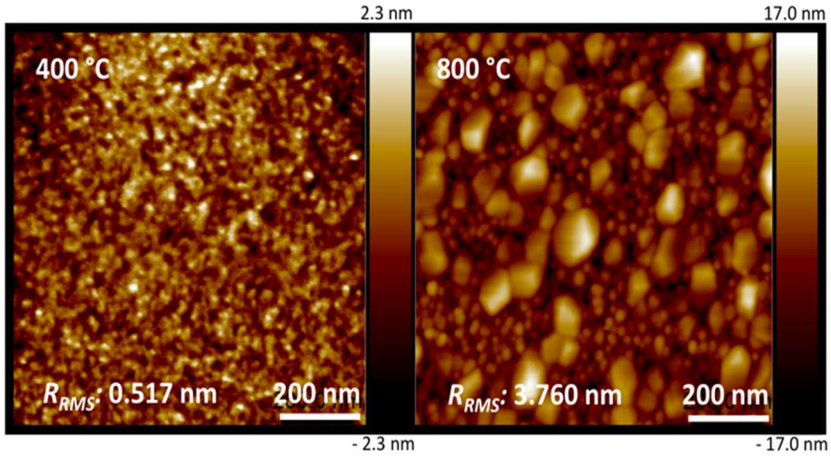

Figure 2.7. 1 μm^2 area AFM scans of 5-layer CoAl films annealed at 400 °C (left) and 800 °C (right)

A (SEM) investigation of these films shows the emergence and growth of crystallites as annealing temperature is increased (Figure 2.8). Additionally, SEM-EDS analysis was carried out to further probe elemental distribution and (approximate) ratio of the cobalt and aluminum in the film. Results indicate a uniform distribution of aluminum and cobalt throughout the film at each annealing temperature. This suggests that the Co_3O_4 crystallites propagate throughout the film, supported by an amorphous alumina matrix and are not just present at the surface. EDS analysis also confirmed a final film composition of 3 parts cobalt to 1 part aluminum, matching that of the starting **CoAl** cluster. This was expected due to the non-volatility of the deposited ions and previous work demonstrating

the trend between precursor and final film composition in solution-processed spin-cast films.[7,19]

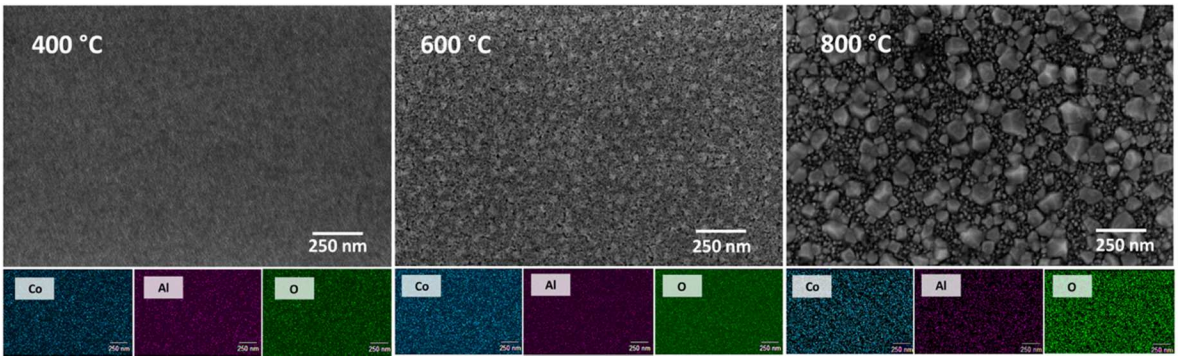

Figure 2.8. (Top) SEM images of **CoAl** films annealed at 400 °C, 600 °C, and 800°C with corresponding EDS scans of cobalt, aluminum, and oxygen (bottom).

To further probe the phase segregation apparent in these films, TEM images were collected. Figure 2.9 shows high-resolution TEM cross section prepared by focused ion milling of a 1-layer **CoAl** film annealed at 800° C. The milling occurred in a region of the film that did not contain any of the larger crystallites present at the surface. Analysis of TEM images and electron diffraction pattern further confirmed a polycrystalline film with a crystal structure matching the *d*-spacing of Co_3O_4. The TEM image also shows that the

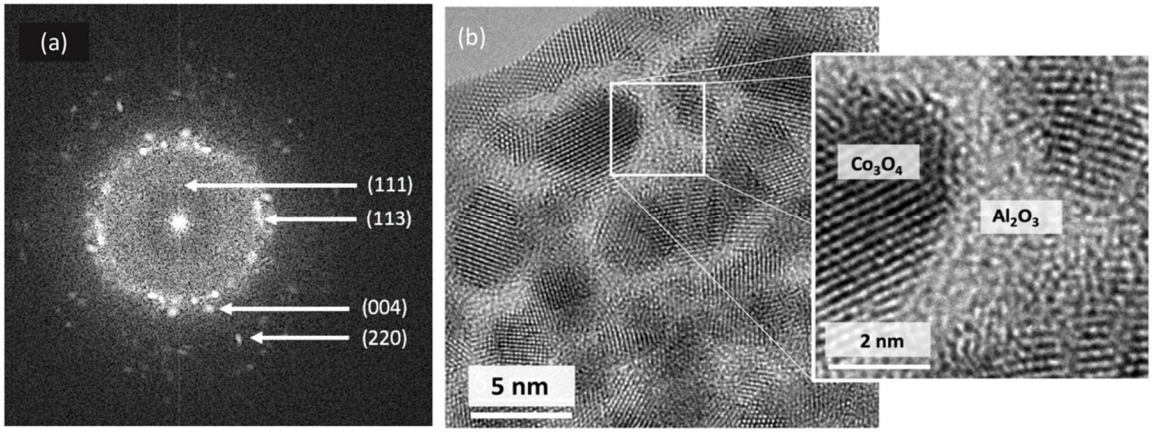

Figure 2.9. TEM image of single-layer CoAl film annealed at 800 °C showing clear crystalline and amorphous domains (b). Electron diffraction pattern from TEM image indexed to Co_3O_4 (a).

Co_3O_4 crystallites propagate throughout the entire film, supported by an amorphous Al_2O_3 matrix.

Analysis of SEM and TEM images suggest a variation in crystallite size as a function of annealing temperature. To further evaluate the size of crystalline domains in each film, the Scherrer equation was utilized:

$$d = \frac{K \cdot \lambda}{\beta \cdot \cos\theta} \qquad (1)$$

where d is the crystallite size, K is the Scherrer constant, λ is X-ray wavelength, β is the peak width (FWHM), and θ is the corresponding Bragg angle.[20] Table 2.1 displays the average crystallite size of the Co_3O_4 domains, demonstrating a near linear correlation between crystallite size and annealing temperature.

Table 2.1. Average crystallite size present in **CoAl** films.

Annealing temp (°C)	Crystallite size (nm)
800	19.3
700	14.1
600	9.9
500	4.0

With a full understanding of the composition in these **CoAl** films, we sought to investigate the optical properties of the fabricated films. Upon annealing, the deposited

films appeared pale-brown and transparent. The absorbance properties of the hot plate annealed and box furnace post-annealed layered films were recorded between 300 and 800 nm. Upon the post-annealing of the films, the absorbance of the films decreases as shown in Figure 2.10c. Figure 2.10a shows the absorbance spectra for the post-annealed **CoAl** films featuring 1-5 layers. A clear trend between the number of deposited layers and an increased absorbance can be discerned with a linear correlation between number of deposited layers and film absorbance at the λ_{max}. The two regions of optical transitions in the spectra correspond to the Co^{3+} 3d - Co^{2+} 3d at 685 nm and the O 2p – Co^{3+} 3d at 408 nm, consistent with previously reported Co_3O_4 films.[21,22] The optical response in these films is dominated by Co_3O_4, indicating that the amorphous alumina network does not contribute to the absorbance of these films in a significant manner. The observed optical data was further utilized to estimate the band gap energy for these films using the classical relation for optically induced transitions in semiconductors shown in equation 2:

$$\alpha = \frac{A(hv - E_g)^n}{hv} \qquad (2)$$

where α is the absorption coefficient, A is a constant, hv is the photon energy, E_g is optical band gap, and n is ½ for direct transitions and 2 for indirect transitions.[23] Figure 2.10b shows the plots of $(\alpha hv)^2$ and $(\alpha hv)^{1/2}$ vs hv for the 5 layer **CoAl** film annealed at 700 °C. Since the linear extrapolation of each plot appears in the domain of higher as well as lower energies, it indicates the presence of both direct and indirect optical transitions in these films.[24] Extrapolation of the linear region of each plot to the axis gives the indirect and direct optical band gap energies of 1.89 eV and 2.25 eV respectively. These results are

slightly higher than previously reported spray pyrolysis Co_3O_4 films with the minor difference being attributed to the amorphous alumina network present in our **CoAl** films.[25]

The results presented show a clear picture for the composition and characterization of the fabricated films. Despite the precondensed nature of the **CoAl** cluster, films annealed at 400°C appear to phase segregate instead of forming an alloy. This can likely be attributed to cobalt's non-zero ligand field stabilization energy and low oxidation state indicating that the formation of an amorphous structure would be energetically unfavorable compared to a crystalline one.[4] When these films are annealed to 800 °C, the phase segregation becomes more apparent, with TEM analysis showing a binary oxide containing crystalline Co_3O_4 present in an amorphous Al_2O_3 network. This correlates with previous reports showing that

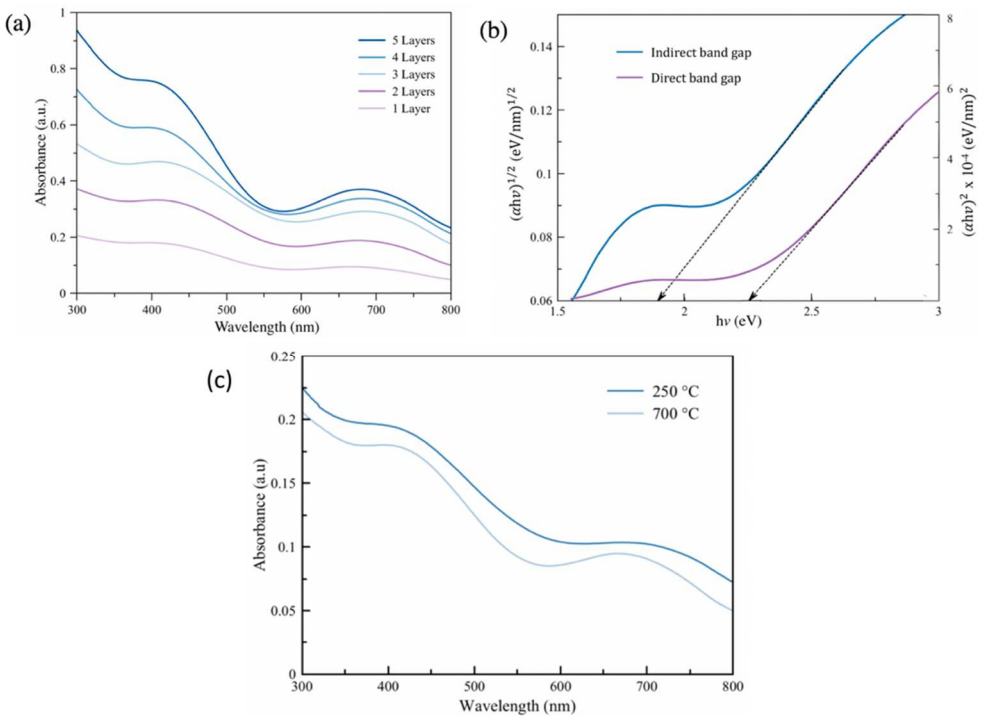

Figure 2.10. (a) UV-vis spectra of 1-5 layer CoAl films annealed at 700°C. (b) Band gap analyses of direct and indirect optical transitions for 5-layer CoAl film annealed at 700 °C. (c) UV-Vis spectra of 1-layer **CoAl** film after hot plate anneal at 250 °C and subsequent box furnace anneal at 700 °C.

cations with greater crystal field stabilization energy such as Co^{3+} will readily phase segregate into the corresponding oxide rather than form an amorphous aluminum oxide alloy.[26] We also present data investigating the crystallinity of these films. Annealed films are polycrystalline and the Co_3O_4 crystallite size grows almost linearly with temperature. This could perhaps be valuable for potential mixed metal oxide systems studying capacitance where polycrystalline films are preferred to amorphous ones as long as crystallite size doesn't exceed film thickness.[27]

Conclusions

In this work, polycrystalline mixed-metal cobalt aluminum oxide films were fabricated from a novel hexol-type cluster. Films were solution deposited via spin-coating and post-annealed at varying temperatures up to 800 °C. By varying the number of layers deposited and annealing temperature, we were able to discern morphological, compositional, microstructural, and optical properties of these films. After spin coating and annealing the films up to 800 °C, the aluminum and cobalt phase segregate to form polycrystalline Co_3O_4 in an amorphous Al_2O_3 network. As annealing temperature increases, the Co_3O_4 crystallite size increases as well. The optical properties of these films can be tuned by varying the number of layers deposited, and the Co_3O_4 present in these films dominates the optical response, exhibiting both indirect and direct optical transitions. These results confirm that the **CoAl** cluster ($Al[(u\text{-}OH)_2Co(NH_3)_4]_3(NO_3)_6$) can be used as a precursor to produce high quality mixed metal oxide thin films. The successful fabrication and subsequent characterization of these films warrants future studies into similar films fabricated from hexol-type derivatives previously reported in literature.

Bridge to Chapter III

The presented work in Chapter II is an excellent demonstration of the solution deposition process. The process began with an inorganic synthesis to isolate the desired cluster. Then, the cluster was dissolved to produce a precursor solution that was deposited on a silicon substrate via the spin-coating method. Lastly, the films were annealed in a box furnace to produce the final mixed-metal oxide. Once the films were produced, a fleet of microstructural characterization techniques were deployed to characterize the optical, morphological, microstructural, and elemental properties of these films. These steps generalize the solution deposition process and will demonstrated again in the chapters to come. However, while working on the presented **CoAl** work in Chapter II, it became apparent how detached the presented work was from actual application implementation. We were able to show the viability of the **CoAl** cluster to produce high-quality films, however it was not entirely apparent how these films could be utilized for immediate impact on applications. In Chapter III however, we demonstrate the immediate industrial applications of solution deposited coatings. The work in Chapter III will provide a process for solution deposited thin films that was developed specifically for industry to provide an immediate industrial impact.

CHAPTER III

DEVELOPMENT AND OPTIMIZATION OF AN ALUMINUM OXIDE COATING ON PYROLYTIC GRAPHITE

Introduction

Thermal management is an extremely important factor in high temperatures applications in a wide variety of industries including, aerospace, electronics, and semiconductor industries. It is crucial in these applications to properly control heat flow and ensure that processes have uniform heat distribution. For example, thermal heat management systems are widely utilized in the aerospace industry where their air and space based equipment utilize high powered microelectronic circuitry that can generate extreme heat. When exposed to harsh environments, it is vastly important to avoid these systems overheating which could greatly limit their performance or lead to system failure.[1] Additionally, in the semiconductor industry, heat spreading materials are used as "heat sinks" to dissipate heat generated by the semiconductor in order to ensure high quality device performance.[2]

Materials classified as heat spreaders exhibit relatively high thermal conductivity (~ 100 W/m°K or greater), and show resistance to high temperatures. There are currently a variety of heat spreading materials industrially available, with copper and aluminum being some of the most commonly used heat transport materials. One alternative heat spreading material currently on the market is pyrolytic graphite (PG). PG is a carbon based material made up of layered sp^2 hybridized carbon 2-dimensional sheets layered on top of each other (Figure 3.1). The Van der Waals forces in the c-lattice direction makes pyrolytic

graphite unique and gives it anisotropic properties where the thermal conductivity of the *ab* plane is much higher than that of the *c* plane.[3]

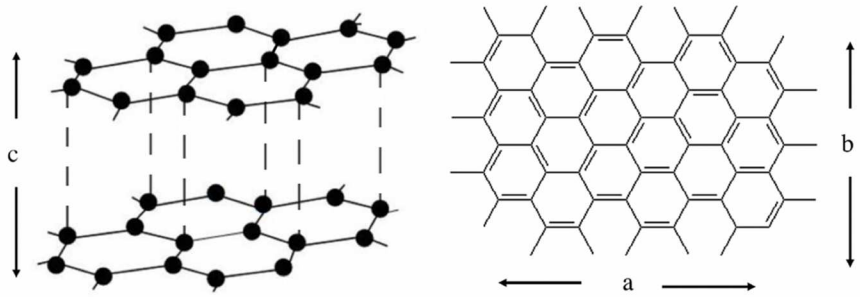

Figure 3.1 Structural depiction of *c* planes of pyrolytic graphite showing Van der Waals interaction (dashed line) between planes (left) and sp^2 hybridized covalently bound carbon in the *ab* plane (right).

MinTEQ International's (MTI) Pyrogenics group is one of the industry leaders in the manufacturing of pyrolytic graphite. Their high thermal conductivity PG (PYROID HT, PGHT) exhibits "five-nine" purity (99.999% pure), is incredibly stable at high temperatures (>2500 °C), and is resilient to ions and other reactive gasses. Additionally, the PGHT's *ab* plane exhibits extremely high thermal conductivity (1700 W/m°K). That value is 8 times more conductive than aluminum and 4 times more conductive than copper, making it an excellent heat spreading material, as shown in Figure 3.2.[4,5] What makes MTI's product truly exceptional is their proprietary PG growth method that allows for PG to be tailored to specific shapes and complex dimensions. This versatility in their growth method has enabled them to produce PG for a wide variety of high temperature heat spreading applications.

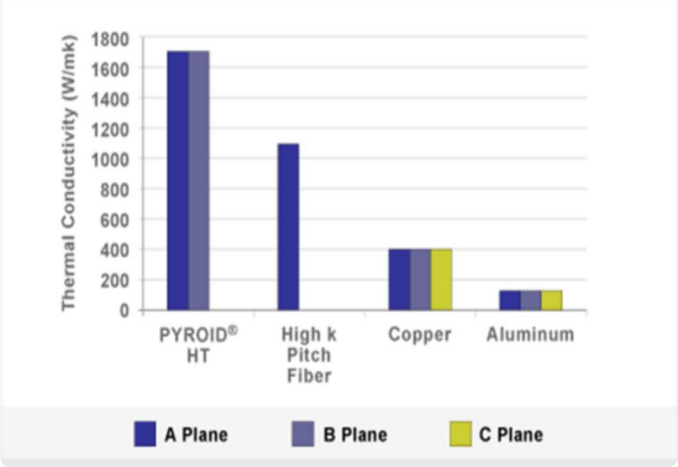

Figure 3.2. Thermal conductivity of MTI's PYROID HT compared to other commercially available heat spreading materials.[4]

While MTI is interested in expanding the utilization of PG into new industries and applications, they are hindered by PG's natural propensity to delaminate. Due to the unrefined surface of the PG as shown in Figure 3.3, the potential exists for graphitic flakes to delaminate from the surface and dislodge from the material. Because of the electrically conductive nature of PG it can cause issues in an application that would be sensitive to conductive particles, such as microelectronics.

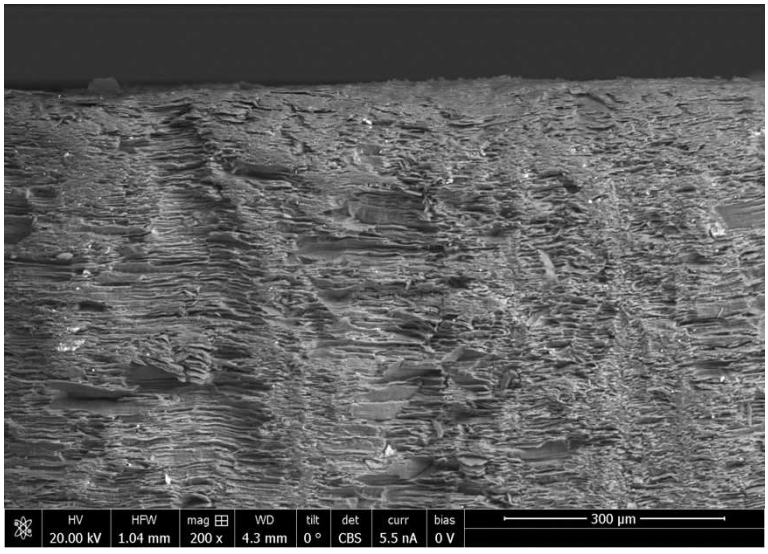

Figure 3.3 SEM image of the surface of pyrolytic graphite. Image is taken parallel to the *ab* plane and demonstrates the layered nature of the material.

In order to avoid the release of conductive graphite flakes from the PG surface, the material needs to be fully encapsulated in a protective coating that would prevent the generation of deleterious particles, without inhibiting its thermal conductivity. To meet these criteria for a coating material, the added coating has to be thermally conductive and exhibit a similar coefficient of thermal expansion (COE) to that of the PG. With these properties in mind, aluminum oxide was chosen as the selected encapsulation material.

Aluminum oxide, Al_2O_3, is an excellent encapsulation material as it is thermally conductive, water repellent, and electrically insulating. Additionally, Al_2O_3 is chemically resistant to materials and gasses which are otherwise troublesome for bare PG (O_2, as a primary example). Due to the UO's experience and published literature on producing Al_2O_3 coatings, a collaboration to encapsulate MTI's PG with Al_2O_3 seemed particularly promising. Additionally, the Darren Johnson lab's experience with solution processed coatings would allow for a significantly more scalable approach to the Al_2O_3 coatings, as compared to techniques such as atomic layer deposition (ALD). Utilizing the advantages of solution processing would provide MTI with a much more scalable process than that of current industrial methods used such as ALD or vacuum deposition that do not allow for flexibility in sample shape and size.

The following chapter will detail the trials, errors, and successes in providing MTI with an Al_2O_3 coating for PG that exhibits good aerial coverage and sufficient adhesion, in a scalable process that MTI can easily implement into their workflow.

Assessing morphological concerns of PG surface

Before any Al_2O_3 coatings were attempted, the surface of the PG had to be modified in order to allow for sufficient adhesion with an Al_2O_3 coating precursor. There were two initial challenges presented by the PG that needed to be addressed before substantial coating experimentation could take place. These challenges, addressed below, include the rough morphology of the PG and the inherently hydrophobic nature of the carbon-based material. All coatings and experimentation were performed on PG samples provided by MTI that exposed the *c* plane of the PG and were pre-cut to either 2 cm x 2 cm x 0.75 cm (Figure 3.4 left) or 1" x 1" x 0.1" (Figure 3.4 right).

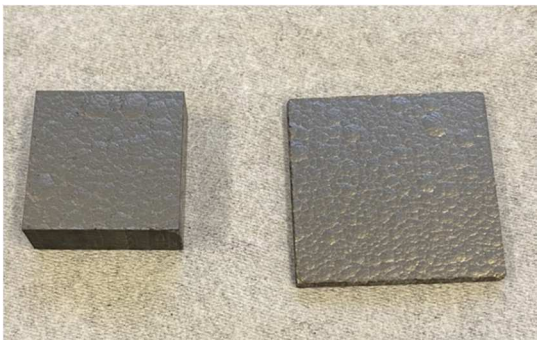

Figure 3.4 PG samples provided by MTI for experimentation.

PG surface polishing

The first challenge to address was the rough morphology of the PG, which could lead to incomplete coatings with non-uniform thickness. The morphology of the PG samples was initially assessed by 3D SEM photogrammetry (discussed further in Chapter 5). Analysis via this method showed that surface topographical features of the PG could be as large as 15 microns (Figure 3.5) indicating an extremely rough surface.

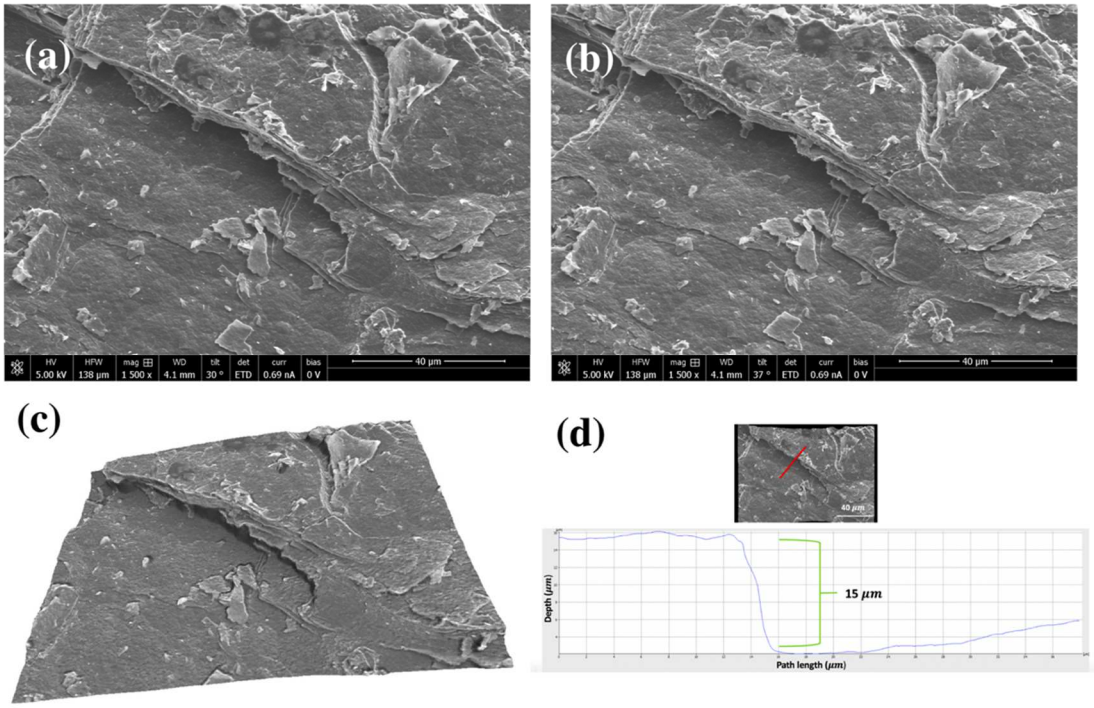

Figure 3.5 SEM image of surface of PG tilted at 30° (a) and 37° (b). 3D SEM reconstruction of PG surface (c) and corresponding profile analysis of reconstruction (d).

In order to assess coverage and adhesion in a more controlled and systematic approach, it was decided to polish the PG so that the coatings could be assessed on PG surfaces that had less variability between samples. Films were polished in a Struers Roto-Pot 35 with 3 varying grits. Samples were polished back and forth for 60 seconds on a rotating stand with 1200 grit sandpaper attached. This was then repeated with a 9 micron polishing pad, and 3 micron polishing pad. Figure 3.6 shows SEM images displaying the morphological difference between polished and unpolished substrates. By polishing the PG substrates, surface features were reduced to less than 1 micron in height.

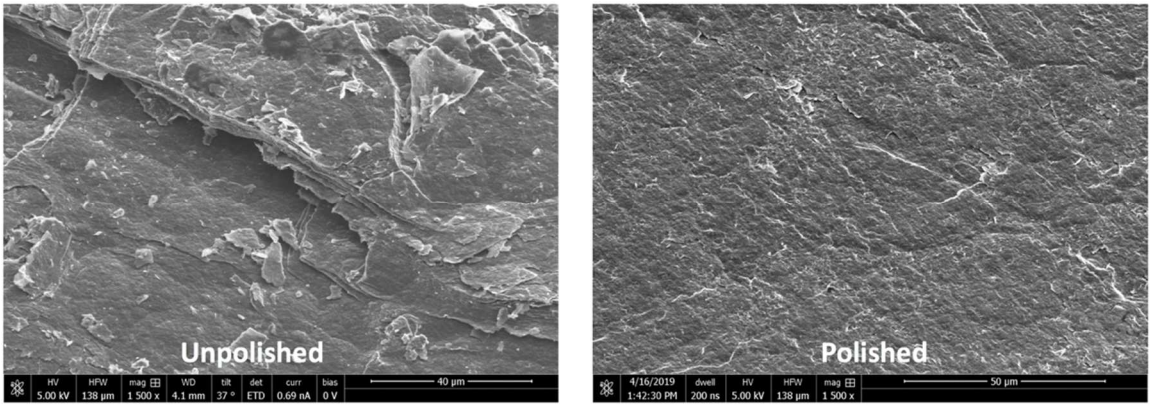

Figure 3.6 SEM images showing unpolished (left) and polished PG (right).

PG surface activation

The second challenge to address was the inherent hydrophobicity of the PG surface. Since most of our anticipated coating precursors were anticipated to be deposited from a water-based solution, a hydrophilic surface was necessary to achieve high surface wetting and enhanced coating adhesion. Therefore, it was important to "activate" the PG, incorporating polar hydroxyl groups onto the surface, making it more tolerant of aqueous or polar solvents. This surface modification of the PG was initially accomplished through the use of an oxygen plasma chamber (Plasma Etch Inc. Model PE-50). The plasma contains a combination of electrons, positive ions, UV light and reactive oxygen species that allows for the incorporation of polar groups onto the PG surface. Figure 3.7 below shows how the contact angle of water on unpolished PG decreases with varying plasma times. The contact angle of the water has been measured using a contact angle goniometer. As the plasma time increases, the wettability of the PG surface also increases allowing for the dispersion of water. Based on the results, all future PG samples were placed in the plasma chamber prior to coating with Al_2O_3 precursors.

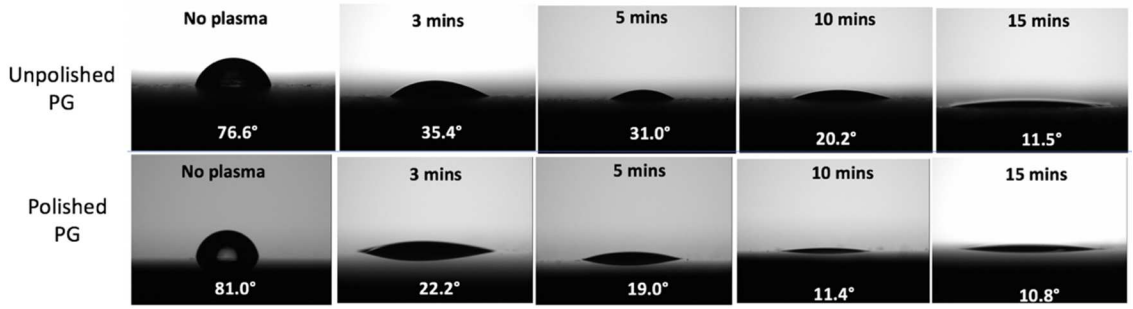

Figure 3.7 Contact angle results of unpolished and polished PG plasma treated at varying times

In an effort to make the PG pre-processing more scalable, and easier for MTI to incorporate into their workflow, it was important to improve the surface activation process of the PG. While good results were achieved from activating the surface via plasma, there was also reason to provide solution based alternatives that would allow MTI to treat a variety of sample sizes that wouldn't necessarily fit into a conventional plasma chamber. To address this, PG samples were soaked in a variety of oxidizing solutions at varying times and temperatures. This method seemed promising as it was utilized by Saberi et. al. to activate the surface of graphite in efforts to coat it with $MgAl_2O_4$.[6] After multiple attempts and some parameter optimization, it was determined that soaking the PG substrate in a heated oxidizing solution and letting the sample rest in the solution for 3 to 6 hours activated the surface and achieved similar contact angle results to plasma treated PG. These results are shown in Figure 3.8.

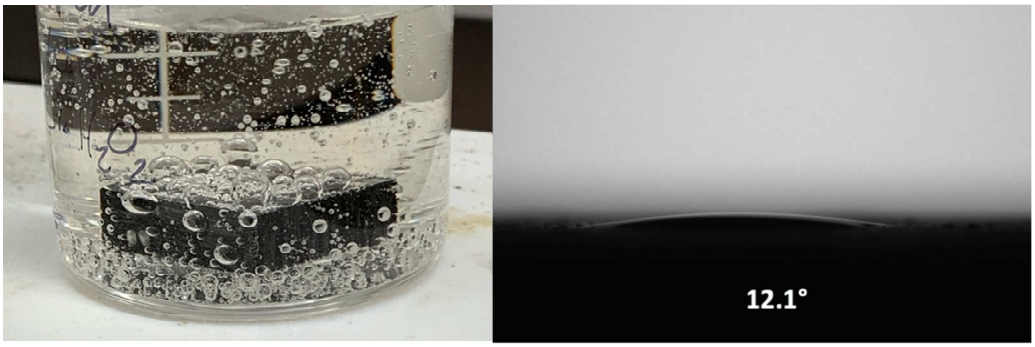

Figure 3.8 PG sample soaking in oxidizing solution (left) and subsequent contact angle(right).

In addition to the pretreatment, all unpolished samples were subjected to sonication in a Branson 2510 ultrasonic cleaner before any surface activation. The goal of the sonication was to dislodge any graphitic flakes that could easily delaminate during the coating process. Samples were placed face down in DI water and sonicated for 10 minutes before being removed, rinsed with DI water, and air dried.

Unsuccessful Al_2O_3 coating attempts

Al_{13} dissolution method

The first attempt at Al_2O_3 coatings was an innovative synthetic approach developed at the University of Oregon. This approach, termed the "dissolution method" by Fulton et. al., allowed for the direct synthesis of the flat-Al_{13} cluster, $[Al_{13}(\mu_3\text{-}OH)_6(\mu\text{-}OH)_{18}(H_2O)_{24}](NO_3)_{15}$ via the stoichiometric dissolution of bulk $Al(OH)_3$ in HNO_3.[7] In this work, Fulton et. al. presented a single-pot synthesis of the Al_{13} cluster , that formed a single product and didn't require any post-synthetic purification. This synthetic method initially appeared to be the most appropriate precursor synthesis method due to the ease of use, scalability, and advantages of the flat-Al_{13} cluster. The Al_{13} cluster shown in Figure 3.9, has been shown to be a viable precursor for dense Al_2O_3 films due to its' precondensed

aluminum-oxygen network and reduced aluminum to nitrate ratio.[8] Additionally, since the Al_{13} cluster is soluble in environmentally benign solvents, it allows for a wide variety of scalable solution deposition techniques to be utilized. To fabricate the Al_{13} cluster via the dissolution method, solid $Al(OH)_3 \cdot 0.7H_2O$ is dissolved in 5 M HNO_3 (aq). Due to the stoichiometric amount of nitric acid in solution compared to aluminum (15:13), the cluster forms and becomes the dominant species in solution with no necessary post-synthetic steps.

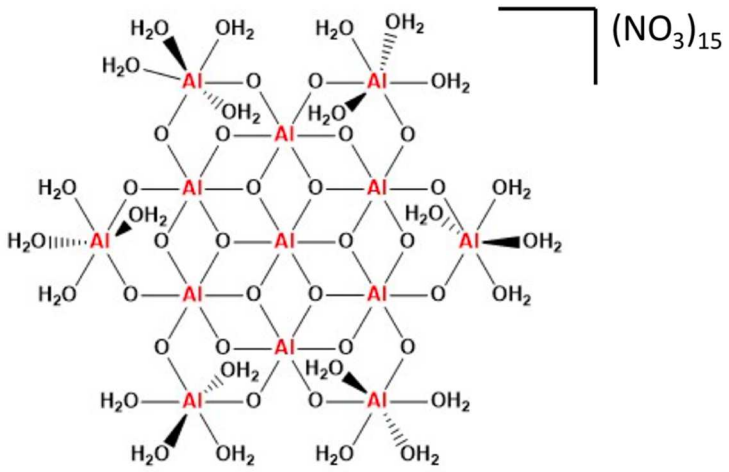

Figure 3.9 Chemical structure of flat-Al_{13} cluster.

Initial experiments were structured around varying the concentration of the precursor solution, organic additives, coating method, and processing temperature of the PG. Despite numerous attempts varying these parameters, successful coatings could not be produced. All of the produced coatings exhibited significant issues with large scale cracking of the deposited film. Large scale cracking on films was apparent after annealing of films. Optical microscope images showed smaller scale cracking, as well, as shown in Figure 3.10.

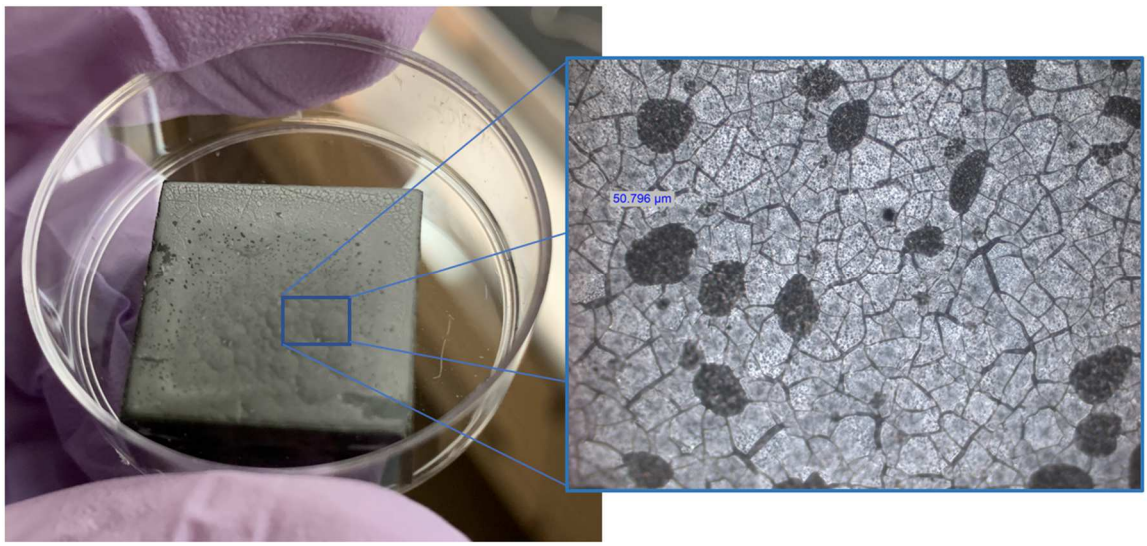

Figure 3.10 Optical image of Al_2O_3 coating produced from Al_{13} dissolution method.

In addition to the films exhibiting major cracking, there was another issue that caused concern. Regardless of how the PG surface was activated before coating, no adhesion to the PG surface was observed. Testing of the resulting coatings showed that a simple "tape test" was enough to remove the coating from the PG surface, as shown in Figure 3.11.

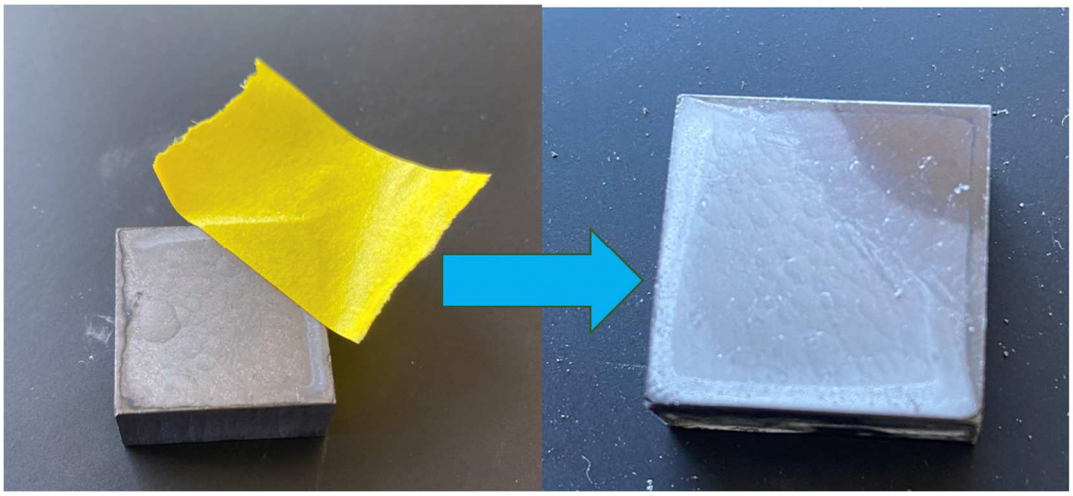

Figure 3.11 Adhesion results from tape test on film produced from dissolution method. Image on right shows coating fully removed in the region where tape was applied.

While the dissolution method of producing the Al_{13} cluster has many advantages such as ease of synthesis and scalability, it also had significant disadvantages that hindered experimental progress. For instance, since the final product is suspended in an aqueous solution it was difficult to accurately determine and vary the concentration. This also made it difficult to experiment with different solvents as well. Attempts were made to resolve the cracking and adhesion issues, but they were not successful. It was at this point that the decision was made to attempt other Al_2O_3 precursor methods.

Al_2O_3 sol-gel synthesis

After unsuccessful attempts using the dissolution method, other published solution based sol-gel coatings were attempted. In this work, Jing et. al presented an approach to crack-free alumina films with the use of aluminum *sec*-butoxide (ASB) precursor and ethyl acetoacetate (EAcAc).[9] They suggested that the EAcAc acted as a chelating agent and largely prevented crack formation in the films.

To fabricate the sol, aluminum *sec*-butoxide (ASB) was added dropwise to heated (80 °C) nanopure water (18 MΩ). After hydrolysis of the organometallic compound and subsequent heating of the solution for 3 minutes, ethyl acetoacetate (EAcAc) was added to the solution, followed by the dropwise addition of HNO_3 until the solution became transparent. Once the solution was formed, PG samples were dipped into the sol, allowed to dry at ambient temperature for 48 hours, then subjected to thermal annealing via a box furnace at 700 °C for 4 hours. After many attempts, a successful coating could not be produced using this method and all films appeared severely cracked, as shown in Figure 3.12.

While this sol-gel method was not successful, it did introduce the potential viability of EAcAc as an additive and this was utilized later in successful coatings.

Figure 3.12 Sample showing large scale cracking of Al_2O_3 after attempt to coat via sol-gel method.

Solution deposition with $Al(NO_3)_3$

After analyzing the unsuccessful results from the Al_{13} dissolution method it became clear that progress would need to focus on controlling the aluminum precursor concentration and on the nature of the solvent. Due to its high solubility, testing $Al(NO_3)_3 \cdot 9H_2O$ as the coating precursor allowed for the aluminum concentration to be precisely controlled and tested in a variety of solvents. Coating solutions were made by dissolving $Al(NO_3)_3 \cdot 9H_2O$ in a variety of solvents at different concentrations. Once the aluminum precursor was dissolved and solutions were transparent, they were filtered with a 0.45 micron filter and drop-cast onto the PG films and post-annealed in a box furnace. After attempting coatings in a variety of solvents, ethanol seemed the most promising and produced films that adhered to the surface of the PG. Figure 3.13 shows the coatings at a variety of concentrations.

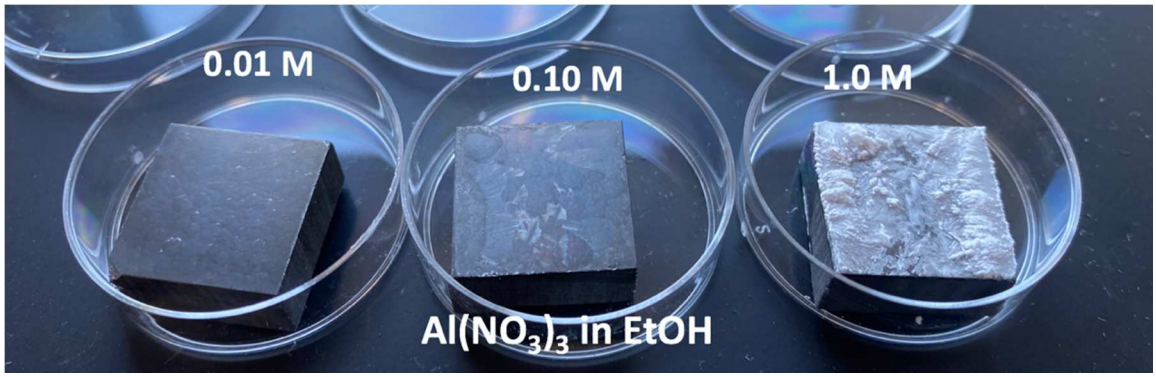

Figure 3.13 Al_2O_3 coatings made from varying concentrations of aluminum nitrate in ethanol.

After further analysis of these films via SEM it was determined that the lower concentration solutions (0.01M) produced an Al_2O_3 coating on the surface with sufficient adhesion and continuous coverage across the PG surface. From this point, the aluminum nitrate films were investigated further, and processing parameters were varied in attempts to produce the highest quality films. Unfortunately, the aluminum nitrate coatings on unpolished PG exhibited discontinuous coverage. This is shown in Figure 3.14, which compares the coatings to analogous, successful coatings produced from the Al_{13} cluster. The porous nature of the aluminum nitrate coating was due to a higher amount of nitrate groups that burn off from the film during annealing. After unsuccessful attempts to produce

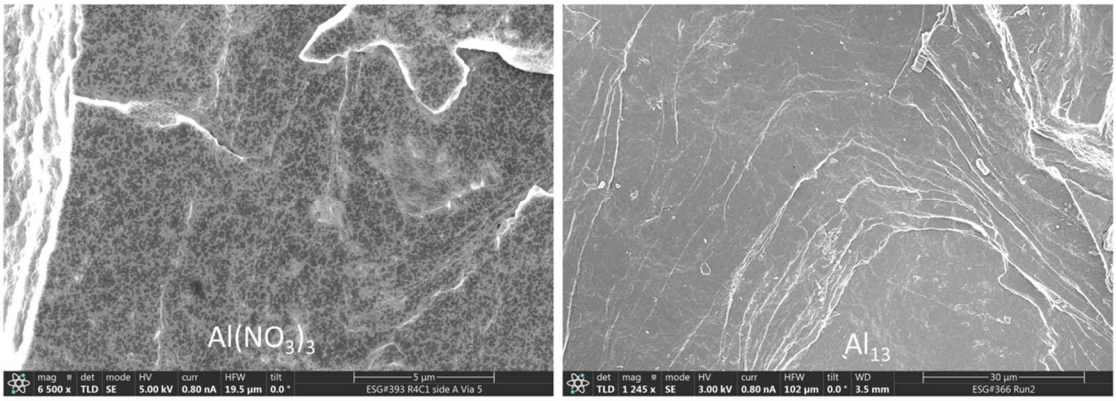

Figure 3.14 SEM images of Al_2O_3 coatings on unpolished PG from aluminum nitrate (left) and Al_{13} cluster (right).

homogenous coatings on unpolished PG, the Al_{13} cluster became the main focal point for all coating work moving forward.

Successful and optimized Al_2O_3 coatings

This section of the chapter will detail the precursor synthesis, coating process parameters, and coating characterization of the PG samples that were successfully coated from an Al_{13} precursor solution. The flat-Al_{13} cluster, $[Al_{13}(\mu_3\text{-}OH)_6(\mu\text{-}OH)_{18}(H_2O)_{24}](NO_3)_{15}$, was selected as the precursor of interest due to its ease of synthesis, solubility in environmentally benign solvents, ability to be solution processed, and low decomposition temperature. Additionally, the flat-Al_{13} cluster exhibits a higher aluminum to nitrate ratio than aluminum nitrate ($Al(NO_3) \cdot 9H_2O$). This leads to coatings that are denser and less porous than analogous films made from aluminum nitrate. Selecting a precursor that can be isolated as a solid also allowed for exact precursor concentrations to be determined before sample coating. The following results will display the coverage, thickness, and adhesion of the optimal Al_2O_3 coatings.

Preparing the precursor solution is a fairly simple process that can be easily scaled up and produced in bulk quantities. To begin, the Al_{13} cluster is synthesized and isolated using the Zinc reduction method presented by Wang et. al.[10] First, $Al(NO_3) \cdot 9H_2O$ is added to nanopure water (18 MΩ) and the solution is stirred. Once the aluminum nitrate is fully dissolved, zinc powder is slowly added to the solution. Once the zinc has fully dissolved, the solution was filtered to remove any residual zinc and the filtrate was collected and heated on a hotplate to precipitate out the final product. After the Al_{13} cluster precipitated from solution, the amorphous white powder was filtered, washed with solvents to remove

any residual zinc nitrate and aluminum nitrate, dried, and collected. Once isolated, the cluster was dissolved in an organic solvent to make precursor solutions in varying concentrations. These solutions were then cast onto the films in a variety of deposition methods including spin coating, drop coating, and spray coating. Once coated, samples were placed in a box furnace and annealed at varying temperatures with a ramp rate of 12.5 °C/minute.

To fully optimize the coating solution and processing conditions, the following parameters were investigated:

- $[Al_{13}]$
- [EAcAc]
- Solvent
- PG pre-coating annealing temperature
- PG post-coating annealing temperature
- Spray coating distance
- Number of coats

After significant trial and error varying the above parameters, an optimized coating with sufficient adhesion, continuous coverage, and scalable approach was determined. The following sections will detail the characterization of the optimized coatings.

Al_2O_3 coating coverage

In order to determine coating coverage, scanning electron microscopy (SEM) was utilized. The following section will show examples of Al_2O_3 coatings and how the coverage is assessed. Coverage was determined via a TLD detector on the SEM instrument that allowed for the greatest contrast between the PG and Al_2O_3 coating. Figure 3.15 displays the failure modes used to classify unsuccessful coatings:

Incomplete coverage	Large regions of PG substrate exposed
Discontinuous coverage	Coated regions appeared splotchy and non-uniform
Cracking	Coating appeared to have large scale cracks that exposed PG

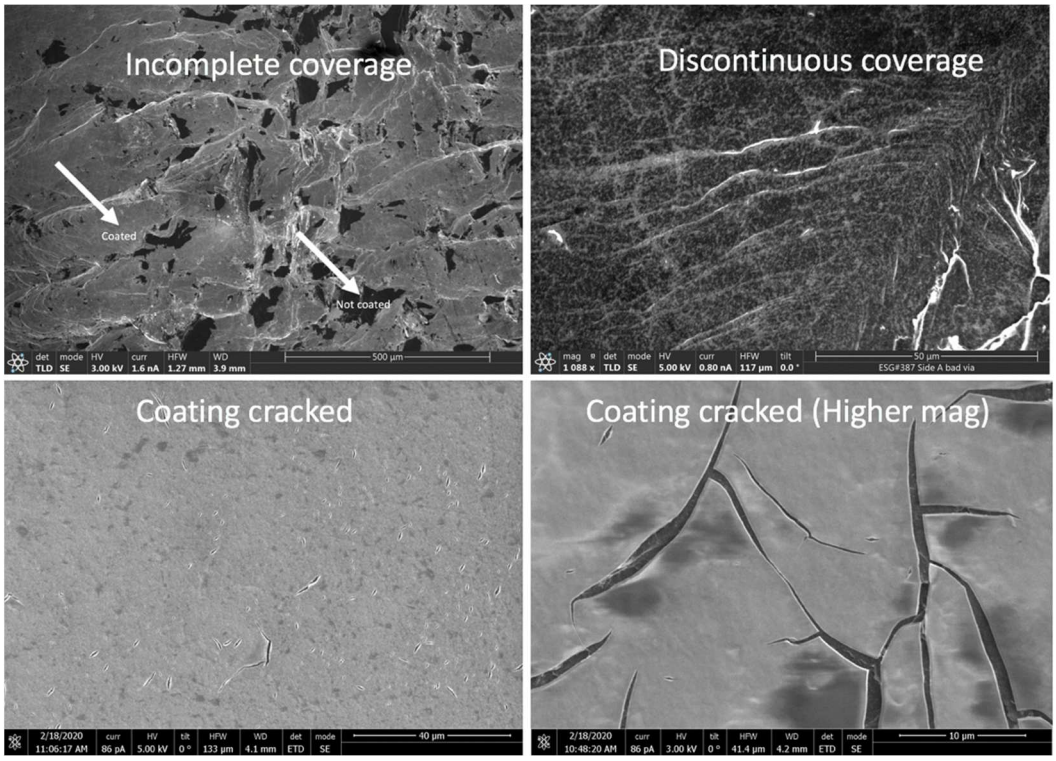

Figure 3.15 SEM images depicting the common coating failures that occur during coverage analysis.

Figure 3.16 demonstrates a successful coating, one that exhibits complete and uniform coverage with no presence of cracking. The first successful coatings were produced on polished PG that had been plasma treated.

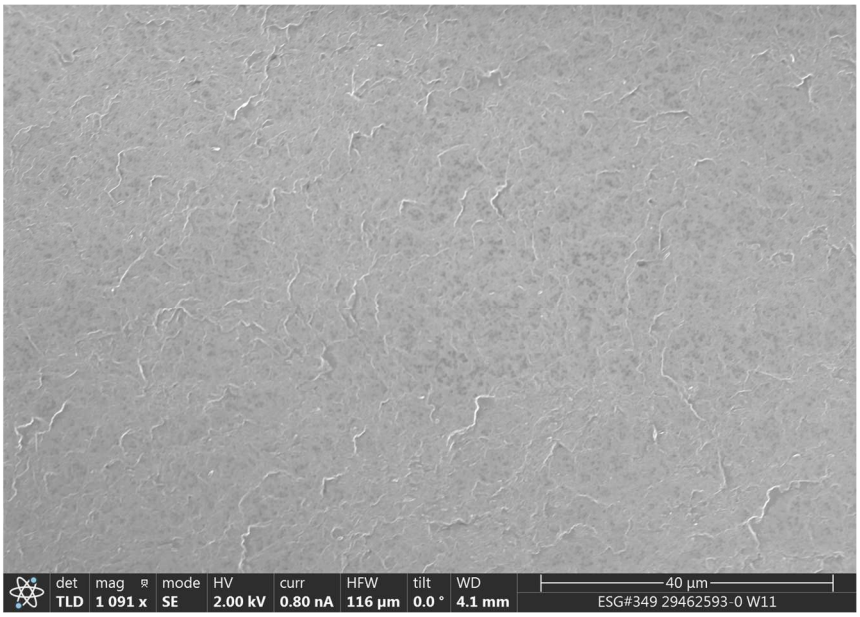

Figure 3.16 SEM image showing crack-free Al_2O_3 coating with full coverage on polished PG.

After accomplishing reproducible coatings on polished PG, it seemed important to attempt similar coatings on the unpolished PG as removing the need for polishing would be more scalable for MTI. By altering the coating concentration and formulation , similar successful coatings on unpolished PG were achieved, even in relatively rough regions (Figure 3.17).

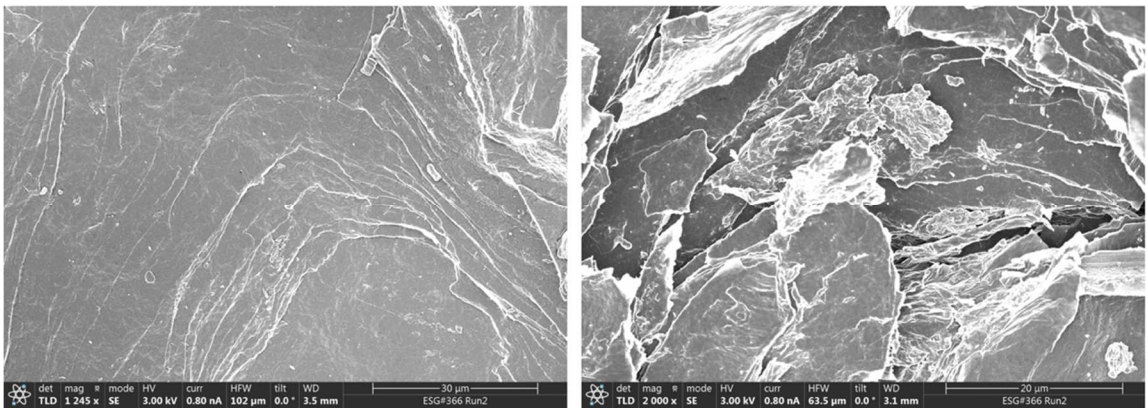

Figure 3.17. SEM image showing crack-free Al_2O_3 coating with full coverage on unpolished PG.

To demonstrate the elemental presence of aluminum oxide on the films, an EDX detector in conjunction with the SEM was utilized. Figure 3.18 displays the elemental spectrum of carbon, aluminum, and oxygen present in the sample.

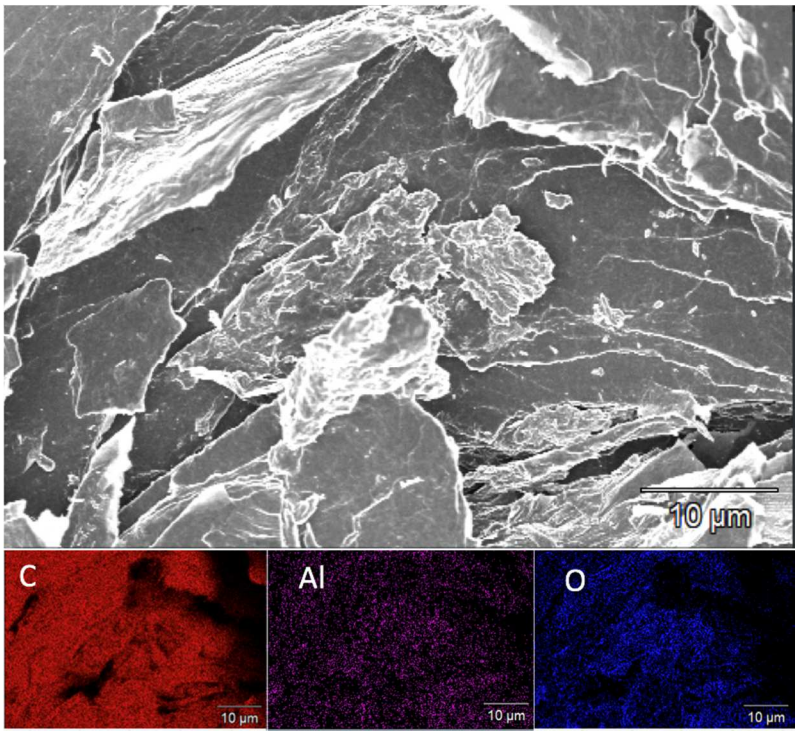

Figure 3.18 SEM-EDX image with elemental mapping of carbon, aluminum, and oxygen.

In an effort to further improve scalability, it was important to investigate how activating unpolished PG in an oxidizing solution would affect the coverage. As shown in Figure 3.19, similar coverage was achieved on unpolished samples when using the same spray coating parameters. It should be noted however that this process is not as reproducible as plasma treated unpolished samples.

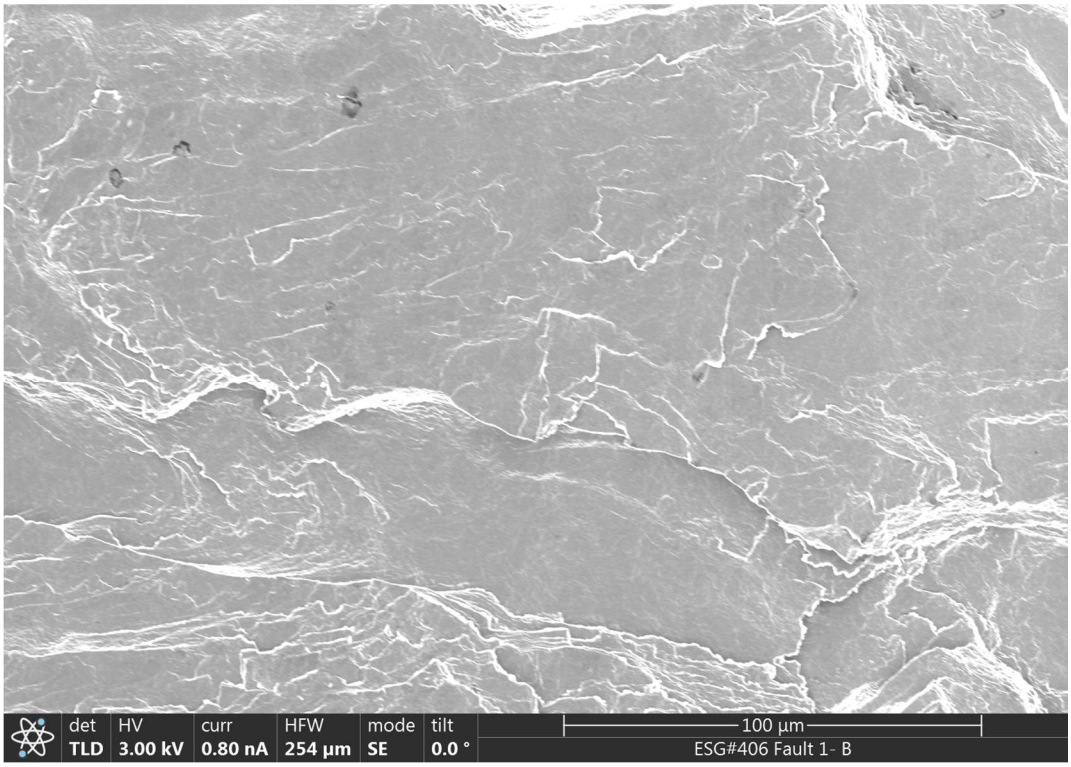

Figure 3.19 SEM image showing crack-free Al_2O_3 coating with full coverage on unpolished PG.

Al_2O_3 coating thickness

Figure 3.20 demonstrates a cross-sectional SEM image utilized to determine coating thickness. On average, 3 layer films range from approximately 121 to 149 nm in thickness. This thickness is below the critical thickness level where coatings have been shown to crack or sinter.

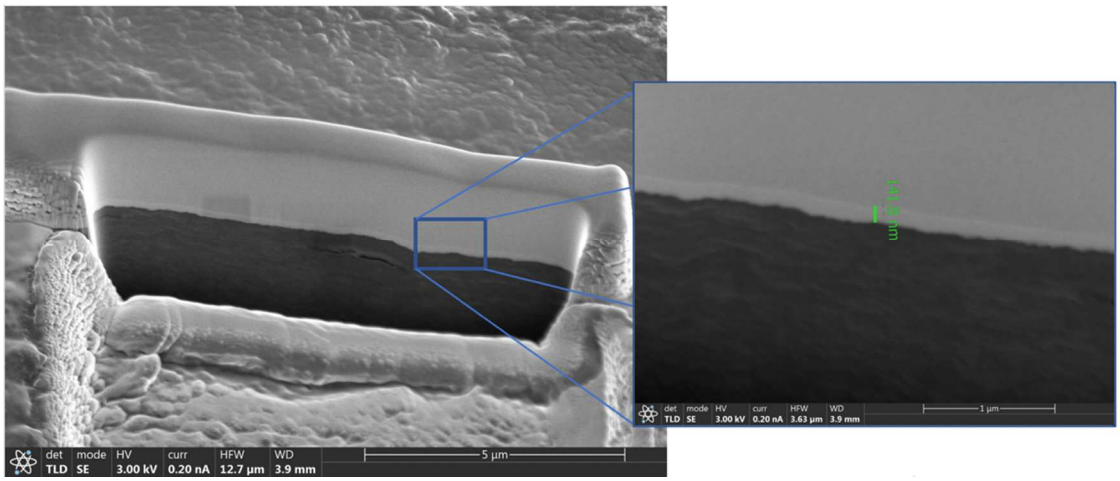

Figure 3.20. Cross-sectional SEM image showing thickness of Al_2O_3 coating on polished PG.

Al_2O_3 coating adhesion

In order to determine adhesion of the Al_2O_3 on PG, MTI contracted Quad Group Inc to perform adhesion tests. Adhesion was determined through a stud pull test in which a stud was adhered to the sample via epoxy and cured at 150 °C for one hour. A variety of Al_2O_3 coated PG samples produced with different processing conditions were subjected to the pull test. The adhesion strength and failure mode are presented in Table 3.1. The following list demonstrates the possible failure modes that could occur during the stud pull:

Coin	Total removal of coating
Coating	Coating failure, more than 30% of the Coating left on the sample.
Partial Coating	Partial Coating failure, less than 30% of the Coating left on the sample.
Epoxy	The epoxy failed cohesively, leaving epoxy on both the stud and the sample.

Cohesive coating	The coating failed cohesively leaving coating on both the stud and the sample.
Stud detach	The stud detached from the epoxy (epoxy on sample not on stud).
Substrate	The cohesive strength of the substrate was less than the adhesive strength of the bond.
Mismount	The stud was not mounted properly on the sample.

Figure 3.21 presents an example of a substrate failure mode where the stud removed all of the coating and some of the substrate.

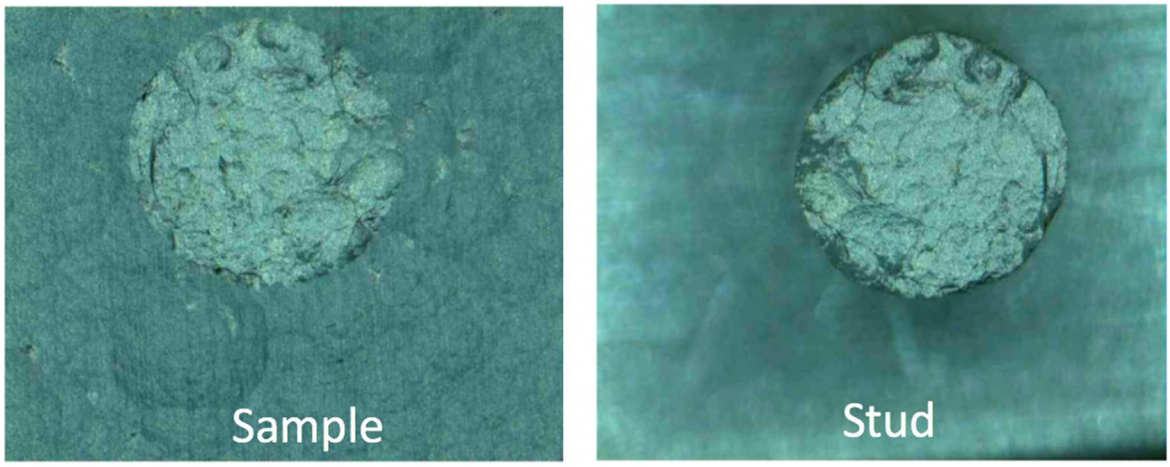

Figure 3.21 Images showing the sample (left) and stud (right) after the pull test has been performed.

Table 3.1 Adhesion test results of Al_2O_3 coated PG

Testing conducted November 2, 2020 with 901106 Studs at pull rate of 0.3 lbs/sec.					
Sample lot Number		Force (lb)	Stud	Adh. Str. (psi)	Failure Mode
1		1.7	0.106	193	Substrate
2		1.5	0.106	170	Substrate
3		2.0	0.106	227	Substrate
4		2.1	0.106	238	Substrate
5		1.5	0.106	170	Substrate
6		1.1	0.106	125	Substrate
7		2.1	0.106	238	Substrate
8		1.2	0.106	136	Substrate
9		1.4	0.106	159	Substrate
10		1.2	0.106	136	Substrate
11		0.9	0.106	102	Substrate
12		1.5	0.106	170	Substrate
13		2.4	0.106	272	Substrate
14		2.2	0.106	249	Substrate
15		1.6	0.106	181	Substrate
16		1.6	0.106	181	Substrate
Max (psi)	Min (psi)	Mean (psi)		Standard Deviation	Percent Standard Deviation
271.96	101.99	184.14		48.87	26.54%

The results indicate that regardless of polishing, and type of surface activation, the presented Al_2O_3 coatings are adhered more strongly to the surface of the PG than the adherence of the PG substrate layers themselves. If the Al_2O_3 coating had been weakly bound to the PG surface, the expectation would be for a "coin" failure mechanism, which is not present in the data. The data also suggests that unpolished samples exhibit slightly stronger adhesion forces than polished samples. Overall, all of the coatings tested exhibit sufficient adhesion to the PG surface.

Scalability of fabrication process

The presented research offered not only the opportunity to assess the viability of the presented coatings, but it also allowed for significant process engineering to take place in order to provide a more scalable process for MTI to implement.

During the coating optimization process, there was a point reached where the coatings exhibited strong adhesion, uniform coverage, and high reproducibility. Perhaps if

this were simply an academic research project investigating the viability of aluminum oxide coatings on pyrolytic graphite, then the project would have been deemed a success at this point. However, while the optimized precursor formulation and fabrication process produced acceptable coatings, it was not a process that MTI could easily scale up. For instance, the PG substrates needed to be polished, and activated via plasma chamber before any coatings could be added. Also, after the PG substrates were properly prepped, the precursor solution was dropped onto the surface using a plastic pipette. This fabrication process was highly controllable in a lab setting where all of the samples were the exact same size and the exact amount of solution deposited could be controlled. However, since it was crucial to MTI that the production process needed to be adaptable to substrates of complex shapes and sizes, it was clear that steps had to be taken to improve the scalability.

One of the first changes made was the solution deposition technique. Instead of deposition via drop-casting, a process was developed to coat the samples via spray coating (Figure 3.22). This process involved optimizing the precursor formulation to be more suitable for this method. The presented report shows that successful films were achieved using this method, a great step towards improving scalability.

Figure 3.22 Schematic depicting airbrush used for spray coating fabrication.

In addition to altering the fabrication method, it seemed important to change the substrate preparation method as polishing and plasma treating the PG films is a time consuming process that may not be suitable for substrates with complex shapes. Significant time and optimization were spent developing a process that could be produced on unpolished films that were activated via oxidizing solution. The reported results conclude that these scalability initiatives were achieved and homogenous Al_2O_3 coatings with full coverage could be achieved with the improved processing conditions.

Conclusions

The University of Oregon entered into a collaboration with the MinTEQ international's Pyrogenics division to provide them with an aluminum oxide coating method for their heat spreading material, pyrolytic graphite. After a significant amount of work aimed at varying processing parameters to find an optimum production process, the presented report shows that Al_2O_3 coatings with full coverage and strong adhesion on PG can be produced reproducibly. Additionally, the coating process is scalable, easy for MTI to incorporate into their current workflow, and can be performed on polished and unpolished PG regardless of surface activation technique. This coating process is currently in the process of being commercialized by MTI and evaluated for heat spreading properties of the coated PG materials.

Working with MTI has been an incredible opportunity and has provided incredible and invaluable experience of working with industry. Additionally, due to the successful nature of this work, the door is open for potential future collaborations between the University of Oregon and MinTEQ International.

Bridge to Chapter IV

The work presented in this chapter demonstrates the industrial viability of the solution deposition and demonstrates how this process can have an immediate impact on enhancing industrial processes. Additionally, this chapter highlights the benefits of the f-Al_{13} cluster to produce dense Al_2O_3 coatings can be easily scaled up. This work was leveraged in Chapter IV to provide a low temperature approach to forming water repellent Al_2O_3 coatings on textiles. In Chapter IV the advantages of the f-Al_{13} cluster are on full display and the sustainability benefits of solution processing takes center stage.

CHAPTER IV

A SIMPLE, SCALABLE, ECO-FRIENDLY AND ULTRALOW-TEMPERATURE APPROACH TO FORMING AL_2O_3 WATER REPELLENT COTTON COATINGS VIA UV PHOTO-ANNEALING

Authorship Statement

Some or all of the material in this chapter may appear in an upcoming publication authored by Jordan D. Levine, Alex Q. Rosen, Tawney A. Knecht, and Darren W. Johnson.

Introduction

The formation of hydrophobic coatings for textiles is of significant interest to a variety of industries, especially for the generation of waterproof apparel and footwear. The formation of these durable water repellents (DWR) has traditionally been fabricated using per- and polyfluoroalkyl substances (PFASs) due to their high level of water-repellent functionality and ease of deposition.[1] However, while these fluorinated coatings exhibit excellent hydrophobic performance, they are currently being phased out of a significant number of industrial processes.[2] This industry-wide change is due to the increasing health and environmental concern that PFASs pose. These substances have not only shown extreme environmental persistence and bioaccumulation[3], but they are also associated with cancer, toxic effects on the immune system, and even increased mortality rates.[4-6]

Since these PFAS's have been identified as problematic, there has been a continuing challenge to replace fluorine-based durable water repellents and replace them with greener alternatives.[7] In addition to being environmentally benign, it is important that

any proposed process requires minimal steps, can be processed at low temperatures, and can be easily scaled up for industrial implementation.

One interesting alternative being investigated as DWR on textiles is aluminum oxide (Al_2O_3). Al_2O_3 coatings are highly transparent, inexpensive to produce, exhibit strong hydrophobic properties, and are considerably less toxic than the currently used PFAS alternatives .[8] There have been many attempts to coat textiles with aluminum oxide, but none of them have provided a low energy, efficient, and easily scalable approach to forming a dense aluminum oxide coating containing little or no impurities. Lee et. al. has shown that Al_2O_3 coated cotton fibers exhibit extremely hydrophobic character; however, the coatings were formed using atomic layer deposition (ALD) under vacuum conditions, which is extremely energy intensive and only allows for small sample sizes suggesting this process would be very difficult to scale up.[9,10] In an attempt to provide a more scalable process, researchers have investigated a sol-gel based approach, in which textiles are soaked in an aluminum based sol and heated to form the alumina coated textiles.[11,12] While these approaches are more scalable than an ALD approach, there are significant drawbacks including the use of a microwave reactor, heating up to 160-170 °C, and the requirement of organic additives and ligands including ethyl acetoacetate (eacac) and sodium stearate to produce the final hydrophobic textile coatings.

While these ALD and sol-gel methods demonstrate the viability of aluminum oxide coatings, they fail to demonstrate the scalability needed to present a simple deposition approach that industry could readily adapt. One exciting solution to this challenge is the solution deposition fabrication technique of forming dense Al_2O_3 coatings. This process has been demonstrated on silicon substrates and has shown to produce Al_2O_3 coatings, with

no organic additive, spun-cast from an aqueous solution of the "flat" f-Al_{13} hydroxo cluster $[Al_{13}(\mu\text{-}OH)_{24}(H_2O)_{24}](NO_3)_{15}$.[13,14] The down-side of this approach is that formation of the final oxide coating requires thermal annealing of up to 500 °C, which would not be suitable for textiles that would decompose or auto-ignite at temperatures considerably lower. This relatively high processing temperature can be circumvented however by using deep ultraviolet (DUV) light (λ=185-254 nm) to photo-anneal the Al_2O_3 coatings.[15] This has been shown by Jo. et al. in which they demonstrated the fabrication of DUV photo-annealed Al_2O_3 films on silicon substrates, spun-cast from 2-methoxy ethanol solutions of $Al(NO_3)_3$ and f-Al_{13}. The combination of the DUV irradiation of the nitrate counterions and radiant heat from the mercury lamp (up to 160 °C) to remove residual solvent produced dense Al_2O_3 coatings that showed excellent dielectric properties.[16]

In this work, we utilize solution deposition and the DUV photo-annealing approach to produce hydrophobic Al_2O_3 coatings on cotton textiles. We believe this offers an easily scalable and low-temperature approach for forming Al_2O_3 coated textiles that requires no organic additives, can be deposited from environmentally benign solvents, and post-processed using only ultraviolet light, none of which are damaging to the underlying textile substrates.

Materials and Methods

Preparation of f-Al_{13} and $Al(NO_3)_3 \cdot 9H_2O$ precursor solutions

The f-Al_{13} cluster $[Al_{13}(\mu\text{-}OH)_{24}(H_2O)_{24}](NO_3)_{15}$ was prepared using a previously published method.[17] In this simple precipitation method, $Al(NO_3)_3 \cdot 9H_2O$ (Acros Organics) and zinc metal powder (Sigma-Aldrich) were dissolved in nanopure water (ρ =

18.2 MΩ cm) and filtered. The cluster then precipitates out of the filtrate solution as an amorphous white solid that was filtered, washed with isopropyl alcohol, and collected.

Preparation of UV-annealed textile coatings

A 10 mM precursor solution of the f-Al_{13} cluster was made in an acetone/water mixture and filtered through a 0.45 micron filter. For comparative studies, analogous $Al(NO_3)_3 \cdot 9H_2O$ solutions were prepared containing the equivalent aluminum concentration (130 mM). The precursor solutions were then drop cast or spray cast onto 2 x 2 cm square pieces of native cotton fabric using a Master G233 Pro Set airbrush with N_2 flow.

Once samples were coated with precursor solution, they were photo-annealed using a Novascan PSD Pro Series digital UV ozone system equipped with a mercury grid lamp emitting at 253.7 nm (90%) and 184.9 nm (10%). Samples were placed in the UV chamber, purged under N_2 atmosphere for 10 minutes and then subjected to 2 hours of UV treatment at ambient temperature. Radiant heat from the lamp increased the temperature to 30 °C. Samples that were thermally annealed were placed on a hot plate and heated at 120 °C for 1 hour. The prepared samples are labeled based on the precursor used and the relative post treatment. For instance, a native cotton sample treated with the f-Al_{13} cluster precursor solution and post annealed using UV light and thermal will be labeled as "Al_{13}-UV/Thermal".

Characterization

The UV-absorbance of the aluminum precursors were measured using an Agilent Technologies Cary 60 UV-Vis photospectrometer measuring from 190 nm – 800 nm. Surface morphology images and composition were determined by scanning electron microscopy (SEM) and energy dispersive X-ray spectroscopy (SEM-EDS) using a ThermoFisher Helios Hydra Plasma FIB. To determine surface roughness of samples, atomic force microscopy (AFM) images were collected using a Bruker Dimension Icon atomic force microscope equipped with FastScan scanning 2 μm^2 areas of individual sample fibers. The wettability of the samples was determined by collecting images on a First Ten Angstroms FTA135 Contact Angle Analyzer. 10 μL of DI water was dropped onto the samples and images were collected on multiple spots of each sample. Images were processed using ImageJ contact angle plugin to determine water contact angle. Elemental composition of the prepared samples was investigated using X-ray photoelectron spectroscopy (XPS). Measurements were performed on a Thermo Scientific ESCALAB 250 spectrometer using a monochromated Al Kα X-ray source (150 W, 20 eV pass energy, 500 μm spot size). Peak fitting was done using ThermoScientific Avantage 4.75 software. A smart background subtraction was used for analysis and spectra were referenced to the C 1s hydrocarbon peak at 284.8 eV. Elemental ratios reported in this manuscript are the average of multiple spots measured across the same sample.

Results and Discussion

Preparation of hydrophobic coating and effect of UV photo-annealing

In this work, aluminum oxide coated cotton fabrics were fabricated via the solution deposition technique from f-Al_{13} cluster and compared to $Al(NO_3)_3$ precursor solutions. These coatings were photo-annealed with ultraviolet light to form the final hydrophobic Al_2O_3 coating.

In order for the solution processed aluminum precursors to form Al_2O_3, external energy is required to evaporate any residual solvent, decompose the nitrate counterions, and form Al-O-Al bonds. This is traditionally done through thermal post-processing at temperatures up to 500 °C. However, by leveraging the susceptibility of nitrate counterions to decompose under deep ultraviolet light, the need for external thermal energy can be circumvented and a low temperature approach can be achieved. By irradiating the coated fabrics with UV light at 253.7 and 183.9 nm, nitrate photolysis occurs (eq 4.1), producing an oxygen radical that reacts with water to form hydroxyl species (eq 4. 2), initiating the condensation of the final oxide.[18,19]

$$NO_3^- \xrightarrow{hv} {}^{\cdot}NO_2 + O^{\cdot -} \qquad (4.1)$$

$$O^{\cdot -} + H_2O \leftrightharpoons O \cdot H + OH^- \qquad (4.2)$$

Since both the f-Al_{13} cluster and $Al(NO_3)_3 \cdot 9H_2O$ absorb in the DUV range (Figure 4.1), the photo-annealing process can be leveraged to produce Al_2O_3 coatings. However, as demonstrated by Kim et. al., additional thermal energy is required to form the final oxide as UV alone is not sufficient to remove all residual solvent and counterions.[14,15]

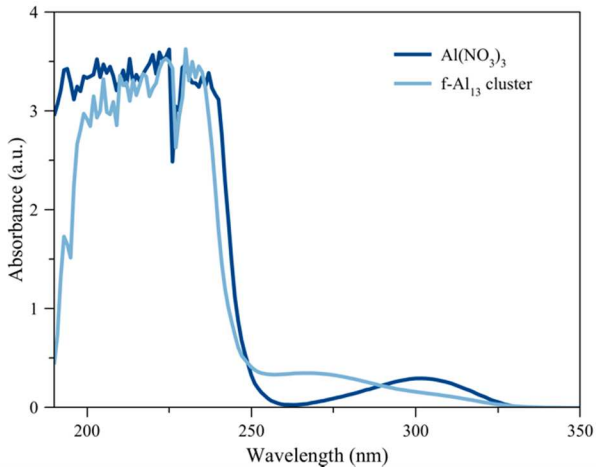

Figure 4.1 UV absorbance spectra of $Al(NO_3)_3 \cdot 9H_2O$ and f-Al_{13} cluster in nanopure H_2O.

Coincidentally, Jo et. al. demonstrated the use of a high powered mercury lamp (25-28 mW cm^{-2}) can generate radiant heat from the lamp up to 160 °C and form dense Al_2O_3 without the need for any further thermal annealing after exposure to UV, allowing for a one-step annealing process.

It is important to note that for the research presented in this manuscript, coatings were annealed with a lower powered mercury lamp (7-8 mW cm^{-2}) that could only generate radiant temperatures up to 30 °C. To compensate for this, additional thermal energy (hotplate = 120 °C) was utilized to further reduces the nitrogen content, densify the coatings, and produce higher water contact angles. It can be assumed that this process can be significantly optimized through the use of a higher powered lamp that generates heat. Therefore, when considering the potential for scaling up this process, the use of external

thermal energy may not be necessary as a higher powered lamp would alleviate the need for extra external heating.

Wettability of coated cotton fabrics

In order to assess the wettability of the prepared coatings, the water contact angle (WCA) of treated and untreated samples was collected and shown in Table 4.1. Figure 4.2 shows the images of samples with a 10 μL DI water droplet. The untreated native cotton samples immediately absorb water making it difficult to determine the contact angle. However, after coating the cotton with the precursor solutions, and photo-annealing, the hydrophobicity is greatly increased. The contact angle results suggest that both $Al(NO_3)_3$ and Al_{13} produce water repellent films with the f-Al_{13} cluster outperforming the $Al(NO_3)_3$. This is likely due to the precondensed aluminum-oxygen network in the f-Al_{13} cluster that more readily densifies to form the final oxide layer under these mild annealing conditions. These results show that hydrophobic coatings can be produced through photo-annealing of these aluminum precursors with no need for external thermal energy. With the radiant heat generated from the UV lamp increasing processing temperatures to only 30 °C, this is one of the lowest processing temperatures we have discovered for generating hydrophobic coatings on textiles (WCA ~120 °). However, adding thermal processing temperatures of 120 °C to the treated textiles does result in an increased WCA of 140.2 °. This increase in the contact angle can be attributed to the further evaporation of any remaining liquid solvent and removal of residual nitrate groups. Since any scale up of this process would likely use a higher powered lamp, it is likely that denser Al_2O_3 coatings would be produced, leading to these even higher water contact angles.

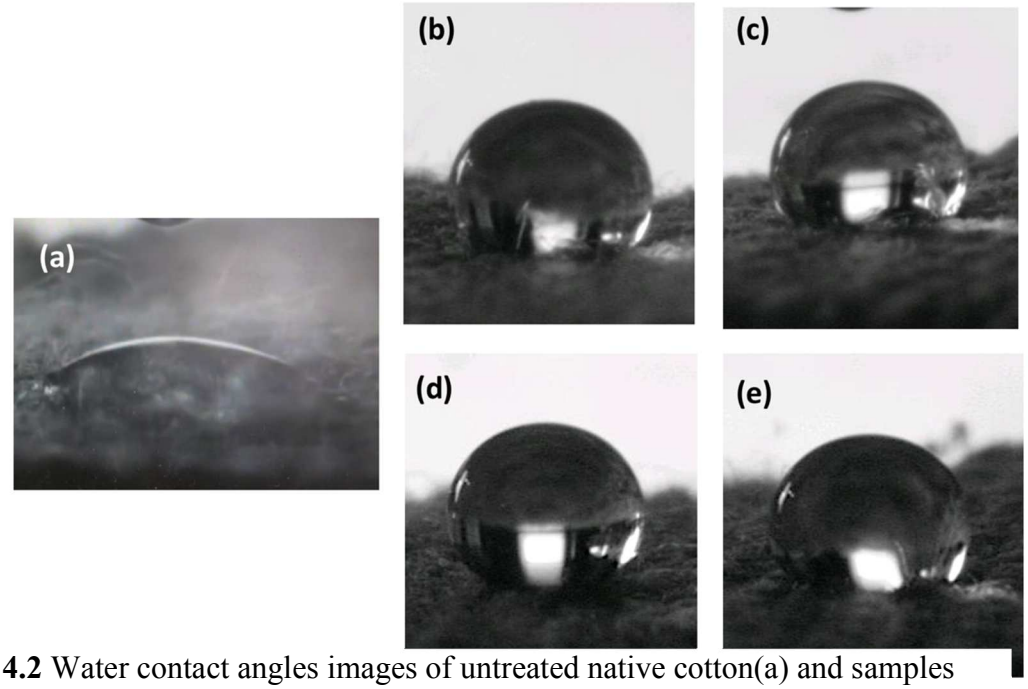

Figure 4.2 Water contact angles images of untreated native cotton(a) and samples treated with Al_{13}-UV (b), $Al(NO_3)_3$ – UV (c), Al_{13} – UV/Thermal (d), and $Al(NO_3)_3$ – UV/Thermal (e)

Table 4.1 Water contact angle measurements of native and Al_2O_3 coated cotton samples

Sample	WCA (°)
Native Cotton	< 10
Al_{13} – UV	122.3
$Al(NO_3)_3$ – UV	118.1
Al_{13} – UV/Thermal	140.2
$Al(NO_3)_3$ – UV/Thermal	127.2

Morphology of coated cotton

To ensure that Al_2O_3 was present on the surface of the textiles, elemental mapping via SEM-EDX was carried out. Figure 4.3 shows an example of the elemental mapping of carbon, oxygen, and aluminum for an Al_{13} sample that was UV and thermally annealed. The location of the aluminum on the fibers overlapped with oxygen, strongly indicates the presence of alumina on the surface.

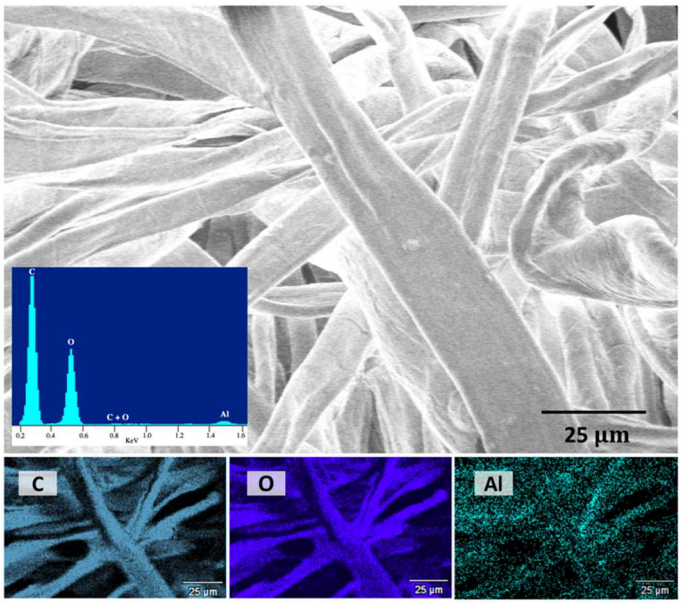

Figure 4.3 EDX elemental mapping of carbon, aluminum, and oxygen on f-Al_{13} sample UV and photo-annealed.

One unique aspect of the solution deposition process is the ability to uniformly coat the substrates using a variety of solution deposition techniques such as spray coating, drip coating, drop coating, or spin coating. These methods allow for relatively low concentrated solutions to be deposited and fully immerse the substrate in the precursor solution with little to no waste. Additionally, the precursor solution concentration can be optimized to

control the overall coating thickness and prevent cracking and sintering of the coatings.[20] This is further demonstrated in Figure 4.4. Figure 4.4a shows an SEM image of the native cotton and the inherent striations of the cellulose fibers can be discerned. In Figure 4.4b, the fiber is coated with Al_2O_3 from the f-Al_{13} cluster solution and the striations can still be discerned, indicating a relatively thin and uniform Al_2O_3 coating. However, the fibers coated from the $Al(NO_3)_3$ precursor solution in Figure 4.4c appear significantly rougher, which is likely due the increased number of nitrate counterions that have to burn off which leads to a rougher coating with more morphological defects.

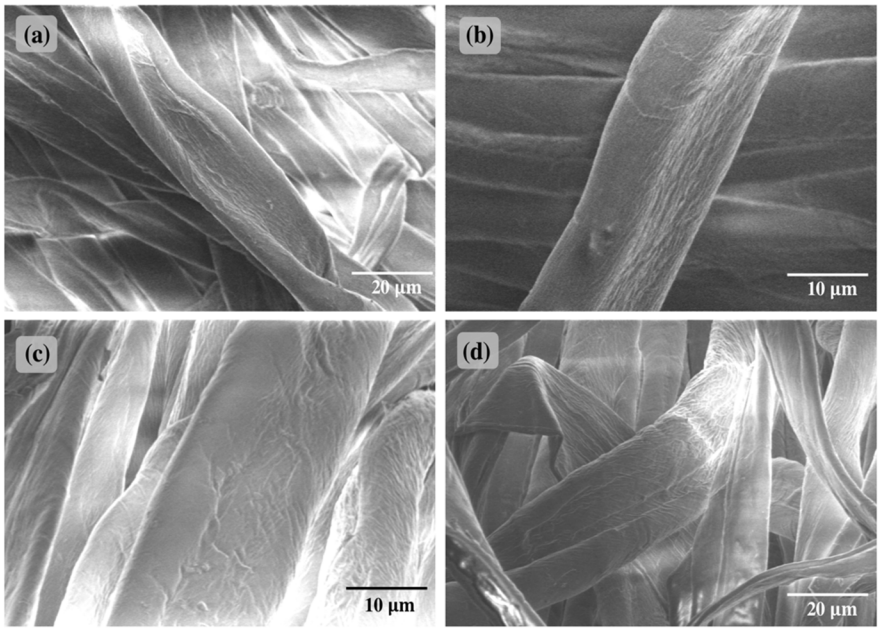

Figure 4.4 SEM images of native cotton (a), and sample Al_{13}-UV (b), $Al(NO_3)_3$-UV (c) , and Al_{13}-UV/thermal (d).

To further probe the morphology of these coatings, the surface roughness of the prepared samples was explored through atomic force microscopy (AFM). Figure 4.5 shows AFM scans of individual fibers on the native cotton, Al_{13} -UV, and $Al(NO_3)_3$-UV samples. In all 3 samples, a textured surface can be elucidated, and the resulting RMS roughness (R_{rms}) and average roughness (R_A) are presented in Table 4.2. Interestingly, coating the

cotton in Al_2O_3 from the f-Al_{13} only slightly increases the surface roughness of the cotton, whereas there is a drastic increase in the RMS roughness in the cotton coated from $Al(NO_3)_3$. This roughness discrepancy can be likely attributed to the increased nitrate to aluminum ratio in $Al(NO_3)_3$ (3:1 ratio) compared to that of the f-Al_{13} (1.15:1). In order to form the final film, these nitrate groups need to decompose and therefore the additional nitrate groups present in the $Al(NO_3)_3$ coatings lead to a more porous and rougher coating.

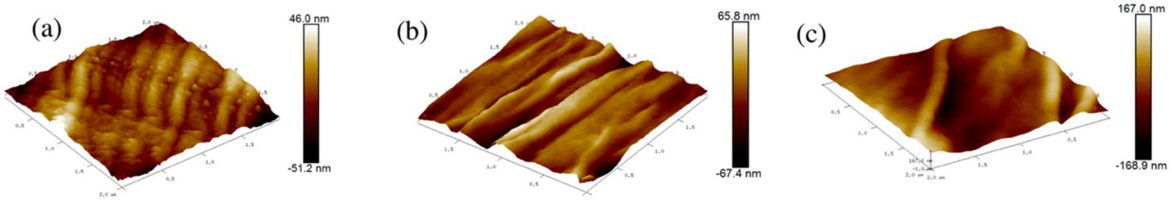

Figure 4.5 2 μm^2 AFM scans of native cotton (a), sample Al_{13}-UV (b) and sample $Al(NO_3)_3$ – UV (c).

Table 4.2 Surface roughness of native and Al_2O_3 coated cotton.

Sample	R_{RMS} (nm)	R_A (nm)
Native Cotton	12.4	9.43
Al_{13} – UV	18.7	14.6
$Al(NO_3)_3$ – UV	42.5	29.5

Elemental analysis of prepared samples

It is important to address that one of the major advantages of this synthesis is that the presented precursor solution contains no organic additives or ligands. As a result, the final coating is composed of pure Al_2O_3 plus any elemental nitrogen that has not fully decomposed from residual nitrate counterions. Table 4.3 shows the elemental analysis of

native cotton and the four prepared Al_2O_3 coatings. There are a couple of important conclusions that can be elucidated from this data. First, it is clear that cotton coated with the f-Al_{13} cluster contains substantially less nitrogen than that of the analogous $Al(NO_3)_3$ coatings. This is expected due to the precondensed nature of the cluster, coupled with a higher aluminum to nitrate ratio (13:15) that enables coatings to more readily condense.[12] Second, as expected, the addition of heat to this process also contributes to reduced nitrogen content in the coatings. Based on previous literature, it is not unreasonable to suspect that an optimized process with a higher powered lamp will remove all of the nitrate and further enhance the contact angle.

Table 4.3 Elemental analysis of native and Al_2O_3 coated cotton samples

Sample	Chemical composition (at.%)					
	C			Al	O	N
	C-H	C-OH	C-O-C			
Native Cotton	38.84	27.35	6.63	-	27.17	-
Al_{13} – UV	36.41	22.1	5.55	3.51	30.02	2.41
$Al(NO_3)_3$ – UV	45.04	15.69	7.15	2.12	25.84	4.15
Al_{13} – UV/Thermal	36.62	22.79	6.59	2.16	29.62	2.22

Scalability of presented hydrophobic coatings

Perhaps the greatest advantage of the presented process is the ability and ease of scaling up. The f-Al_{13} precursor uses inexpensive starting materials, requires minimal synthetic steps, and can be fabricated in large quantities. The precursor solutions require minimal amounts of precursor (10 mM f-Al_{13}) dissolved in an acetone/water mixture that is environmentally benign. This solution can be deposited onto a variety of textiles via a multitude of scalable deposition techniques such as spray casting, dip coating, drip coating, spin coating, and ink jet printing. The UV photo-annealing step requires minimal energy and scalability is only limited by the size/number of lamps used. As a representative example to showcase the potential scalability of our process, a 400 cm^2 piece of cotton fabric was spray-coated with the f-Al_{13} precursor solution using an airbrush with N_2 flow. The sample was then subjected to 2 hours of ultraviolet light and the resulting hydrophobicity is presented in Figure 4.6.

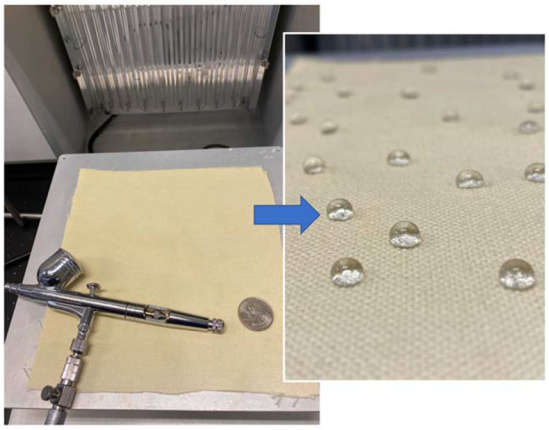

Figure 4.6 Image showing the scalability of presented process. Image on left shows spray coater used to coat 400 cm^2 of cotton to produce hydrophobic cotton (right). Quarter in left image for scale.

Conclusions

This research presents the first scalable approach to forming Al_2O_3 coatings on textiles. Traditionally this has been accomplished with high energy techniques such as ALD or sol-gel processes that require multi-step processing and contain substantial organic additives. In this work, hydrophobic cotton can be achieved at ultra-low processing temperatures (30 °C) by utilizing deep ultraviolet light to photo-anneal the coatings. We demonstrate the viability of the f-Al_{13} cluster, its advantages over $Al(NO_3)_3$, and the benefits of using solution deposition to produce hydrophobic Al_2O_3 coatings without the use of any organic additives or ligands.

Lastly, we display the scalability of this process by spray coating a 400 cm^2 piece of cotton with the f-Al_{13} precursor solution, photo-annealing it for 2 hours at 30 °C, and prove strong resulting hydrophobicity. These results show that this process can be easily scaled up and that photo-annealed Al_2O_3 hydrophobic coatings could be considered as a greener alternative to PFASs.

Bridge to Chapter V

In addition to demonstrating the feasibility of solution deposited Al_2O_3 coatings, Chapter IV showcased some relevant morphological characterization techniques, such as SEM, EDX, and AFM. In Chapter V, we aim to build upon these nanomaterial characterization techniques, with efforts aimed at characterizing the topology of vertically aligned carbon nanotubes used as retinal implant electrodes.

CHAPTER V

CHARACTERIZATION OF VERTICALLY ALIGNED CARBON NANOTUBE FILMS FOR USE AS RETINAL IMPLANTS INTERFACE

Introduction

Biological implants that restore general sensory function to the impaired is an incredible example of scientific and societal advancement. Whether it be the use of cochlear implants to restore hearing in the deaf, prosthetic limbs controlled through neural impulses, or a pacemaker to help control heart arrythmias[1-3], the impact of these implants is life changing for the patients. Scientists, doctors, and engineers have worked tirelessly to not only develop these implants, but to continually optimize their functionality. While an incredible amount of progress has been made in partially restoring these functions, there remains substantial room for improvement.

One area of biological implants is retinal implants to restore blindness. Retinal implants provide restored vision in patients who suffer from age-related macular degeneration (AMD) and retinitis pigmentosa (RP). AMD and RP are both degenerative eye diseases that cause the deterioration of key photoreceptors in the eye that translate images to the brain.[4,5] However, since the retina still remains intact in these diseases, a device can be implanted in the eye to electrically stimulate the healthy retinal neurons as shown in Figure 5.1. Based on the design of the implant and electrical stimulation method, patients can effectively transmit images from their surroundings to return some degree of vision.

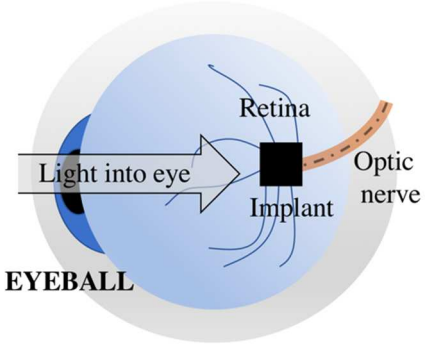

Figure 5.1 Visual representation of retinal implant.

Zrenner et. al. has shown the effectiveness of subretinal implants comprised of titanium nitride (TiN) electrodes.[6] In their clinical trials, they were able to show statistically significant vision restoration in six patients with a maximum visual acuity of 20/1000.[7] Recent experimentation has optimized this process to achieve visual acuities of 20/546, but these results were not fully reproducible amongst the tested patients.[8,9] Additional epiretinal implants, such as Second Sight's Argus II, are comprised of platinum electrodes has also restored partial vision comparable visual acuities of 20/1000.[10] While the ability to restore any vision in patients suffering from AMD or RP is truly remarkable, the resulting visual acuity has significant room for improvement.

The main obstacle in reaching optimal implant performance is the interfacial inefficiencies of the electrodes stimulating the retinal neurons. Less than 10% of the interconnects on the electrode are believed to successfully stimulate the retinal neurons.[11] However, if implants can be optimized to have 100% of interconnects stimulating neurons, then partial vision can be restored up to 20/80 visual acuity (Figure 5.2).

The Richard Taylor group at the University of Oregon is on the forefront of retinal implant research through investigating exiting and novel solutions to improve neuronal

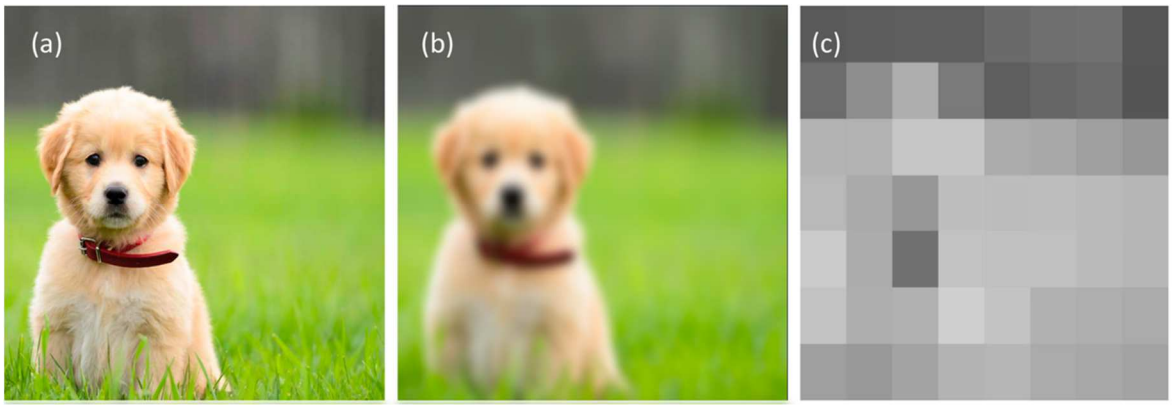

Figure 5.2. (a) Image observed with perfect 20/20 vision. (b) Equivalent image expected with optimized implants displaying 20/80 vision (25%). (c) Simulated image expected with current retinal implants that display 20/1000 vision (2 %).

stimulation. The Taylor group has spent significant time investigating the viability of retinal implants that are geometrically inspired by fractals. Fractals are geometric patterns that self-repeat at increasingly smaller size scales. A common pattern in nature, fractal patterns are found in the branching structure of trees, Romanesco broccoli, snowflakes, and much more. Fractals can also be mathematically constructed through creating unlimited branching iterations from a starting design as shown in Figure 5.3.

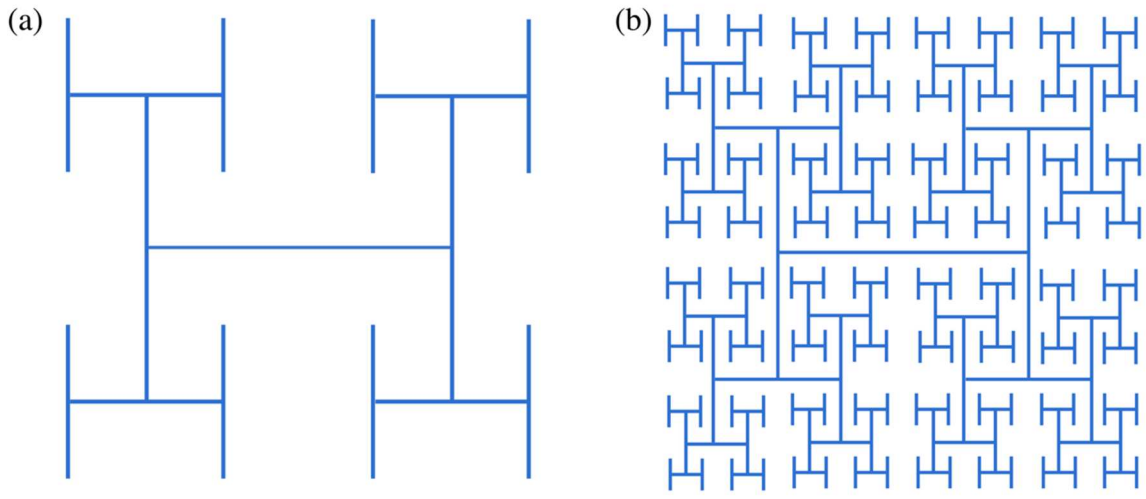

Figure 5.3 Mathematical fractal pattern of H-tree seed design with 1 iteration (a) and 3 iterations (b).

Fractally designed electrodes could be a route for advancing over retinal implants past traditional designs since neurons themselves exhibit fractal branching behavior.[12] These benefits include maximized capacitance, optimized morphology, a supportive environment for glial cells in the negative space, transmission wavelength tunability, and mechanical flexibility that allows electrode to form to the natural curvature of the eye.[13]

In addition to selecting the preferred geometry, it is also critical to select an electrode material that will support peak implant performance. With this in mind, the Taylor group selected multiwalled vertically aligned carbon nanotubes (VACNT) as the electrode. These VACNT films are conductive, biocompatible, flexible, and have been shown to be an effective material for artificial bio implants.[14,15] Additionally, the fabrication method allows photolithography to be utilized to produce CNT films in any desired pattern as shown in Figure 5.4.

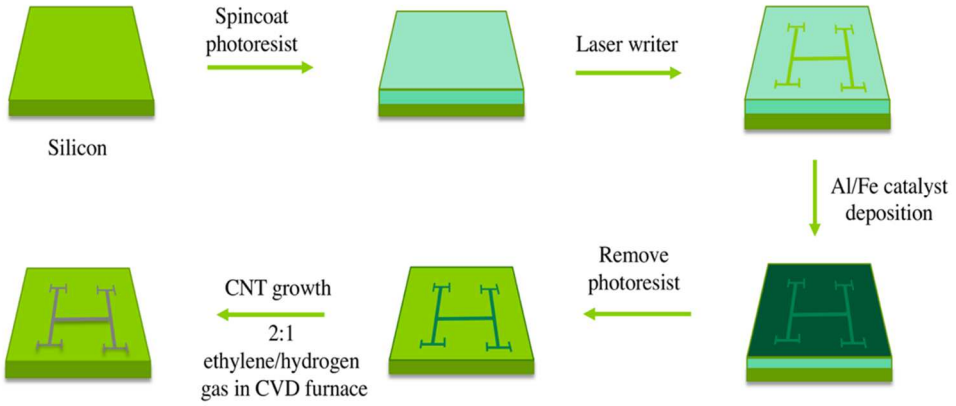

Figure 5.4 Fabrication process of VACNT film with H-tree design.

Research in the Taylor group has shown that fractal patterned VACNT films allow for glial cell proliferation and neuronal outgrowth to be maximized. These results have shown a strong preference for glial cells to proliferate on the silicon substrate, while the neurons prefer to grow on the surface of the CNTs.[12] In addition to the fractal design, the

surface of the CNT films has shown to exhibit strong neural adhesion. This is due to the CNT's forest-like morphology that closely mimics the extracellular matrix of the neurons. The intertwined branched nature of CNT films and neurons preference to grow along the edges of the films are shown in Figure 5.5a and 5.5b, respectively.

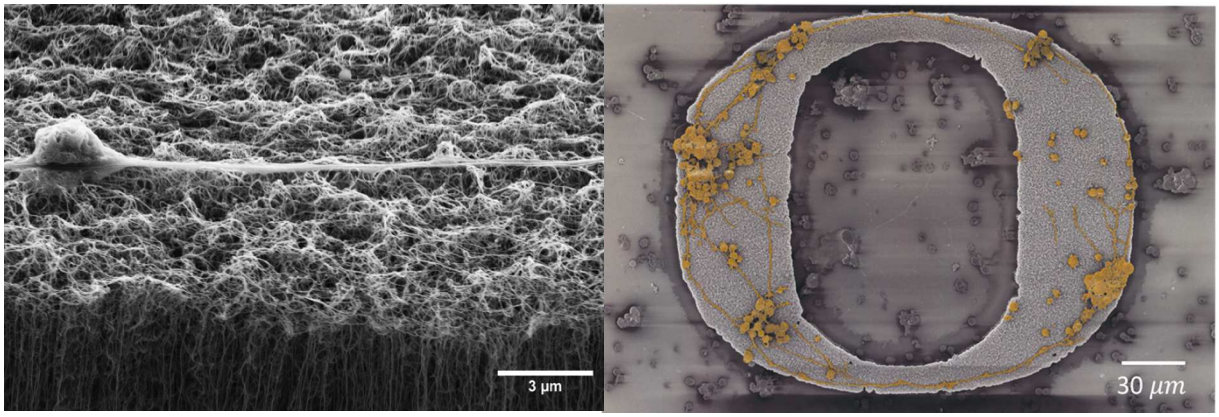

Figure 5.5 (a) SEM image showing forest like morphology closely mimicking the extracellular matrix of the neuron. (b) SEM image of CNT showing neurons (in yellow) strong preference for growing along the edges.

The goal of this project was to characterize the surface morphology of these films, a necessary step in determining how neurons respond to differences in surface roughness and giving insight to their preference for the edges of the CNT surface. It is hypothesized that neurons prefer the edges due to proximity of the glial cells on the silicon substrate. It is also possible that due to the natural curvature of the edge, the neurons can achieve maximum outgrowth as shown in.[16] In order to test or confirm these hypotheses, the surface morphology of these films needed to be characterized.

Since the use of VACNT's as electrodes was a relatively new field, there was no determined or published approach for characterizing the surface morphology of these films. This is due to some of the physical characteristics that these VACNT films exhibit that will

be further discussed in this manuscript. Therefore, due the many advantages of VACNT's and the opportunity for them to play a large role in the next generation of retinal implants, it was vastly important to determine characterization techniques for this material as it could help optimize the electrodes and improve visual acuity in the next generation of retinal implants.

Ineffective characterization attempts

Atomic force microscopy (AFM)

The first approach taken in this investigation was to use atomic force microscopy (AFM), a commonly used technique for characterizing surface roughness and morphology of thin films. In this technique, a microscopic probe placed on the end of a cantilever is rapidly tapped across the surface of the sample. Changes in surface texture of a sample can be detected and 3-dimensional surfaces and roughness parameters can be determined. Performing AFM on these CNT films proved difficult due to their natural "mechanical sponginess" of the CNTs, a property stemming from their medium density and high aspect ratio. This resulted in the inability of the CNT's to withstand force from the AFM probe which produced unresolved AFM images, damaged the film, and did not provide useful

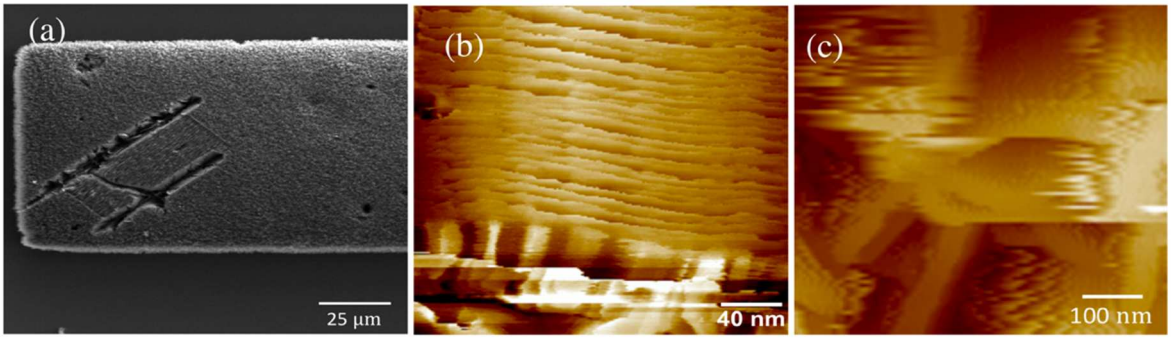

Figure 5.6 (a) SEM image showing destruction of CNT film due to AFM probe. (b & c) AFM images showing unresolved images, streaking, and morphology unrepresentative of CNT forest-like surface.

surface morphology information (Figure 5.6). Many attempts were made to produce accurate results, but surface mappings proved to not be representative of CNT surface.

Optical profilometry

After unsuccessful attempts to characterize the surface via AFM, optical profilometry was utilized on the CNT films. Optical profilometry is a useful technique for creating 3-dimensional (3D) renderings of surface morphologies through use of an optical microscope. In this technique, light is reflected off the sample and compared to light reflected off a reference mirror. Unfortunately, this proved problematic as vertically aligned carbon nanotubes have been shown to be one of the darkest absorbing materials and can absorb light almost perfectly across a wide spectral range (0.2-200 μm).[17] This caused the CNT forest to absorb the majority of light from the optical profilometer and resulted in the 3-dimensional surface in Figure 5.7 .

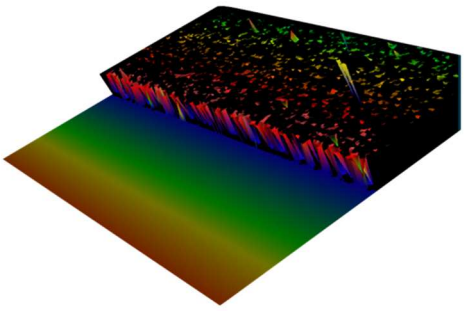

Figure 5.7 3-dimensional rendering produced from optical profilometry. Black regions display where all incident light is absorbed by CNT surface.

Effective characterization attempts

3D SEM stereo reconstruction

Due to the inability for AFM and optical profilometry to characterize the morphology of the CNT films, 3-D scanning electron microscopy (SEM) stereo

reconstruction was investigated. SEM stereo reconstruction is a novel technique used to create 3-D surface renderings constructed from two SEM images taken at different angles.[18] Since this technique does not physically probe the surface of the CNT films, it seemed like a viable option to characterize the morphology of these films in a non-destructive manner.

The renderings in this research were produced using Alicona MeX software. To construct accurate 3D renderings using this software, the following parameters have to be optimized:

- eucentric tilt angle
- projection distance
- sampling distance
- global offset

The eucentric tilt angle refers to the difference in tilt angle between the two SEM images where the tilting axis for the SEM stage is located in the middle of the sample as shown in figure 5.8. The SEM being used for this research, FEI Helios 600i, had eucentric

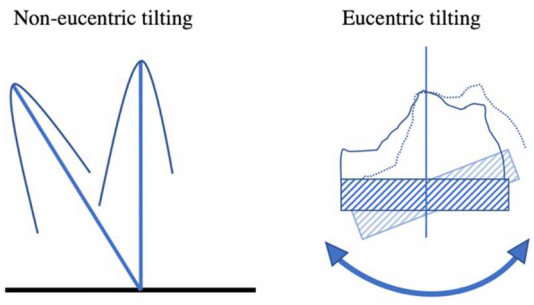

Figure 5.8 Examples of non-eucentric tilting and eucentric tilting where tilting axis is in the middle of the sample.

tilting ability, so as long as clear images with high contrast are taken, 3D renderings could be produced.

Projection distance refers to the distance between the sample surface and the crossover point of the ion beam in the SEM. This is a combination of the working distance (wd) which is the distance between where the beam comes out and the surface of the sample, and the epsilon value (ε), which is the distance between the crossover point of the ion beam and where the beam actually comes out as shown in Figure 5.9.

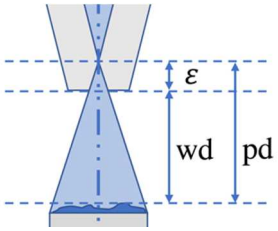

Figure 5.9 Diagram showing projection distance (pd) as combination of working distance (wd) and ε.

The sampling distance informs the software of the actual distance between pixels in the SEM image being sampled. For instance, an SEM image that is 1800 pixels wide that sampled a width of 180 μm would have a sampling distance of 0.1 μm per pixel. This information is crucial for gathering accurate height and quantitative morphological data.

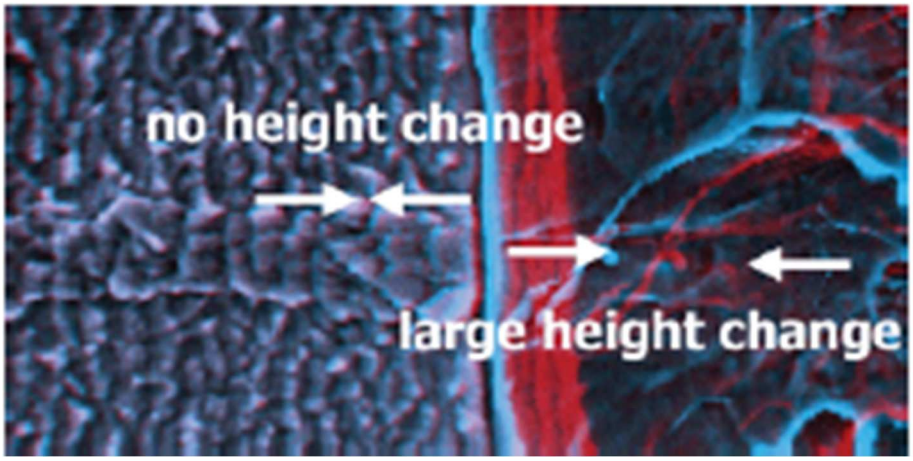

Figure 5.10 Two overlaid SEM images where area with high overlap indicates no height change and areas with distance in between similar features indicate large height change.

Lastly, the global offset refers to the distance between matching surface features when the two SEM images are overlaid as shown in Figure 5.10.

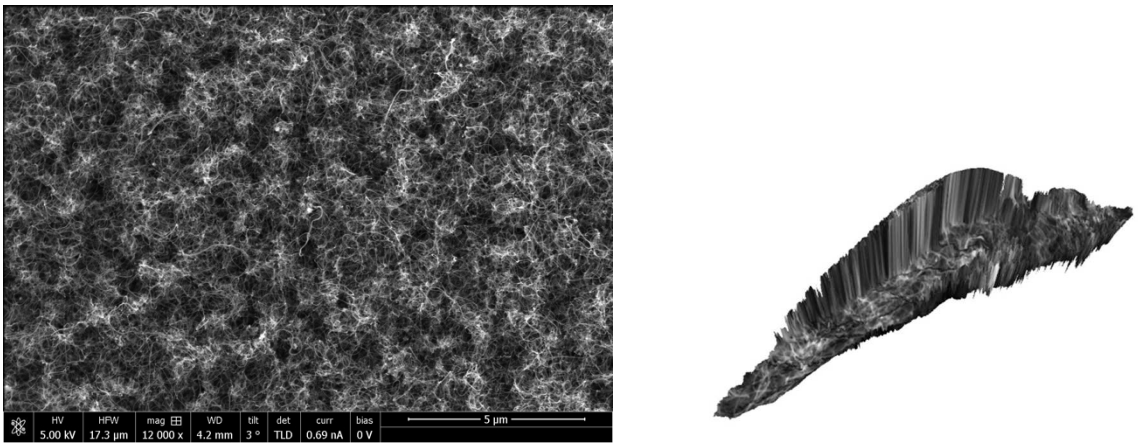

Figure 5.11 (Left) SEM image used to make 3-D renderings. (Right) Unsuccessful 3-D rendering made from SEM image on the left plus similar image eucentrically tilted 5°. Rendering is clearly not representative of CNT forest. Rendering completed using Alicona MeX metrology software.

Initial use of the Alicona MeX software proved difficult as early experimentation with the software lead to unsuccessful renderings that did not represent the surface of the CNT films (Figure 5.11). It was determined that the large variability was directly influenced by the ε value input parameter. Efforts made to determine this value involved communication with SEM operators, contacting the SEM instrument manufacturer (FEI), and speaking with representatives from Alicona MeX. Through trial and error, the ε value was determined to be approximately 10 mm. This value worked well in conjunction with accurate sampling distances and generated promising renderings as shown in Figure 5.12.

The rendering in Figure 5.12b seemed promising because it displayed the edges of the film which were of particular interest due to the neurons strong preference to adhere to the edges. In efforts to expose the edges of these carbon nanotube, new SEM images were

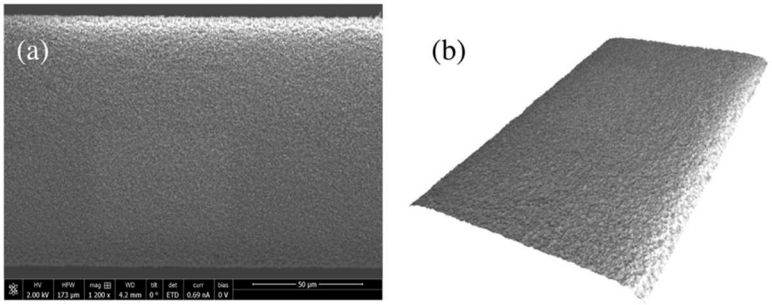

Figure 5.12 (a) SEM image used to create 3-D rendering. (b) Promising rendering created from SEM image in (a) and similar SEM image eucentrically tilted at 5 °. Right side of rendering displays curved edges, which were of interest.

taken at eucentric tilt angles from 0° to 37° and displayed the corner of a CNT row (Figure 5.13). Experimenting with these new SEM images eventually lead to a successful rendering (Figure 5.13) that clearly showed the sides of the CNT row and the complex morphology of the top.

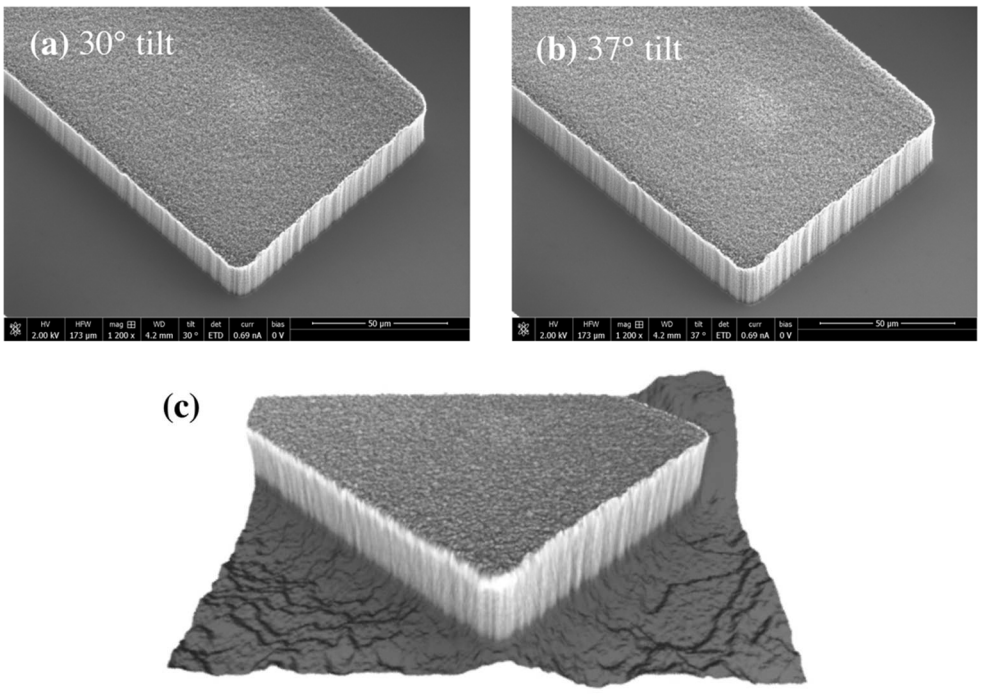

Figure 5.13 SEM images of CNT row eucentrically tilted at 30° (a) and 37° (b). (C) 3D reconstruction of CNT row from SEM images in (a) and (b).

Once the renderings were completed, quantitative morphological data could be collected. Data for average heights, maximum and minimum peak to valley heights, and RMS roughness were obtained using the Alicona Mex software. Figure 5.14 shows the profile analysis of the red path line manually drawn on the surface of the image. Once the path length has been analyzed, quantitative data was collected as shown in Table 5.1.

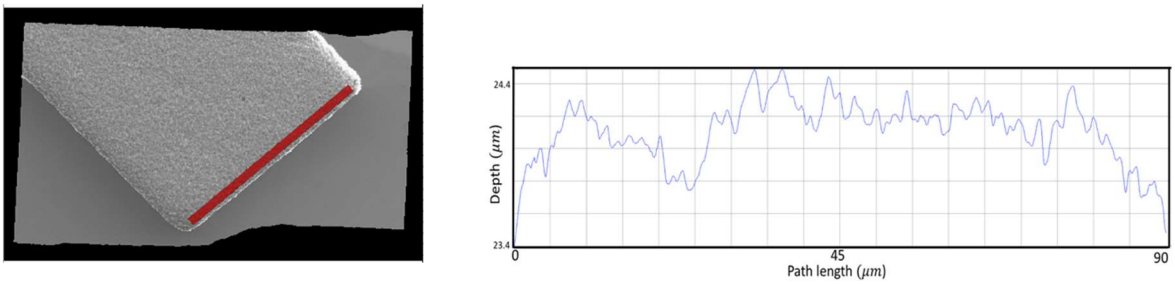

Figure 5.14 Results from surface profile analysis. Right image displays the height profile of the surface of the CNT film along the red line on the left image.

Table 5.1. Morphological data obtained from profile in Figure 5.14

Average Height	RMS roughness	Maximum peak to valley length
23.72 µm	166.04 nm	1.09 µm

Reproducibility of 3D reconstructions

Since establishing the imaging parameters, additional renderings of the surface of these films have been completed. However, since there is no additional technique that can be used to corroborate these results, the accuracy of the renderings has to be confirmed using the tools available in the software as well as any information available in the original SEM images. Distance measurements of the CNT rows in SEM images show a width of roughly 98 µm and a height of approximately 22 µm as shown in Figure 5.15.

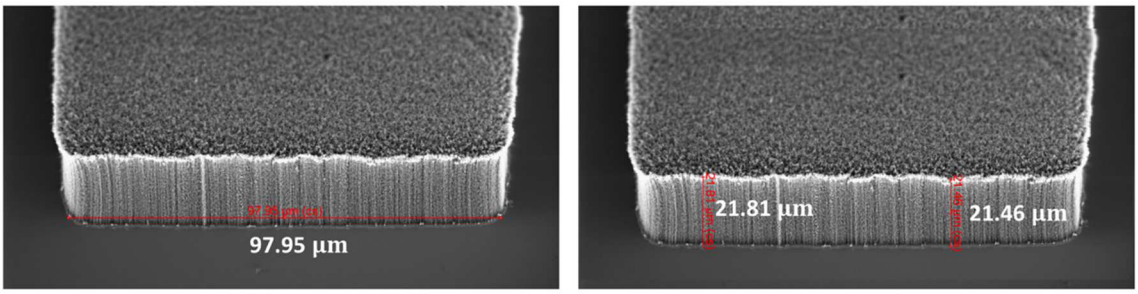

Figure 5.15 SEM images showing the width and height of CNT rows.

Using the data analysis tools in the 3D reconstruction software, these height and width measurements have been confirmed for the produced renderings as confirmed in Figure 5.16

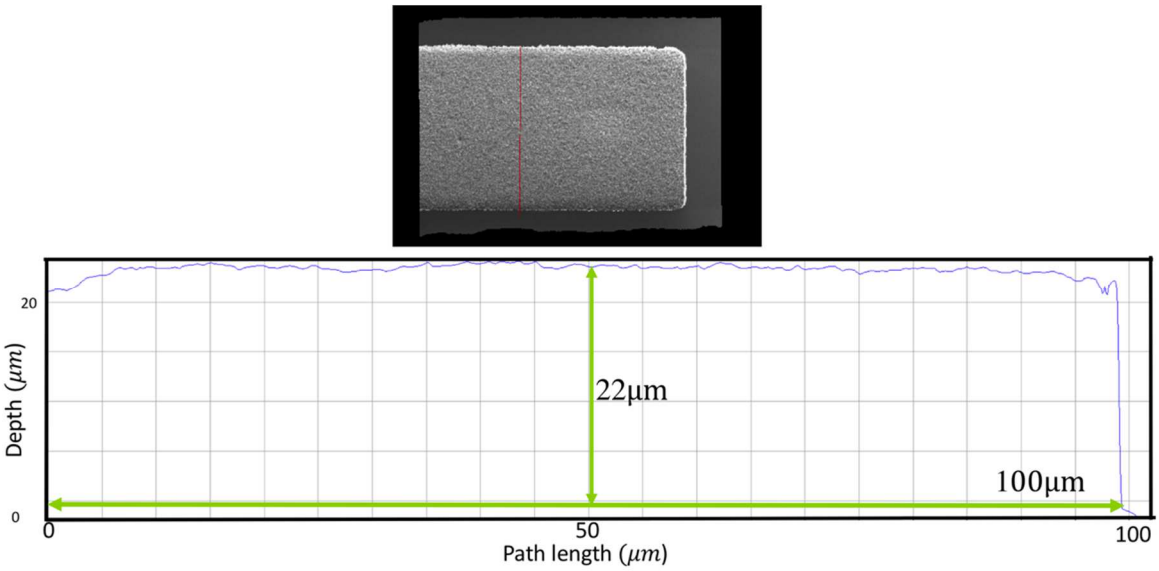

Figure 5.16 Path length profile of red line on above image. Profile analysis displays a height of approximately 22 microns and a width of approximately 100 microns.

Although the height and width of the CNT rows was corroborated by the 3D SEM profile analysis, there is still considerable room for error, especially when mapping out the morphology of the incredibly complex surface of the CNT's. In order to feel confident about the renderings, it was important to analyze the reproducibility of these renderings

and determine any known errors. Previous reports have confirmed that 3D SEM reconstruction exhibits a relative uncertainty of 5% and 4% for rotation and tilt respectively.[19]

To assess reproducibility, multiple renderings were collected, and the resulting surface morphology analyzed. In order to ensure that the same area of the sample was being analyzed, a particular region of a CNT row that contained a naturally occurring divot was used (Figure 5.17). By repeatedly analyzing the width and depth of this divot in multiple renderings, the reproducibility and standard deviation in the profile analysis could be determined.

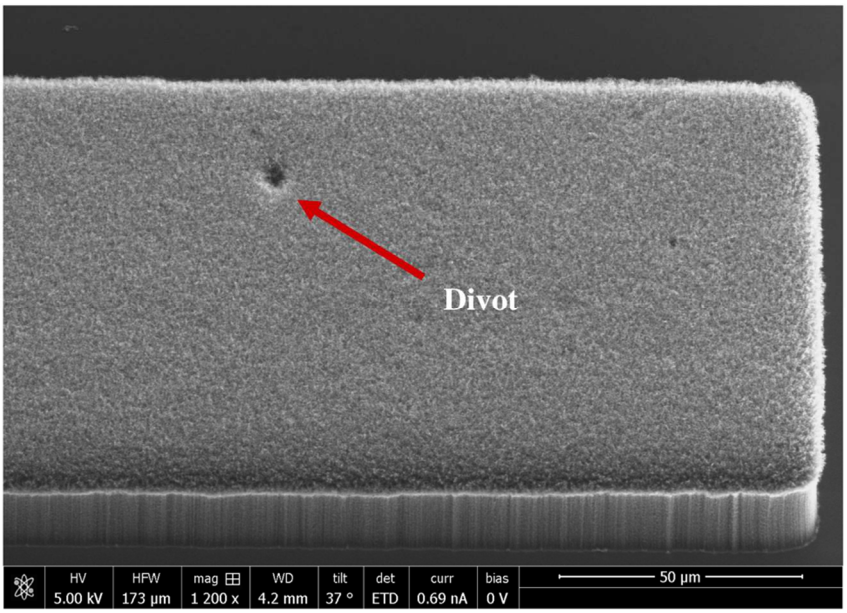

Figure 5.17 SEM image of CNT row showing divot used for profile analysis.

Figure 5.18 shows one profile analysis of the CNT row with the divot and the resulting width and depth. This process was repeated 8 times and the widths and depths of the divot were recorded. The results indicate that the divot had an average width of 6.12 ± 0.55µm and average depth of 2.06 ± 0.24 µm. These results showed an 8.9% and 11.6%

error in the width measurement and depth measurement, respectively. This variance in the measurements was relatively higher than the 4% reported errors from Carli et. al.

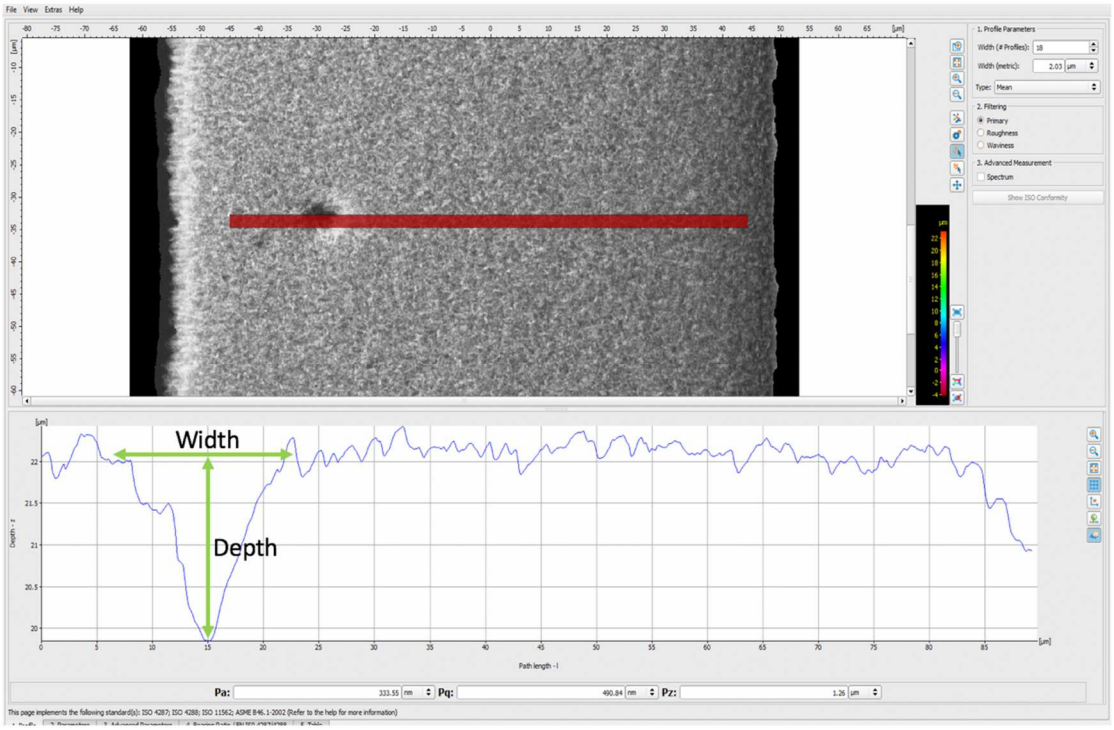

Figure 5.18 Profile analysis of 3D rendering of CNT row with divot.

These results suggest that mapping out CNT films using 3D SEM stereo reconstructions is somewhat complex. This technique is fairly useful at mapping out large-scale features in films and explains the accurate representation of the overall height and width of the CNT row in the rendering. However, since the overall morphology of these CNT films is comprised of strands of carbon nanotubes that are 3-7nm in diameter, it proved difficult to get accurate representation of the smaller features on the surface.

Conclusions

In an effort to better understand the underlying mechanisms of neural adhesion on vertically aligned carbon nanotube films, a variety of instrumental techniques were utilized. AFM was ineffective due to the mechanical sponginess of the CNT rows which resulted in the AFM tip damaging the films. Optical profilometry also proved unhelpful as the CNT's absorbed the majority of the light, resulting in the total loss of morphological information. 3D SEM stereo reconstruction proved the most promising and was further investigated.

After troubleshooting to produce accurate renderings, 3D SEM stereo reconstruction was used to produce 3D renderings of carbon nanotube films. This technique proved effective at mapping out the overall structure of the CNT rows. Unfortunately, due to the complex nature of the CNT rows, 3D SEM stereo reconstruction did not provide reproducible surface morphology results. However, it is possible that advanced 3D SEM rendering software that could resolve the complex nature of the CNT rows and future work should involve using advanced software with less uncertainty in the results.

Bridge to Chapter VI

Chapter VI wraps up this dissertation by reiterating the benefits of solution processing, demonstrating the scalability and sustainability, as well as suggesting how it can be incorporated into the next generation of metal oxide films .

CHAPTER VI

CONCLUSIONS

Concluding Remarks

Modern society continues to be defined by technological advances that have progressed the world into the digital age. While the benefits of these technological advances cannot be overstated, it is important we consider the environmental impact the production of electronic devices have had on the planet. Metal oxides are an essential component to modern microelectronics and their fabrication requires significant processing energy due to the high temperature and vacuum conditions required. Solution processing of metal oxides offers a greener alternative for the fabrication of metal oxide films, using lower processing temperatures, less toxic precursors, and environmentally benign solvents. Historically, it has been a challenge for solution processed films to achieve the performance of their CVD counterparts, but recent advances in the field have closed this gap, further enhancing the profile of solution processing. Thus, microelectronics and a variety of other industrial fields could greatly benefit from the economic, and sustainability x0benefits of solution processing.

This dissertation demonstrates the advantages of solution processed films from the perspective of scalability and sustainability. Chapter II demonstrated the viability of the novel CoAl cluster to produce high quality mixed metal oxide films. Chapter III explored the industrial viability of solution processed coatings. This work has already had an immediate impact on industry as MinTEQ International's Pyrogenics Group is currently in testing production of their new solution processed materials. The work presented in

Chapter V attempted to tackle a significant sustainability issue that is currently challenging the footwear and apparel industries. This chapter truly encompasses all of the benefits of solution processing, provide a water repellent coating process that is extremely scalable, requires ultra-low temperature processing, and is solution processed from environmentally friendly solutions. With the demonstrated industrial viability and sustainability, solution processing can provide an immediate environmental impact and should be seriously considered for fabrication of the next generation of metal oxide thin films and coatings.

REFERENCES CITED

CHAPTER I

[1] Fortunato, E.; Ginley, D.; Hosono, H.; Paine, D. C. Transparent Conducting Oxides for Photovoltaics. *MRS Bull.* **2007**, *32* (3), 242–247.

[2] Nguyen, T. T.; Patel, M.; Kim, J.-W.; Lee, W.; Kim, J. Functional TiO_2 Interlayer for All-Transparent Metal-Oxide Photovoltaics. *J. Alloy. Compd.* **2020**, *816*, 152602.

[3] Park, J. S.; Maeng, W. J.; Kim, H. S.; Park J. S. Review of recent developments in amorphous oxide semiconductor thin-film transistor devices. *Thin Solid Films*, **2012**, 520, 1679–1693.

[4] Trinh, H. D.; Chang, E. Y.; Wu, P. W.; Wong, Y. Y.; Chang, C. T.; Hsieh, Y. F.; Yu, C. C.; Nguyen, H. Q.; Lin, Y. C.; Lin, K. L.; Hudait, M. K. The Influences of Surface Treatment and Gas Annealing Conditions on the Inversion Behaviors of the Atomic-Layer-Deposition Al2O3/n-In0.53Ga0.47As Metal-Oxide-Semiconductor Capacitor. *Appl. Phys. Lett.* **2010**, *97* (4), 042903.

[5] Sun, Y.-F.; Liu, S.-B.; Meng, F.-L.; Liu, J.-Y.; Jin, Z.; Kong, L.-T.; Liu, J.-H. Metal Oxide Nanostructures and Their Gas Sensing Properties: A Review. *Sensors* **2012**, *12* (3), 2610–2631.

[6] Smith, R. D. L.; Prévot, M. S.; Fagan, R. D.; Zhang, Z.; Sedach, P. A.; Siu, M. K. J.; Trudel, S.; Berlinguette, C. P. Photochemical Route for Accessing Amorphous Metal Oxide Materials for Water Oxidation Catalysis. *Science* **2013**, *340* (6128), 60–63.

[7] Talic, B.; Molin, S.; Wiik, K.; Hendriksen, P. V.; Lein, H. L. Comparison of Iron and Copper Doped Manganese Cobalt Spinel Oxides as Protective Coatings for Solid Oxide Fuel Cell Interconnects. *J. Power Sources* **2017**, *372*, 145–156.

[8] Wang, Y.; Runnerstrom, E. L.; Milliron, D. J. Switchable Materials for Smart Windows. *Annu. Rev. Chem. Biomol. Eng.* **2016**, *7*, 283–304.

[9] Wei, Q.; Zheng, H.; Huang, Y. Direct Patterning ITO Transparent Conductive Coatings. *Sol. Energ. Mat. Sol. C.* **2001**, *68* (3), 383–390.

[10] Joo, S. Y.; Loka, C.; Jo, Y. W.; Reddyprakash, M.; Moon, S. W.; Choi, Y.; Lee, S. E.; Cho, G. S.; Lee, K.-S. ITO/SiO_2/ITO Structure on a Sapphire Substrate Using the Oxidation of Ultra-Thin Si Films as an Insulating Layer for One-Glass-Solution Capacitive Touch-Screen Panels. *Coatings* **2020**, *10* (2), 134.

[11] Wang, B.; Bates, J.B.; Hart, F.X.; Sales, B.C.; Zuhr, R.A.; Robertson, J.D. Characterization of Thin□Film Rechargeable Lithium Batteries with Lithium Cobalt Oxide Cathodes. *J. Electrochem. Soc.* **1996** 143 3203

[12] Park, J.-S.; Jeong, J. K.; Chung, H.-J.; Mo, Y.-G.; Kim, H. D. Electronic Transport Properties of Amorphous Indium-Gallium-Zinc Oxide Semiconductor upon Exposure to Water. *Appl. Phys. Lett.* **2008**, *92* (7), 072104.

[13] Prasanna, S. R. V. S.; Balaji, K.; Pandey, S.; Rana, S. Metal Oxide Based Nanomaterials and Their Polymer Nanocomposites. *Nanomaterials and Polymer Nanocomposites*; Elsevier, **2019**; 123–144.

[14] Yin, Z.; Huang, Y.; Bu, N.; Wang, X.; Xiong, Y. Inkjet printing for flexible electronics: Materials, processes and equipments. *Chinese Sci. Bull.* **2010** 55(30), 3383–3407.

[15] Anastas, P. T.; Warner, J. C. Green Chemistry: Theory and Practice; *Oxford University Press: New York*, **1998**; p 30.

[16] Trotochaud, L.; Ranney, J. K.; Williams, K. N.; Boettcher, S. W. Solution-Cast Metal Oxide Thin Film Electrocatalysts for Oxygen Evolution. *J. Am. Chem. Soc.* **2012**, *134* (41), 17253–17261.

[17] Kast, M. G.; Cochran, E. A.; Enman, L. J.; Mitchson, G.; Ditto, J.; Siefe, C.; Plassmeyer, P. N.; Greenaway, A. L.; Johnson, D. C.; Page, C. J.; Boettcher, S. W. Amorphous Mixed-Metal Oxide Thin Films from Aqueous Solution Precursors with Near-Atomic Smoothness. *J. Am. Chem. Soc.* **2016**, *138* (51), 16800–16808.

[18] Cochran, E. A.; Woods, K. N.; Johnson, D. W.; Page, C. J.; Boettcher, S. W. Unique Chemistries of Metal-Nitrate Precursors to Form Metal-Oxide Thin Films from Solution: Materials for Electronic and Energy Applications. J. *Mater. Chem. A* **2019**, *7* (42), 24124–24149.

[19] Brinker C. J.; Scherer G. W.; Sol-Gel Science: The Physics and Chemistry of Sol-Gel Processing, *Academic Press, Inc., Boston*, 1st edn, **1990**.

[20] Seon, J.-B.; Cho, Y. H.; Lee, W. H.; Lee, J.-H.; Kim, Y. S.; Char, K. Densification Process and Mechanism of Solution-Processed Amorphous Indium Zinc Oxide Thin Films for High-Performance Thin Film Transistors. *Appl. Phys. Express* **2019**, *12* (7), 071004.

[21] Jo, J.-W.; Kim, Y.-H.; Park, J.; Heo, J. S.; Hwang, S.; Lee, W.-J.; Yoon, M.-H.; Kim, M.-G.; Park, S. K. Ultralow-Temperature Solution-Processed Aluminum Oxide Dielectrics via Local Structure Control of Nanoclusters. *ACS Appl. Mater. Inter.* **2017**, *9* (40), 35114–35124.

[22] Nadarajah, A.; Wu, M. Z. B.; Archila, K.; Kast, M. G.; Smith, A. M.; Chiang, T. H.; Keszler, D. A.; Wager, J. F.; Boettcher, S. W. Amorphous In–Ga–Zn Oxide Semiconducting Thin Films with High Mobility from Electrochemically Generated Aqueous Nanocluster Inks. *Chem. Mater.* **2015**, *27* (16), 5587–5596.

[23] Smith, S. W.; Wang, W.; Keszler, D. A.; Conley, J. F. Solution Based Prompt Inorganic Condensation and Atomic Layer Deposition of Al_2O_3 Films: A Side-by-Side Comparison. *J. Vac. Sci. Technol. A* **2014**, *32* (4), 041501.

[24] Seichter, W.; Mögel, H.-J.; Brand, P.; Salah, D. Crystal Structure and Formation of the Aluminium Hydroxide Chloride $[Al_{13}(OH)_{24}(H_2O)_{24}]Cl_{15}\cdot 13H_2O$. *Eur. J. Inorg. Chem.* **1998** (6)

[25] Mensinger, Z. L.; Gatlin, J. T.; Meyers, S. T.; Zakharov, L. N.; Keszler, D. A.; Johnson, D. W. Synthesis of Heterometallic Group 13 Nanoclusters and Inks for Oxide Thin-Film Transistors. *Angew. Chem. Int. Edit.* **2008**, *47* (49), 9484–9486.

[26] Gatlin, J. T.; Mensinger, Z. L.; Zakharov, L. N.; MacInnes, D.; Johnson, D. W. Facile Synthesis of the Tridecameric Al_{13} Nanocluster $Al_{13}(\mu_3\text{-}OH)_6(\mu_2\text{-}OH)_{18}(H_2O)_{24}(NO_3)_{15}$. *Inorg. Chem.* **2008**, *47* (4), 1267–1269.

[27] Wang, W.; Wentz, K. M.; Hayes, S. E.; Johnson, D. W.; Keszler, D. A. Synthesis of the Hydroxide Cluster $[Al_{13}(\mu_3\text{-}OH)_6(\mu_2\text{-}OH)_{18}(H_2O)_{24}]^{15+}$ from an Aqueous Solution. *Inorg. Chem.* **2011**, *50* (11), 4683–4685.

[28] Fulton, B. L.; Perkins, C. K.; Mansergh, R. H.; Jenkins, M. A.; Gouliouk, V.; Jackson, M. N.; Ramos, J. C.; Rogovoy, N. M.; Gutierrez-Higgins, M. T.; Boettcher, S. W.; Conley, J. F.; Keszler, D. A.; Hutchison, J. E.; Johnson, D. W. Minerals to Materials: Bulk Synthesis of Aqueous Aluminum Clusters and Their Use as Precursors for Metal Oxide Thin Films. *Chem. Mater.* **2017**, *29* (18), 7760–7765.

Chapter II

[1] P. L. Qin, H. W. Lei, X. L. Zheng, Q. Liu, H. Tao, G. Yang, W. J. Ke, L. B. Xiong, M. C. Qin, and X. Z. Zhao, *Adv. Mater.* Interfaces, 2016, **3**, 1500799.

[2] A. Nadarajah, M. E. Carnes, M. G. Kast, D. W. Johnson, and S. W. Boettcher, *Chem. Mater.*, 2013, **25**, 4080−4087.

[3] J. W. Hennek, M. G. Kim, M. G. Kanatzidis, A. Facchetti, and T. J. Marks., *J. Am. Chem. Soc.*, 2012, **134**, 9593–96.

[4] M. Kast, E. A. Cochran, L. Enman, G.Mitchson, J.Ditto, C. Siefe and P. Plassmeyer, J. *Am. Chem. Soc.*, 2016, **138**, 16800–808.

[5] E.A. Cochran, K.Woods, D.W. Johnson, C.J. Page, and S.W. Boettcher, *J. Mat. Chem.*, 2019, **42**, 24124–49.

[6] C. J. Brinker and G. W. Scherer Academic Press, Inc., Boston, 1st edn, 1990.

[7] A. Nadarajah, M. Z. B. Wu, K. Archila, M. G. Kast, A. M. Smith, T. H. Chiang, D. A. Keszler, J. F. Wager, and S. W. Boettcher, *Chem. Mater.*, 2015, **27**, 5587–96.

[8] J. Jo, Y. Kim, J. Park, J. S. Heo, S. Hwang, W. Lee, M. Yoon, M. Kim, and S. K. Park. *ACS. Appl. Mater. Interfaces,* 2017, **40**, 35114–24.

[9] W. Xu, H. Li, J. Bin Xu and L. Wang, *ACS Appl. Mater. Interfaces*, 2018, **10**, 25878–901.

[10] A. Liu, H. Zhu, H. Sun, Y. Xu and Y. Noh, *Adv. Mater.*, 2018, **30**, 1706364.

[11] D. A. Marsh, W.S. Elliott, R. M. Smith, M. C. Sharps, M. K. Baumeister, M. E. Carnes, L. N. Zakharov, W. H. Casey, and D. W. Johnson, *Angew. Chem. Int. Ed.,* 2017, **56**, 8776–8779.

[12] A.Werner, *Ber. Dtsch. Chem. Ges.*, 1907, **40**, 2103 –2125.

[13] J.P. Picard, G. Baud, J.P. Besse, and R. Chevalier, J. Less. *Common Met.*, 1980, **75**, 99-104.

[14] H. S C. O'Neill, *Eur. J. Min.*, 1994, **6**, 603-609

[15] J. Kacher, C. Landon, B. L. Adams and D. Fullwood, *Ultramicroscopy*, 2009, **109**, 1148–1156.

[16] M. Oku and K. Hirokawa, *J. Electron Spectrosc.*, 1976, **8**, 475–481.

[17] B. S. M. Kretzschmar, K. Assim, A. Preuß, A. Heft, M. Korb, M. Pügner, T. Lampke, B. Grünler and H. Lang, *RSC. Adv.,* 2018, **8**, 15632–15640.

[18] C. S. Yang, J. S. Kim, J. W. Choi, M. H. Kwon, Y. J. Kim, J. G. Choi and G. T. Kim, *J. Ind. Eng. Chem.*, 2000, **6**, 149-156.

[19] K.M. Norelli, P.N. Plassmeyer, K.N. Woods, B.A. Glassy, C. C. Knutson, M. Beekman, and C. J. Page. *Solid State Sci.*, 2016, **55**, 8−12.

[20] A. L. Patterson, *Phys. Rev.,* 1939, **56**, 978–982.

[21] C. Cheng, M. Serizawa and H. Sakata, *Mater. Chem. Phys.*, 1998, **53**, 225-230.

[22] P. S. Patil, L. D. Kadam, and C. D. Lokhande, *Thin Solid Films*, 1996, **272**, 29-32.

[23] R.H. Misho and W.A. Murad, *Sol. Energ. Mat. Sol. C.*, 1992, **27**, 335.

[24] V. R. Shinde, S. B. Mahadik, T. P. Gujar and C. D. Lokhande, *Appl. Surf. Sci.*, 2006, **20**, 7487–92.

[25] L.D. Kadam, and P.S. Patil, *Mater. Chem. Phys.*, 2001, **68**, 225.

[26] L.J. Enman, M. G. Kast, E. A. Cochran, E. Pledger, M. B. Stevens, and S. W. Boettcher, *J. Phys. Chem. C* , 2018, **25**, 13691–704.

[27] D. M. Hausmann and R. G. Gordon, *J. Cryst. Growth*, 2003, **249**, 251–261.

CHAPTER III

[1] Barako, M. T.; Gambin, V.; Tice, J. Integrated Nanomaterials for Extreme Thermal Management: A Perspective for Aerospace Applications. *Nanotechnology* **2018**, *29* (15), 154003.

[2] Luedtke, A. Thermal Management Materials for High-Performance Applications. *Adv. Eng. Mater.* **2004**, *6* (3), 142–144.

[3] Slack, G. A. Anisotropic Thermal Conductivity of Pyrolytic Graphite. *Phys. Rev.* **1962**, *127* (3), 694–701.

[4] Minerals Technologies; Minteq pyrogenics group; https://www.mineralstech.com/business-segments/minteq/pyrogenics

[5] Taylor R.; The thermal conductivity of pyrolytic graphite: *Philos. Mag.* **1966** 13 (21).

[6] Saberi, A.; Golestani-Fard, F.; Willert-Porada, M.; Simon, R.; Gerdes, T.; Sarpoolaky, H. Improving the Quality of Nanocrystalline MgAl2O4 Spinel Coating on Graphite by a Prior Oxidation Treatment on the Graphite Surface. *J. Eur. Ceram.* **2008**, *28* (10), 2011–2017.

[7] Fulton, B. L.; Perkins, C. K.; Mansergh, R. H.; Jenkins, M. A.; Goulioukk, V.; Jackson, M. N.; Ramos, J. C.; Rogovoy, N. M.; Gutierrez-Higgins, M. T.;

Boettcher, S. W.; Conley, J. F.; Keszler, D. A.; Hutchison, J. E.; Johnson, D. W. Minerals to Materials: Bulk Synthesis of Aqueous Aluminum Clusters and Their Use as Precursors for Metal Oxide Thin Films. *Chem. Mater.* **2017**, *29* (18), 7760–7765.

[8] Jo, J.-W.; Kim, Y.-H.; Park, J.; Heo, J. S.; Hwang, S.; Lee, W.-J.; Yoon, M.-H.; Kim, M.-G.; Park, S. K. Ultralow-Temperature Solution-Processed Aluminum Oxide Dielectrics via Local Structure Control of Nanoclusters. *ACS. Appl. Mater. Inter.* **2017**, *9* (40), 35114–35124.

[9] Jing, C.; Zhao, X.; Zhang, Y. Sol–Gel Fabrication of Compact, Crack-Free Alumina Film. *Material. Res. Bull.* **2007**, *42* (4), 600–608.

[10] Wang, W.; Wentz, K. M.; Hayes, S. E.; Johnson, D. W.; Keszler, D. A. Synthesis of the Hydroxide Cluster $[Al_{13}(\mu_3\text{-}OH)_6(\mu\text{-}OH)_{18}(H_2O)_{24}]^{15+}$ from an Aqueous Solution. *Inorg. Chem.* **2011**, *50* (11), 4683–4685.

CHAPTER V

[1] Buck, R.C.; Murphy, P.M.; Pabon, M. Chemistry, properties and uses of commercial fluorinated surfactants**,** T.P. Knepper, F.T. Lange (Eds.), *The Handbook of Environmental Chemistry: Polyfluorinated Chemicals and Transformation Products.* **2012,** Springer, London, 1-19

[2] Barry, V.; Winquist, A.; Steenland, K. Perfluorooctanoic Acid (PFOA) Exposures and Incident Cancers among Adults Living near a Chemical Plant. *Environ Health Perspect* **2013**, *121* (11–12), 1313–1318.

[3] Buck R. C.; Schubert, K. V. Textile fluorochemicals - what users need to know. *AATCC Rev.*, **2009,** 9 (5), 32-36

[4] Farre, M.; Llorca, M.; Perez, S.; Barcelo D.; Perfluorinated compounds in food. T.P. Knepper, F.T. Lange (Eds.), *The Handbook of Environmental Chemistry: Polyfluorinated Chemicals and Transformation Products*. **2012,** 127-14

[5] Shiwanov, E. Chain reactions: a deep look into the DWR dilemma and the current options for product designers. *Inside Outdoor Mag.* **2015,** 24-29

[6] Barry, V.; Winquist, A.; Steenland, K. Perfluorooctanoic Acid (PFOA) Exposures and Incident Cancers among Adults Living near a Chemical Plant. *Environ. Health. Perspect.* **2013**, *121* (11–12), 1313–1318

[7] Hill, P. J.; Taylor, M.; Goswami, P.; Blackburn, R. S. Substitution of PFAS Chemistry in Outdoor Apparel and the Impact on Repellency Performance. *Chemosphere* **2017**, *181*, 500–507.

[8] Stanley, J. K.; Coleman, J. G.; Weiss, C. A.; Steevens, J. A. Sediment Toxicity and Bioaccumulation of Nano and Micron-Sized Aluminum Oxide. *Environ. Toxicol. Chem.* **2010**, *29* (2), 422–429.

[9] Lee, K.; Jur, J. S.; Kim, D. H.; Parsons, G. N. Mechanisms for Hydrophilic/Hydrophobic Wetting Transitions on Cellulose Cotton Fibers Coated Using Al2O3 Atomic Layer Deposition. *J. Vac. Sci. Technol. .A* **2012**, *30* (1), 01A163.

[10] Johnson, R. W.; Hultqvist, A.; Bent, S. F. A Brief Review of Atomic Layer Deposition: From Fundamentals to Applications. *Materials Today* **2014**, *17* (5), 236–246.

[11] Damayanti, N. P. Preparation of Superhydrophobic PET Fabric from Al2O3–SiO2 Hybrid: Geometrical Approach to Create High Contact Angle Surface from Low Contact Angle Materials. *J. Sol-Gel Sci. Techn.* **2010**, *1* (56), 47–52.

[12] Pan, C.; Shen, L.; Shang, S.; Xing, Y. Preparation of Superhydrophobic and UV Blocking Cotton Fabric via Sol–Gel Method and Self-Assembly. *Appl. Surf. Sci.* **2012**, *259*, 110–117.

[13] Fulton, B. L.; Perkins, C. K.; Mansergh, R. H.; Jenkins, M. A.; Goulioukk, V.; Jackson, M. N.; Ramos, J. C.; Rogovoy, N. M.; Gutierrez-Higgins, M. T.; Boettcher, S. W.; Conley, J. F.; Keszler, D. A.; Hutchison, J. E.; Johnson, D. W. Minerals to Materials: Bulk Synthesis of Aqueous Aluminum Clusters and Their Use as Precursors for Metal Oxide Thin Films. *Chem. Mater.* **2017**, *29* (18), 7760–7765.

[14] Smith, S. W.; Wang, W.; Keszler, D. A.; Conley, J. F. Solution Based Prompt Inorganic Condensation and Atomic Layer Deposition of Al_2O_3 Films: A Side-by-Side Comparison. *J. Vac. Sci. Technol. A* **2014**, *32* (4), 041501.

[15] Kim, Y.-H.; Heo, J.-S.; Kim, T.-H.; Park, S.; Yoon, M.-H.; Kim, J.; Oh, M. S.; Yi, G.-R.; Noh, Y.-Y.; Park, S. K. Flexible Metal-Oxide Devices Made by Room-Temperature Photochemical Activation of Sol–Gel Films. *Nature* **2012**, *489* (7414), 128–132.

[16] Jo, J.-W.; Kim, Y.-H.; Park, J.; Heo, J. S.; Hwang, S.; Lee, W.-J.; Yoon, M.-H.; Kim, M.-G.; Park, S. K. Ultralow-Temperature Solution-Processed Aluminum Oxide Dielectrics via Local Structure Control of Nanoclusters. *ACS Appl. Mater. Inter.* **2017**, *9* (40), 35114–35124.

[17] Wang, W.; Wentz, K. M.; Hayes, S. E.; Johnson, D. W.; Keszler, D. A. Synthesis of the Hydroxide Cluster $[Al_{13}(\mu_3\text{-}OH)_6(\mu_2\text{-}OH)_{18}(H_2O)_{24}]^{15+}$ from an Aqueous Solution. *Inorg. Chem.* **2011**, *50* (11), 4683–4685.

[18] Park, S.; Kim, K.-H.; Jo, J.-W.; Sung, S.; Kim, K.-T.; Lee, W.-J.; Kim, J.; Kim, H. J.; Yi, G.-R.; Kim, Y.-H.; Yoon, M.-H.; Park, S. K. In-Depth Studies on Rapid Photochemical Activation of Various Sol–Gel Metal Oxide Films for Flexible Transparent Electronics. *Adv. Funct. Mater.* **2015**, *25* (19), 2807–2815.

[19] Cochran, E. A.; Woods, K. N.; Johnson, D. W.; Page, C. J.; Boettcher, S. W. Unique Chemistries of Metal-Nitrate Precursors to Form Metal-Oxide Thin Films from Solution: Materials for Electronic and Energy Applications. J. *Mater. Chem. A* **2019**, *7* (42), 24124–24149.

[20] Norelli, K. M.; Plassmeyer, P. N.; Woods, K. N.; Glassy, B. A.; Knutson, C. C.; Beekman, M.; Page, C. J. Influence of Composition and Processing Parameters on the Properties of Solution-Processed Aluminum Phosphate Oxide (AlPO) Thin Films. *Solid State Sciences* **2016**, *55*, 8–12.

CHAPTER V

[1] Wilson, B. S.; Finley, C. C.; Lawson, D. T.; Wolford, R. D.; Eddington, D. K.; Rabinowitz, W. M. Better Speech Recognition with Cochlear Implants. *Nature* **1991**, *352* (6332), 236–238.

[2] Vujaklija, I.; Farina, D.; Aszmann, O. C. New Developments in Prosthetic Arm Systems. *Orthop Res Rev* **2016**, *8*, 31–39.

[3] Callaghan, J. C.; Bigelow, W. G. An Electrical Artificial Pacemaker for Standstill of the Heart. *Ann Surg* **1951**, *134* (1), 8–17.

[4] Hartong, D. T.; Berson, E. L.; Dryja, T. P. Retinitis Pigmentosa. *The Lancet* **2006**, *368* (9549), 1795–1809.

[5] Congdon, N.; O'Colmain, B.; Klaver, C. C. W.; Klein, R.; Muñoz, B.; Friedman, D. S.; Kempen, J.; Taylor, H. R.; Mitchell, P.; Eye Diseases Prevalence Research Group. Causes and Prevalence of Visual Impairment among Adults in the United States. *Arch Ophthalmol* **2004**, *122* (4), 477–485.

[6] Zrenner, E.; Stett, A.; Weiss, S.; Aramant, R. B.; Guenther, E.; Kohler, K.; Miliczek, K. D.; Seiler, M. J.; Haemmerle, H. Can Subretinal Microphotodiodes Successfully Replace Degenerated Photoreceptors? *Vision Res* **1999**, *39* (15), 2555–2567.

[7] Zrenner, E.; Bartz-Schmidt, K. U.; Benav, H.; Besch, D.; Bruckmann, A.; Gabel, V.-P.; Gekeler, F.; Greppmaier, U.; Harscher, A.; Kibbel, S.; Koch, J.;Kusnyerik, A.; Peters, T.; Stingl, K.; Sachs, H.; Stett, A.; Szurman, P.; Wilhelm, B.; Wilke, R. Subretinal Electronic Chips Allow Blind Patients to Read Letters and Combine Them to Words. *Proc Biol Sci* **2011**, *278* (1711), 1489–1497.

[8] Stingl, K.; Bartz-Schmidt, K. U.; Besch, D.; Braun, A.; Bruckmann, A.; Gekeler, F.; Greppmaier, U.; Hipp, S.; Hörtdörfer, G.; Kernstock, C.; Koitschev, A.; Kusnyerik, A.; Sachs, H.; Schatz, A.; Stingl, K. T.; Peters, T.; Wilhelm, B.; Zrenner, E. Artificial Vision with Wirelessly Powered Subretinal Electronic Implant Alpha-IMS. *Proc Biol Sci* **2013**, *280* (1757), 20130077.

[9] Stingl, K.; Bartz-Schmidt, K. U.; Besch, D.; Chee, C. K.; Cottriall, C. L.; Gekeler, F.; Groppe, M.; Jackson, T. L.; MacLaren, R. E.; Koitschev, A.; Kusnyerik, A.; Neffendorf, J.; Nemeth, J.; Naeem, M. A. N.; Peters, T.; Ramsden, J. D.; Sachs, H.; Simpson, A.; Singh, M. S.; Wilhelm, B.; Wong, D.; Zrenner, E. Subretinal Visual Implant Alpha IMS – Clinical Trial Interim Report. *Vision Research* **2015**, *111*, 149–160.

[10] Cruz, L. da; Coley, B. F.; Dorn, J.; Merlini, F.; Filley, E.; Christopher, P.; Chen, F. K.; Wuyyuru, V.; Sahel, J.; Stanga, P.; Humayun, M.; Greenberg, R. J.; Dagnelie, G.; Group, for the A. I. S. The Argus II Epiretinal Prosthesis System Allows Letter and Word Reading and Long-Term Function in Patients with Profound Vision Loss. *British Journal of Ophthalmology* **2013**, *97* (5), 632–636.

[11] Watterson, W. J.; Moslehi, S. M.; Smith, J. H.; Montgomery, R. D.; Taylor, R. P. Fractal Electronics as a Generic Interface to Neurons. In *The Fractal Geometry of the Brain*; Di Ieva, A., Ed.; Springer Series in Computational Neuroscience; Springer: New York, NY, 2016; pp 553–565.

[12] Smith, J. H.; Rowland, C.; Harland, B.; Moslehi, S.; Montgomery, R. D.; Schobert, K.; Watterson, W. J.; Dalrymple-Alford, J.; Taylor, R. P. How Neurons Exploit Fractal Geometry to Optimize Their Network Connectivity. *Sci Rep* **2021**, *11* (1), 1–13.

[13] Browning, L. A.; Watterson, W.; Happe, E.; Silva, S.; Abril Valenzuela, R.; Smith, J.; Dierkes, M. P.; Taylor, R. P.; Plank, N. O. V.; Marlow, C. A. Investigation of Fractal Carbon Nanotube Networks for Biophilic Neural Sensing Applications. *Nanomaterials* **2021**, *11* (3), 636.

[14] Watterson, W. J.; Montgomery, R. D.; Taylor, R. P. Fractal Electrodes as a Generic Interface for Stimulating Neurons. *Sci. Rep.* **2017**, 7 (1).

[15] Wang, K.; Fishman, H. A.; Dai, H.; Harris, J. S. Neural Stimulation with a Carbon Nanotube Microelectrode Array. *Nano Lett.* **2006**, 6 (9), 2043–2048.

[16] Smeal, R. M.; Rabbitt, R.; Biran, R.; Tresco, P. A. Substrate Curvature Influences the Direction of Nerve Outgrowth. *Ann. Biomed. Eng.* **2005**, 33 (3), 376–382.

[17] Mizuno, K.; Ishii, J.; Kishida, H.; Hayamizu, Y.; Yasuda, S.; Futaba, D. N.; Yumura, M.; Hata, K. A Black Body Absorber from Vertically Aligned Single-Walled Carbon Nanotubes. Proc. Natl. Acad. Sci. U. S. A. 2009, 106 (15), 6044–6047

[18] Tafti, A. P.; Kirkpatrick, A. B.; Alavi, Z.; Owen, H. A.; Yu, Z. Recent Advances in 3D SEM Surface Reconstruction. *Micron* **2015**, *78*, 54–66.

[19] Carli, L.; Genta, G.; Cantatore, A.; Barbato, G.; De Chiffre, L.; Levi, R. Uncertainty Evaluation for Three-Dimensional Scanning Electron Microscope Reconstructions Based on the Stereo-Pair Technique. *Measurement Science and Technology* **2011**, *22* (3), 035103.